SEARCH FOR AXION-LIKE PARTICLES THROUGH THEIR EFFECTS ON THE TRANSPARENCY OF THE UNIVERSE WITH THE FERMI LARGE AREA TELESCOPE

Dissertation

zur Erlangung des akademischen Grades
doctor rerum naturalium
(Dr. rer. nat.)
im Fach: Physik
Spezialisierung: Experimentalphysik

eingereicht an der
Mathematisch-Naturwissenschaftlichen Fakultät
der Humboldt-Universität zu Berlin

von

M. Sc. Galo Gallardo Romero

Präsidentin der Humboldt-Universität zu Berlin:
Prof. Dr.-Ing. Dr. Sabine Kunst

Dekan der Mathematisch-Naturwissenschaftlichen Fakultät:
Prof. Dr. Elmar Kulke

Gutachter:
1. Prof. Dr. Elisa Bernardini, Deutsches Elektronen-Synchrotron, Zeuthen.
2. Prof. Dr. Dieter Horns, Universität Hamburg, Hamburg.
3. Dr. Gernot Maier, Deutsches Elektronen-Synchrotron, Zeuthen.

Tag der mündlichen Prüfung: 19. Dezember 2019

A mi familia.

"We are trying to prove ourselves wrong as quickly as possible, because only in that way can we find progress." — Richard P. Feynman

Abstract

Axion-like particles, pseudo-scalar particles that arise in theories beyond the Standard Model, mix with photons in the presence of magnetic fields. From Faraday rotation measurements, we know that such fields exist in different astrophysical environments, allowing us to search for axion-like particle effects through photon propagation in those regions.

The flux of γ-ray sources is attenuated due to the pair production process with the extragalactic background light, the radiation accumulated in the Universe from star formation and active galactic nuclei emission. This background radiation makes the Universe opaque to γ rays above a certain energy that depends on the distance to the source. If an axion-like particle is produced within a cosmic magnetic field, it evades extragalactic background light absorption and thus it can survive cosmological distances until oscillating back into a photon. This leads to an increased transparency of the Universe to γ rays.

In the scope of this thesis, we search for transparency effects compatible with the existence of axion-like particles with six years of data from the *Fermi* Large Area Telescope. We derive and combine the likelihoods of the highest-energy photon events from a sample of hard distant sources, in order to compare models that include axion-like particles and models with only extragalactic background light. The sources are active galactic nuclei from the Second Catalog of Hard *Fermi* sources at redshift $z \geq 0.1$.

For values of the intergalactic magnetic field strength $B = 1$ nG and coherence length $s = 1$ Mpc, we find no evidence for a modified transparency induced by axion-like particles and therefore we set upper limits. We exclude photon-axion coupling constants $g_{a\gamma}$ above $1 \cdot 10^{-11}$ GeV^{-1} for axion masses $m_a \lesssim 3.0$ neV.

Zusammenfassung

Axionartige Teilchen sind pseudoscalare Teilchen welche in Theorien jenseits des Standardmodells vorhergesagt werden. Diese oszillieren in Anwesenheit von magnetischen Feldern zu Photonen und umgekehrt. Wie durch Messungen der Faraday-Rotation bekannt ist, existieren solche Felder in verschiedenen astrophysikalischen Umgebungen. In diesen Bereichen kann die Ausbreitung der Photononen erforscht werden, um nach axionartigen Teilchen zu suchen.

Hochenergetische Photonen wechselwirken mit dem extragalaktischen Hintergrundlicht, welches sich aus der rotverschobenen Strahlung der Sternentstehung sowie von aktiven galaktischen Kernen zusammensetzt. Diese Photonen gehen dabei den Prozess der Paarerzeugung ein. Durch die Vernichtung der Photonen wird die Intensität der Gammastrahlung abgeschwächt und führt somit zur Undurchlässigkeit des Universums ab einer bestimmten Energie, welche abhängig vom Abstand zur astrophysikalischen Quelle ist. Falls ein axionartiges Teilchen innerhalb eines kosmischen magnetischen Felds gebildet wird, wird dieses nicht durch das Hintergrundlicht absorbiert. Daher kann es kosmische Distanzen überbrücken bevor es wieder in ein Photon zurück oszilliert. Dieser Effekt erhöht die Reichweite der Gammastrahlung im Universum.

Im Rahmen dieser Dissertation werden Daten des *Fermi* Large Area Telescopes, aufgenommen über eine Zeitraum von sechs Jahren, systematisch analysiert. Hierbei wird nach axionartigen Teilchen mit Hilfe von Transparenzeffekten des Universums gesucht. In diesem Zusammenhang werden verschiedene Modelle des extragalaktischen Hintergrundlichts mit und ohne Berücksichtigung axionartiger Teilchen verglichen. Hierfür werden Likelihood-Funktionen für das höchst energetische Photon verschiedener entfernter Quelle kombiniert. Diese sind aktive galaktische Kerne mit einer Rotverschiebung $z \geq 0.1$ des Second Catalog of Hard *Fermi*-LAT Sources.

Unter den Annahmen einer intergalaktischen magnetischen Feldstärke von $B = 1\,\mathrm{nG}$ und einer Kohärenzlänge von $s = 1\,\mathrm{Mpc}$ wurde keine Veränderungen der Transparenz durch axionähnliche Teilchen nachgewiesen. Für eine Masse eines axionartigen Teilchens mit $m_a \lesssim 3.0\,\mathrm{neV}$ wird eine Photonen-Axion Kopplungskonstante $g_{a,\gamma}$ über $1 \cdot 10^{11}\,\mathrm{GeV}^{-1}$ ausgeschlossen.

List of abbreviations

CMB: cosmic microwave background

HE: high-energy

VHE: very high-energy

LAT: Large Area Telescope

WIMP: weakly interacting massive particle

SM: Standard Model

ALP: axion-like particle

QCD: quantum chromodynamics

QED: quantum electrodynamics

EBL: extragalactic background light

MC: Monte Carlo

AGN: active galactic nucleus/nuclei

SED: spectral energy distribution

GRB: gamma-ray burst

PSF: point spread function

IACT: imaging atmospheric Cherenkov telescope/technique

HEP: highest-energy photon

IGMF: intergalactic magnetic field

IGM: intergalactic medium

GMF: galactic magnetic field

p.d.f.: probability distribution function

CGRH: cosmic gamma-ray horizon

ROI: region of interest

IC: inverse Compton

SSC: synchrotron self Compton

Contents

Chapter 1

INTRODUCTION

Astronomy is the scientific study of space, planets, stars, and other celestial objects. It has been around ever since early civilizations began to stare at the night sky, in an impressive effort to understand the Universe. Nowadays, thanks to technological advances, our instruments allow us to observe photons with energies up to the TeV range.[1] Important progress in astronomy came with the invention of the telescope in the 17th century. In the 19th century, the development of the spectroscope and the photographic plate helped the field to progress even further, granting the possibility of discerning elements in stars. Among the achievements of optical astronomy, the discovery of the expansion of the Universe is of particular relevance for modern cosmology.

The field was limited to optical observations until 1933, the year in which cosmic radio emission was first observed by Jansky [1]. Another remarkable example of radio observations was the discovery of the cosmic microwave background (CMB) radiation by Penzias & Wilson in 1965 [2]. Photons with shorter wavelengths than ultraviolet do not penetrate the Earth's atmosphere, and thus were not discovered until the development of rocket technology for the Second World War. The Small Astronomical Satellite 1 (SAS-1), was the first satellite specifically designed for studying the X-ray sky. It was launched in 1970 and it detected 339 X-ray sources in the first uniform all-sky survey [3].

Photons with wavelengths below 10^{-10} m, or energies above 12 keV, are known as γ rays. These photons are the most energetic form of radiation in the electromagnetic spectrum. The first γ-ray detection with extraterrestrial origin was performed by the

[1] In this Dissertation, energies are often given in units of electron volts (eV).

Explorer XI satellite in 1962 [4]. Studies of the γ-ray sky continued further with other experiments. EGRET, one of the instruments on board of the Compton Gamma-Ray Observatory, obtained the first γ-ray map of the whole sky above 100 MeV [5].

Beyond 100 GeV it is not feasible to use satellites for γ-rays detection because lower fluxes and higher energies require larger collection areas and bigger telescope sizes. Fortunately, γ rays at these energies cause electromagnetic cascades in the upper atmosphere. Charged particles in the cascade travel faster than light in the medium, producing optical Cherenkov radiation that can be used to reconstruct the information of the primary γ ray. Using this technique, the Whipple telescope began the study of the very high energy sky from the ground and discovered the Crab Nebula in 1987 [6]. Similar methods are used in other cosmic ray experiments, measuring the Cherenkov radiation emitted in the pass of atmospheric showers through water tanks. Both types of telescopes, satellites and ground based, are required to cover the full γ-ray band.

The only high-energy (HE) gamma-ray space telescope currently in operation is the Large Area Telescope (LAT), which is the main instrument on the *Fermi* Gamma Ray Space Telescope spacecraft. The LAT works as a pair-conversion telescope and detects γ-ray photons from 20 MeV to the sub-TeV domain [7]. At present, there are three major ground based Cherenkov telescopes operational for the 50 GeV - 50 TeV energy range: the High Energy Stereoscopic System (H.E.S.S.), the Major Atmospheric Gamma Imaging Cherenkov (MAGIC) and the very Energetic Radiation Imaging Telescope Array System (VERITAS). H.E.S.S. is an array of five telescopes situated in Namibia [8]. MAGIC is an array of two telescopes in La Palma [9]. VERITAS is an array of four telescopes located at the Fred Lawrence Whipple Observatory in southern Arizona, USA [10]. The High Altitude Water Cherenkov Experiment (HAWC) is an active observatory located in Mexico, based on water tanks and designed to observe γ rays and cosmic rays from about 100 GeV to 100 TeV [11].

Photons in the γ-ray energy band are generated by non-thermal emission mechanisms in astrophysical sources, such as neutron stars, supernova explosions or regions surrounding black holes. This allows us to obtain more information about the physical mechanisms in such environments. Apart from studying the nature of gamma ray sources, many efforts have been done by γ-ray and cosmic ray experiments in the field of fundamental physics. A remarkable example is the indirect searches for dark matter, with candidates such as weakly-interacting massive particles that are predicted to annihilate or decay into Standard Model (SM) particles. Observational features on the

signal of γ rays are expected in astrophysical regions of high dark matter density [12].

Besides dark matter, other theories also predict particular features in the observed spectra of γ-ray sources. Axion-like particles (ALPs) are the generalization of the quantum chromodynamics (QCD) axion in theories beyond the SM. Similarly to axions, ALPs mix with photons under the presence of electromagnetic fields [13]. From Faraday Rotation measurements we know that cosmic magnetic fields exist over different scales in the Universe [14]. Depending upon the magnetic field morphology, ALPs mixing to photons may happen at energies above keV, ideal for searches with γ-ray telescopes [15].

Once created by extragalactic objects, γ-ray photons propagate over cosmological distances and are affected by the extragalactic background light (EBL) [16]. They are absorbed by pair production processes with this background radiation and, as a consequence, the transparency of the Universe to γ rays decreases. If a photon mixes with an ALP within a cosmic magnetic field, it is not affected by the EBL and thus it can travel cosmological distances unhindered. It may then oscillate back into a photon, leading to a modification of the γ-ray transparency of the Universe.

In this work, we search for effects compatible with the existence of ALPs with 6 years of data from the *Fermi*-LAT. We use the energies of the highest-energy photon (HEP) events from each source in the Second Catalog of Hard *Fermi*-LAT Sources [17] at redshift $z \geq 0.1$. With these observations and Monte Carlo (MC) simulations, we derive the likelihoods of these events in the presence and absence of ALPs and then we combine them. We find no evidence for ALPs and exclude photon-ALP couplings above $1 \cdot 10^{-11}$ GeV^{-1} for ALP masses $m_a \lesssim 3.0$ neV for a value of the intergalactic magnetic field (IGMF) strength of 1 nG . The derived limits are compatible with constraints imposed by other experiments and within the sensitivities of planned experiments. The bounds are valid only for a limited number of magnetic field parameters and for scenarios with $B < 0.1$ nG we are not able to set any upper limits.

This Dissertation is organized as follows. An overview of emission mechanisms and γ-ray sources is presented in Chapter 2. Propagation through the interstellar medium and detection of γ rays is discussed in Chapter 3. The theoretical background for axions and the experimental searches are summarized in Chapter 4. A detailed description of the search for ALPs through a combined likelihood analysis using the *Fermi*-LAT HEP events is presented in Chapter 5. Finally, the conclusions and outlook are given in Chapter 6.

Chapter 2

GAMMA-RAY SOURCES AND EMISSION MECHANISMS

Cosmic rays were discovered in balloon flights by Victor Hess in 1912. Their composition and spectral features have been widely studied by different experiments ever since, with energies reaching values above 10^{20}eV [18]. Regardless of these observations, the origin of cosmic rays and acceleration mechanisms are not fully understood yet and remain as an active research topic in astrophysics [19, 20].

In 1984, Hillas found that in order to accelerate particles to very high energies, the size of the acceleration region must be at least twice the Larmor radius.[1] This is known as Hillas criterion [22] and gives the maximum energy acquired by a particle traveling in a magnetic field,

$$E_{max} \simeq 10^{18} Z\beta \left(\frac{L}{\text{kpc}}\right)\left(\frac{B}{\mu\text{G}}\right) \text{eV}, \tag{2.0.1}$$

where Z is the charge of the particle, L is the size of the region, B is the magnetic field strength and β is the speed of the shock. Figure 2.0.1 shows potential acceleration regions in astrophysical environments.

Once cosmic rays have been accelerated, they can emit radiation at different wavelengths. The mechanisms, within the SM, for producing γ-ray photons inside astrophysical environments are described in Section 2.1. Depending on the type of accelerated particles involved, these mechanisms can be leptonic or hadronic. In Section 2.2,

[1] The Larmor radius is the radius of the orbit traveled by a charged particle under a uniform and perpendicular magnetic field [21].

some acceleration models are discussed. For both sections we follow closely Ref. [23] and references therein. In Section 2.3, we briefly describe the types of γ-ray sources in which these mechanisms can take place.

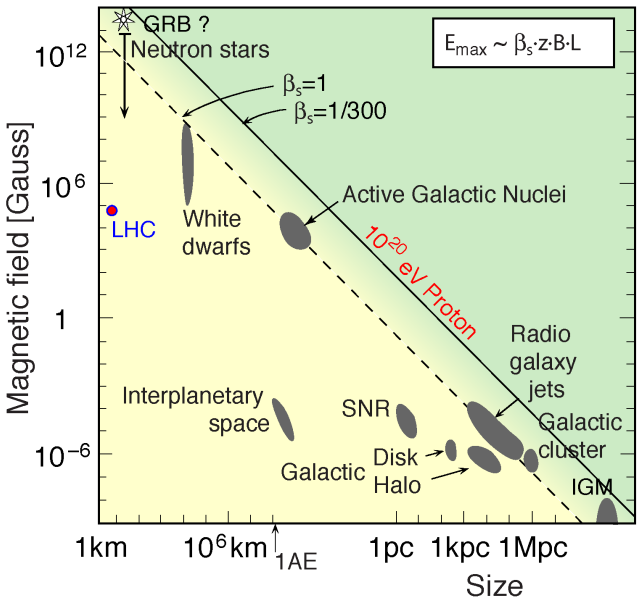

Figure 2.0.1: Hillas plot. Geometrical characterization of potential cosmic ray acceleration sites. The lines represent different proton energies for different shock velocities. The shaded regions represent the size and magnetic field strength of different environments. Adapted from `http://w3.iihe.ac.be/~aguilar/PHYS-467/PA3.html`.

2.1 PRODUCTION OF HIGH-ENERGY PHOTONS

2.1.1 Leptonic processes

Synchrotron radiation

Charged particles emit electromagnetic radiation when they are accelerated. The total power radiated by a non-relativistic electric charge is given by the Larmor formula [24]. From Maxwell's equations, the radiation rates for a charge q moving at relativistic

speeds $\beta = v/c$ are given by [23]:

$$-\left(\frac{dE}{dt}\right) = \frac{q^2\gamma^4}{6\pi\epsilon_0 c^3}\left(|a_\perp|^2 + \gamma^2|a_\parallel|\right), \tag{2.1.1}$$

where $\gamma = (1-\beta^2)^{-1/2}$ is the Lorentz factor, ϵ_0 is the vacuum electric permittivity, and $|a_\perp|$, $|a_\parallel|$ are the normal and parallel components of the acceleration.

Synchrotron radiation is the electromagnetic radiation produced by charged particles under acceleration induced by magnetic fields. This acceleration is described by the Lorentz force, which is always perpendicular to the velocity of the particle and the magnetic field, in the case that the electric field is zero. A schematic representation of this radiative mechanism is displayed in Figure 2.1.1. For a magnetic field strength B and a pitch angle θ between the direction of the particle and the field, the acceleration is:

$$|a_\perp| = \frac{qvB}{\gamma m}\sin\theta. \tag{2.1.2}$$

Due to irregularities in the magnetic field or streaming instabilities, the distribution of scattering angles is expected to be isotropic for high energy particles. From Eq. 2.1.1 and Eq. 2.1.2, the average continuous energy loss rate due to synchrotron radiation is

$$-\left(\frac{dE}{dt}\right) = \frac{16\pi q^4 B^2 p^2}{9\mu_0 c^5 m^4} = \frac{4}{3}\sigma_T c U_{\text{mag}}\beta^2\gamma^2, \tag{2.1.3}$$

where p is the momentum of the particle, σ_T denotes the Thomson cross section, μ_0 is the vacuum permeability constant, and $U_{\text{mag}} = B^2/(2\mu_0)$ is the magnetic field energy. A detailed derivation of the equations presented in this section can be found in Ref. [25]. Synchrotron radiation is dominated by low-mass particles due to a $\propto m^{-4}$ mass dependence in Eq. 2.1.3. For this reason, synchrotron radiation is more important for leptons and it limits the use of electrons or positrons in circular colliders. In any radiative process, the parent particles *cool down* when they lose energy. The cooling time is defined by the ratio of the energy of the charged particles and their energy loss rate and gives the time scale in which the cooling occurs.

Bremsstrahlung

Bremsstrahlung radiation is the electromagnetic radiation due to the deceleration of a charged particle by electric fields. The deflection is often caused by an atomic nucleus.

It is an important radiative process in dense environments, often present in astrophysical sources. Bremsstrahlung radiation is also relevant for particle detectors, as we will see in Chapter 3.2. For relativistic particles, the radiated power is given by [26]:

$$-\left(\frac{dE}{dt}\right) = \frac{Z(Z+1.3)e^6 N}{16\pi^3\epsilon_0^3 m_e^2 c^4 \hbar} E\left[\ln\left(\frac{183}{Z^{1/3}}\right) + \frac{1}{8}\right], \tag{2.1.4}$$

where N and Z are the number density and the atomic number of the target nuclei, respectively. In contrast to the non-relativistic scenario, relativistic Bremsstrahlung energy loss rate is proportional to the energy of the electron, thus the initial particle will lose a significant fraction of its energy in each deflection. An application to ionized plasma can be found in Refs. [27, 25]. Figure 2.1.1 depicts the Bremsstrahlung radiation process between an electron and a proton.

Inverse Compton scattering

The Compton effect is the wavelength increase of a photon after the interaction with an electron [28]. The photon loses part of its energy, which is transferred to the electron. The inverse process can also occur. When a low-energy photon interacts with a HE electron, the charged particle can transfer part of its energy to the photon. This process is called inverse Compton (IC) scattering. Figure 2.1.1 shows the schematic representation of the process. A review of this process can be found in Ref. [25].

There are two energy regimes to distinguish here. Provided that the initial photon energy in the rest frame of the electron is $\hbar\omega \ll m_e c^2$, where m_e is the mass of the electron, the scattering takes place in the Thomson regime. The continuous energy loss rate produced by IC scattering is

$$-\left(\frac{dE}{dt}\right) = \frac{4}{3}\sigma_T c U_{\rm rad}\beta^2\gamma^2, \tag{2.1.5}$$

where $U_{\rm rad} = \epsilon_0 E^2/2$ is the energy density of radiation in the rest frame of the electron. Otherwise, if the initial photon energy is higher than the rest mass of the electron, the process occurs in the Klein-Nishina regime. Eq. 2.1.5 is strikingly similar to Eq. 2.1.3, this can be explained at a quantum level considering the scattering of the electrons with virtual photons coming from the magnetic field in the synchrotron mechanism [29]. If the scattering takes place in the Klein-Nishina regime, the electron loses a significant

amount of energy with each interaction, thus the energy loss is not continuous anymore. The Thomson cross-section can be derived as a low-energy limit of the exact cross-section in the Klein-Nishina regime [30].

The average energy gained by a photon with initial energy E_0 undergoing IC in the Thomson regime is [23]:

$$\langle E \rangle = \frac{4}{3}\gamma^2\beta^2 E_0. \tag{2.1.6}$$

From this equation, we can see that for ultra-relativistic electrons with $\beta \sim 1$, the photon energy can be effectively increased from $E_0 \sim 1$ eV to X-ray or γ-ray energies.

Synchrotron emission and IC scattering can take place with the same population of electrons, this is known as synchrotron self-Compton (SSC) emission. Relativistic electrons that are accelerated in magnetic fields radiate synchrotron photons. The energies of these photons can then be boosted by IC scattering with their parent electrons [31]. For astrophysical environments, the energy spectrum of the synchrotron emitted photons can reach the X-rays band. After IC, these X-ray photons can reach the GeV-TeV energy ranges.

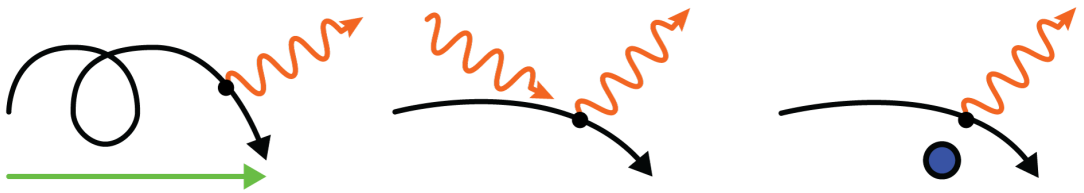

Figure 2.1.1: Main emission mechanisms in astrophysical sources. **Left**: synchrotron radiation (orange line) of an electron (black line) in a magnetic field (green line). **Middle**: IC scattering of an electron and a photon. **Right**: Bremsstrahlung radiation of a moving electron around a nucleus (blue).

2.1.2 Hadronic processes

The above mentioned mechanisms are effective for HE photons production when the primary charged particles are light, such as electrons or positrons, hence they are often called leptonic processes. Nonetheless, depending on the magnetic field strength of the accelerating region, massive particles such as protons can also be responsible of gamma ray emission [32].

Complementary emission models involving hadrons require particle decays. Relativistic beams of accelerated primary protons or nuclei can collide with the interstellar clouds and induce cascades, see e.g. Ref.[33, 34]. If the proton energies are large enough, pion production is possible and they can appear as a result of the following reactions:

$$p + p \rightarrow \pi^+, \pi^-, \pi^0$$

$$p + \gamma \rightarrow \pi_0 + p$$

The first reactions have a low threshold and a high cross section, whereas the last process is only relevant for the UHECRs in the context of γ-ray production. Charged pions decay into muons and neutrinos. On the other hand, neutral pions, with mean life time of 10^{-16} s, decay into pairs of photons [35]. Both decays are displayed in these reactions:

$$\pi^+ \rightarrow \mu^+ + \nu_\mu \qquad \pi^- \rightarrow \mu^- + \bar{\nu}_\mu$$

$$\pi^0 \rightarrow \gamma + \gamma$$

With this mechanism, photons can reach very high energies [36, 37]. A characteristic feature of the decay is a bump around $\sim$ 67 MeV, half of the rest mass of the pion, which has already been detected in supernova remnants with the *Fermi*-LAT [38]. This detection is considered to be an evidence supporting hadronic emission models and cosmic ray acceleration in astrophysical environments.

2.2 ASTROPHYSICAL ACCELERATION OF CHARGED PARTICLES

2.2.1 Second-order Fermi acceleration

In 1949, Fermi proposed a stochastic mechanism in which charged particles are accelerated through collisions with magnetic clouds in the interstellar medium [39]. These magnetic clouds move randomly with speed V and reflect charged particles. The energy of these particles is increased with each reflection in a head-on collision, see Fig. 2.2.1 for a graphical description of the process. If the particles remain in the acceleration zone for some time τ_{esc} before the escape, the energy spectrum turns out to be a power-law.

The energy gain and the spectrum can be derived using relativistic equations, see e.g. the approach of Ref. [40]. A simple formulation of the process is presented next. The average energy of the charged particle, with initial energy E_0, after one collision is $E = \beta E_0$. The probability that it remains in the accelerating region is P. For an initial population of particles N_0 and after k collisions, the number of particles that remain in the accelerating region is $N = N_0 P^k$, while their energies are $E = \beta^k E_0$. We can get a relation between the number of particles and the energies by computing the ratio of logarithms,

$$\frac{\ln(N/N_0)}{\ln(E/E_0)} = \frac{\ln P}{\ln \beta} \quad \rightarrow \quad \frac{N}{N_0} = \left(\frac{E}{E_0}\right)^{\ln P/\ln \beta}. \tag{2.2.1}$$

This equation was derived for k collisions, but some of the particles can still be accelerated after that number, making $N = N(\geq E)$, and thus the energy distribution is a power-law,

$$N(E)dE = \text{constant} \times E^{-1+(\ln P/\ln \beta)}dE. \tag{2.2.2}$$

Comparing this equation with the original work from Fermi, the parameter P is related to τ_{esc}, while β is proportional to $(V/c)^2$. This is why this acceleration mechanism is known as *second-order Fermi acceleration*.

2.2.2 Diffusive shock acceleration

The acceleration mechanism could be more efficient if the fractional energy increase would be $\sim V/c$ instead of $\sim (V/c)^2$. This is called *first-order Fermi acceleration*. By the end of the 1970s, diffusive shock acceleration, a first-order Fermi acceleration process, had gained a lot of attention in astrophysics. It was discovered independently by different people [41, 42, 43, 44]. Strong shock waves propagating through the interstellar medium, discussed in Ref. [45], are common in astrophysical environments. In this section, we follow the physical derivation from Ref. [42]. Ultra-relativistic particles are expected to be in both sides of the shock, which moves much slower compared to the particles. The thickness of the shock is usually much smaller than the gyro-radius of the HE particles, hence the particles barely notice its effects. When a particle crosses the shock in any direction, it is scattered due to streaming instabilities. The velocity distribution of particles becomes isotropic in the reference frame of the moving gas on both sides of the shock.

The dynamics of the problem is shown in Figure 2.2.1. Let us consider a strong shock

wave propagating at speed U through stationary interstellar gas. In the reference frame in which the shock front is at rest, the upstream (front of the shock) gas flows into the shock at velocity $u_1 = U$. After crossing the shock, the downstream (back of the shock) gas has velocity u_2. For a mono-atomic gas in the strong shock limit, the equation of mass continuity yields $u_2 = (1/4)\,U$. When a particle passes through the shock from the upstream side to the downstream side, the gas of the downstream side has a velocity $V = (3/4)\,U$, relative to the upstream side. The energy increase of the particle in the upstream-downstream crossing can be computed with relativistic expressions, and it is given by,

$$\left\langle \frac{\Delta E}{E} \right\rangle = \frac{2}{3}\frac{V}{c} = \frac{1}{2}\frac{U}{c}, \tag{2.2.3}$$

after averaging over all crossing angles of the particles with respect to the shock wave. In the opposite process, when a particle crosses the shock downstream-upstream, the gas moving towards the shock has the same velocity $V = (3/4)\,U$ towards the shock, relative to the downstream gas. The particle gains the same amount of energy in both cases. If the same particle travels back and forth through the shock, the fractional energy increase is doubled. The energy of the particle is always increased when crossing the shock, no matter the side. In contrast to the original Fermi acceleration process, there are never crossings that result in energy loss for the particle that is being accelerated in this scenario.

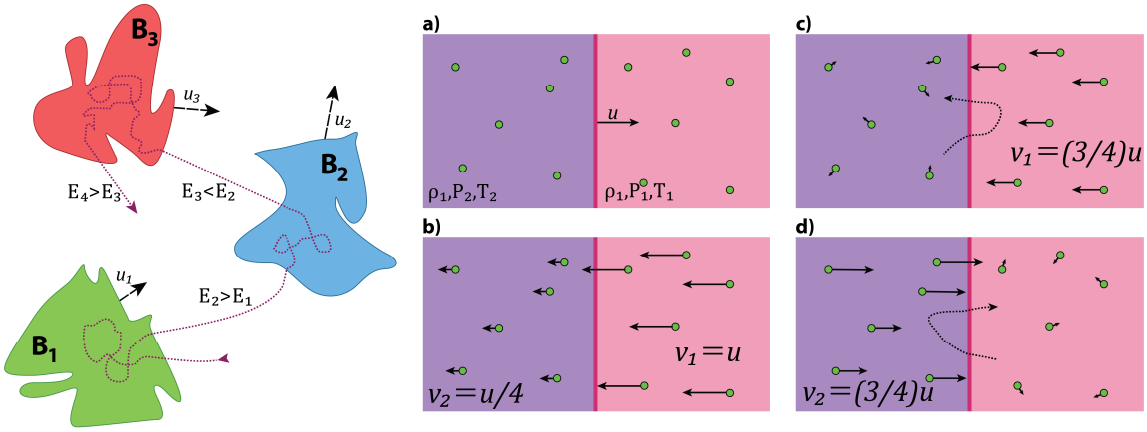

Figure 2.2.1: **Left**: representation of the 2nd-order Fermi acceleration mechanism. A particle is scattered many times in different magnetic mirrors labeled as "B". The particle gains energy in the green and red regions, and it loses energy in the blue cloud. **Right**: representation of charged particles in a shock. **a**): the shock moves at speed u in the observer's frame. **b**): reference frame of the shock. **c**): frame in which the medium is unperturbed in the downstream region and the charged particles velocities are isotropic. **d**): frame in which the medium is unperturbed in the upstream region and the charged particles velocities are isotropic. Adaptated from Ref. [46].

The average number of particles crossing the shock in any direction is $(1/4)\,Nc$, where N is the density of particles. In upstream-downstream crossings, particles can be lost in the flow of gas behind the shock. This is due to the isotropy of the velocity distributions of the particles with respect to the gas in that zone. The flux of particles removed from the system is $(1/4)\,NU$. The probability of losing particles is then the loss flux divided by total flux that crosses the shock, $(1/4)\,NU/\,(1/4)\,Nc = U/c$. The probability of particles remaining in the accelerating region is $P = 1 - U/c$. Comparing these results to the second-order acceleration parameters, the energy increase parameter in a round trip is $\beta = E/E_0 = 1 + U/c$. With these values of P and β, the differential energy spectrum is:

$$N(E)dE = \text{constant} \times E^{-2}dE. \tag{2.2.4}$$

The predicted spectrum in first-order Fermi acceleration is a power-law with index -2. These results are for the simplest diffusive shock acceleration model.

A full treatment of the problem requires the use of the Fokker-Planck equation, taking into account more elements in the problem, such as the effects of magnetic fields in the plasma or the adiabatic and radiative cooling [47]. The effects of the charged particles on the shock itself and the stability of the flows have also to be considered, making the

process of acceleration non-linear. A review of the non-linearity problem is given in Ref. [48], while the efficiency of non-linear models is widely studied with simulations in Ref. [49]. Another problem with this model that the particles need to exceed a threshold energy in order to be further accelerated. For shock acceleration to work, charged particles have to reach an initial energy high enough so that Larmor radius becomes much larger than the size of the shock. This is known as the injection problem [50].

2.2.3 Magnetic reconnection

Magnetic reconnection is a physical process that can take place in highly-conducting plasmas in which the magnetic topology of a system is reorganized. The result of this rearrangement is a conversion of magnetic energy to kinetic and thermal energy. A review on the topic can be found in, e.g. Ref. [51]. The mechanism was first suggested in 1964 [52] in order to explain solar flares particle acceleration.

The first quantitative two-dimensional model, the Parker-Sweet model [53, 54], was developed a decade after the initial model. The schematics of the model are depicted in Figure 2.2.2. Over a region with plasma of density ρ, the magnetic field lines of opposite magnetic fields $\pm B_0$ are steadily brought together in a boundary layer. The size of the region is $2L$ and the thickness of the reconnection layer is 2δ, with $2\delta \ll 2L$. Plasma, to which the magnetic field is frozen according to Alfven's theorem [55], flows into the boundary layer from both sides at a speed v_{in}. This is the same speed at which the lines are steadily merging. A large electric current that heats the plasma is induced in the boundary, leading to locally small Reynolds numbers, thus the field lines velocity deviates from the plasma velocity in the reconnection region. The tension force due to the bend in the reconnected field lines accelerates the plasma flow. Equating the pressure of the heated gas to the magnetic tensions in a steady-state model, the resulting speed of the outflow is the Alfven speed $v_A = B_0/(4\pi\rho)$ [23]. Assuming that the plasma is incompressible, a relation between the initial flow speed of the plasma and the ejection speed can be foun from the conservation of mass:

$$\rho v_{in} L = \rho v_A \delta \quad \rightarrow \quad \frac{v_{in}}{v_A} = \frac{\delta}{L} \tag{2.2.5}$$

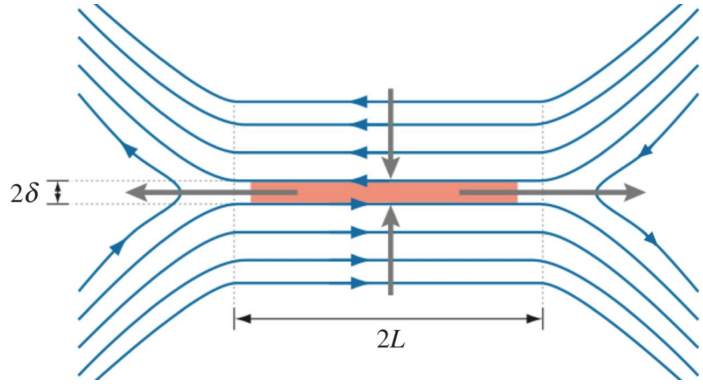

Figure 2.2.2: Geometry of the Sweet-Parker reconnection model. Magnetic field lines (blue) are brought together and merge in the boundary layer (orange). The plasma moves in the direction of the vertical lines and charged particles are accelerated across the horizontal lines. Adapted from Ref. [51]

These values are typically small, thus more complex models of magnetic reconnection are required to explain cosmic ray acceleration. Such models predict instabilities in the flow between the two magnetic fields that generate magnetic islands [56, 57]. In this scenario, particles are first accelerated by the electric fields in the reconnection region and then proceed to further acceleration in the boundaries of the magnetic islands through the Fermi mechanism [58].

2.3 ASTROPHYSICAL SOURCES OF γ-RAYS

The γ-ray sky shows sources from our own galaxy and extragalactic sources. Galactic sources can be divided in diffuse emission, isotropic γ-ray background and point and extended sources. The galactic diffuse emission is the result of the interaction of charged cosmic rays with the interstellar gas and radiation [59]. The isotropic γ-ray background is the remaining background radiation that is not linked to the diffuse background or to a source [60]. In the rest of the section we will summarize the known types of galactic and extragalactic γ-ray sources that do not come from backgrounds.

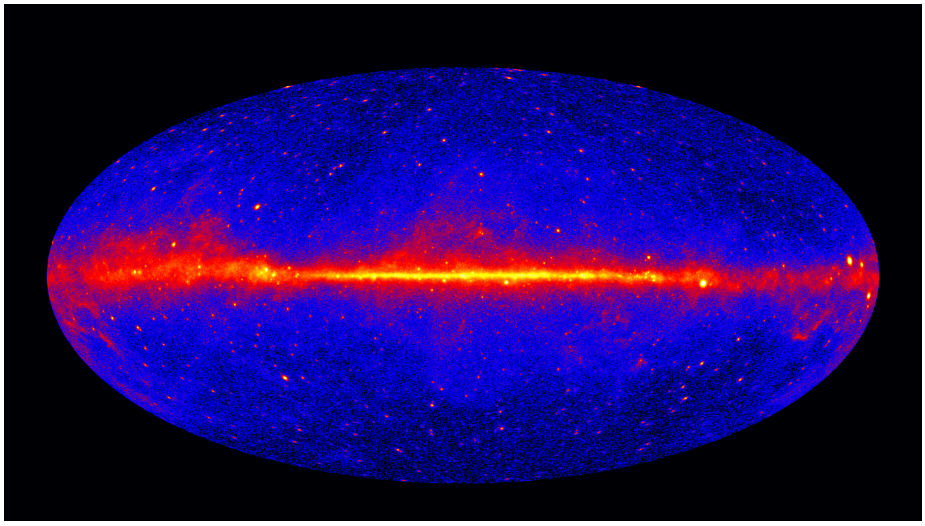

Figure 2.3.1: The γ ray sky above 1 GeV, with 5 years of data from the *Fermi*-LAT. The Milky Way diffuse emission is the bright band along the center of the sky map. Hammer projection. Credit: NASA/DOE/*Fermi*-LAT Collaboration

2.3.1 Sources from the Milky Way

Pulsars and pulsar wind nebulae

Pulsars are largely magnetized neutron stars rotating at very fast speeds that are formed by the collapse of a massive star [61, 62]. Evidence suggests that radiation is emitted in a beam along the magnetic axis of the pulsar, which is generally not the same as the rotational axis, leading to *"pulsed"* observations. Pulsar wind nebulae (PWN) are formed by the interaction of the pulsar wind, electrons produced and accelerated at the pulsar magnetosphere, with the interstellar material [63]. An example of pulsar and PWN is the Crab and its nebula [64].

Supernovae and supernova remnants

Supernovae are violent explosions that occur at the end of massive stars lives. These explosions take place when the core of the star runs out of materials and ceases to generate the required energy to compensate its own gravitational pull, or in thermonuclear explosions in white dwarfs stars binary systems [65]. As a result, most of its material is

expelled at relativistic speeds [66], providing an ideal environment for γ-ray emission, already detected from different supernova remnants [67]. As mentioned in Section 2.1, signatures from the hadronic emission models have also been detected in these sources.

Binary systems

Binary systems are systems of two celestial bodies orbiting each other. The mechanisms of γ-ray emission in these systems can vary depending on the type of binary companions, see e.g. Ref. [68] for a review. The types are:

- Gamma-ray binaries: systems in which the gamma ray emission is dominant. Evidence suggests that these systems are powered by the rotation of a pulsar, but it is still unknown. These sources have already been detected in the HE [69] and very high-energy (VHE) bands [70].
- X-ray binaries (microquasars): systems that are likely to be powered by accretion of stellar mass onto a black hole companion. Most of the emission is detected in the X-ray bands but two have been observed in the HE γ-ray range [71], with no detection at very high-energies.
- Novae: emission from these binaries takes place when a star has a white-dwarf as a companion. It is thought that the radiation comes from thermonuclear explosions on the surface of the white-dwarf star, caused by the accretion of hydrogen from the star. Initially, γ rays between 1 and 10 MeV from decays were expected from these sources. However, novae have already been confirmed as γ-ray sources (see e.g. [72]) even above 100 MeV.
- Colliding wind binaries: systems powered by stellar wind shocks from two massive stars. Gamma-ray binaries are expected to be born when one of the stars runs out of fuel and becomes a neutron star. Only one of these sources has been confirmed as a γ-ray emitter [73].

Galactic Center

The rotational center of our galaxy is known as the Galactic Center. The dynamics are driven by the presence of a super massive black hole [74] located in of the Sgr A* region. Surrounding this region, there is a rich population of astrophysical sources and dense

interstellar gas. The γ-ray emission comes from the interaction between cosmic rays and the interstellar gas and from the many individual sources described above. Because of the absorption produced by the interstellar dust along the line of sight, the Galactic Center can only be observed above the HE X-ray band and at infrared, sub-millimeter and radio wavebands. A review of the γ-ray emission from the Galactic Center can be found in Ref. [75].

The Galactic Center is also relevant for dark matter studies, as a strong density of dark matter particles is expected towards the center of our galaxy, which might be embedded in a dark matter halo. For typical dark matter masses between 10 GeV and 10 TeV, the photon emission is expected to be in the HE and very-high energy bands, which makes current γ -ray telescopes suitable candidates for this study. Recently, an analysis performed by the *Fermi*-LAT found an excess of γ rays in the Galactic Center. However, its implications for dark matter are still unclear due to the magnitude of the systematic uncertainties and only upper limits were reported [76].

2.3.2 Extragalactic sources

Active galactic nuclei

Active galactic nuclei (AGN) are the most common extragalactic γ-ray sources [77]. Super massive black holes accrete matter in the center of these objects and power ultra-relativistic jets of plasma. The HE emission is expected to happen in a compact region of these jets. See Section 2.4 for a more detailed discussion of these sources.

Starburst galaxies

Starburst galaxies are galaxies with a high rate of star formation. Evidence suggests that HE emission comes from the interaction of charged particles with the interstellar medium. Such particles are previously accelerated in the abundant number of supernovae. See e.g. [78] for a review. Two starburst galaxies have been detected at high energies by the *Fermi*-LAT [79]. At very-high energies, these objects have also been detected by HESS [80] and VERITAS [81].

Gamma-ray bursts

Gamma ray bursts (GRBs) are very bright γ-ray events that occur at very short time scales. The exact nature of the bursts is unknown, but evidence points towards the formation of black holes, either by stellar collapse or merging events, see e.g. [82] for a review. The emission from these objects comes in two parts. First, a peak between 0.1 and 1 MeV with a duration between milliseconds and hundreds of seconds is expected. Then, an afterglow at longer wavelengths and timescales takes place [83]. Many GRBs have been detected in the HE range [2] and, by the time of writing this Dissertation, the first GRB in the VHE range was discovered by MAGIC.

2.4 EMISSION FROM ACTIVE GALACTIC NUCLEI

Active galactic nuclei are nuclei of galaxies that display a luminosity much higher than values observed in most galaxies. In contrast to non-active galaxies, the emission of these objects is not compatible with that of the nuclear fusion of stars, see e.g. [84] for a review. The first observations of AGN were the unusual emission lines from the spiral galaxy M77 by Fath [85]. A systematic study of galaxies with such lines was carried out by C. Seyfert and was published in 1943 [86]. With the birth of radio astronomy, some of the objects were found to be nearly point-like or quasi-stellar, and thus were labeled as quasi-stellar radio sources (quasars). In 1963, M. Schmidt measured the redshift of the quasar 3C 273, finding out that this object was extragalactic and implying massive luminosities [87]. The characteristic spectral properties of quasars and luminosities that could not be achieved by thermonuclear reactions within stars led to the idea that these objects were powered by super massive black holes.

According to Ref. [88], only a small percentage, $\sim 5\%$, of galaxies are active. The reasons for the increased activity in only a small fraction of galaxies are often attributed to galaxy merger events or other processes inside the galaxies [89, 90]. This increased activity might also be a stage of galaxies during some time scale around $\sim 10^8$ years. AGN have been observed in a wide range of the electromagnetic spectrum, from radio to γ-ray energy bands. In this section we give a brief overview of the general structure

[2] The *Fermi*-LAT GRB catalog, `https://fermi.gsfc.nasa.gov/ssc/observations/types/grbs/lat_grbs/table.php`

of AGN and the possible emission mechanisms of γ rays. A representation of an AGN can be seen in Fig. 2.4.1.

2.4.1 General structure of active galactic nuclei

Super massive black hole

As seen in Ref. [91], there is evidence that supports the existence of super massive black holes in the center of galaxies. The masses of these black holes, $M_\bullet$, lie between $10^6 - 10^{10}\ M_\odot$. The black hole mass is correlated with the luminosity of the bulge $M_\bullet \sim 10^{-3} M_B$ and with the velocity dispersion of the stars in it $M_\bullet \propto \sigma^4 - \sigma^5$.

Accretion disk

Matter is pulled by the black hole's gravitational force and forms a hot disk around it. Photons emitted by the disk range from the optical wavelength to soft X-rays. Evidence points towards accretion disk emission as the origin of the large blue bump feature of some AGN spectra [92].

X-ray corona

AGN are powerful X-ray sources but the accretion disk cannot produce radiation above $\sim$ keV. The region responsible for the emission of X-rays is the corona surrounding the accretion disk. Hot charged particles can increase the energy of photons to X-ray energies via IC scattering [93].

Broad and narrow line regions

The characteristic emission lines observed in the spectra of AGN are emitted within these regions. The broad line region (BLR) is composed of fast dense bound clouds of interstellar medium close to the black hole, outside the corona. Broad emission lines at UV and optical wavelengths originate here. The narrow line region (NLR), more distant from the black hole, is a region of slower and less dense interstellar clouds. Narrow lines in the spectra are created in this region.

Torus

Unified models of AGN require a dusty torus around the core. The BLR can be obscured in this region. It is heated by the core and re-emits its radiation in the infrared band [94].

Jets

Part of the matter is expelled from the core at relativistic speeds in two opposite directions perpendicular to the accretion disk. These collimated discharges of particles are the jets. Photons across the whole electromagnetic spectrum are produced in the jet, even the highest energies may be produced in the inner jet region. For this reason, AGN are important sources of γ rays. More aspects from the jet are discussed in Section 2.4.3.

2.4.2 Classification of active galactic nuclei

AGN can be divided in two classes depending on their radio emission, namely radio-loud and radio-quiet [95]. For an object to be radio-loud, the ratio of the flux at 5 GHz and the flux in the optical B-band has surpass ~ 10. Different classes of AGN can be explained by the viewing angles θ of the observer with respect to the jet emission. For large values of θ, the obscuring torus hides the emission from the BLR and the accretion disk. Seyfert Type II galaxies and Faranoff-Riley type I and II [96] fall in this category. The former are radio-quiet objects while the latter are radio-loud. At smaller enough angles for the BLR to be visible, there are Seyfert Type I galaxies, quasi-stellar objects (QSOs), steep spectrum radio quasars (SSRQs) and flat spectrum radio quasars (FSRQs). The first two are radio-quiet and the last two are radio-loud. For angles smaller than $\theta \lesssim 10°$, radiation from the jet dominates and AGN are named as blazars. BL Lacs and FSRQs belong to this category. BL Lacs were named after the BL Lacertae galaxy and, in contrast to FSRQs, lack of broad emission lines. If the equivalent width of the lines is smaller than 5 $\AA$, the source is classified as a BL Lac [97]. See Fig. 2.4.1 for a graphical description of the unification scheme.

An alternative classification can be found in Ref. [98]. It consists of measuring the luminosity L_{BLR} of all broad lines in units of the Eddington luminosity and call FSRQs

the sources whose $L_{BLR} \gtrsim 10^{-3} L_{Edd}$. However, this classification scheme needs the redshift and black hole mass of the blazar [99].

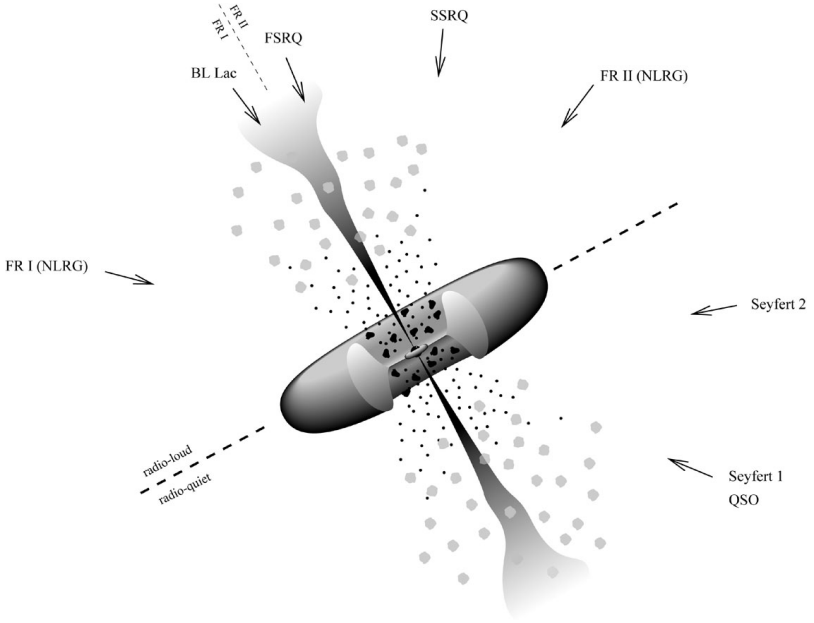

Figure 2.4.1: The unification model for AGNs as described in the text. Different viewing angles yield different types of AGN. Adaptation from [97].

2.4.3 Blazars: high energy emission and spectral energy distributions

Observations suggest [100, 101] that particles in the jet are accelerated through the mechanisms discussed in Section 2.2. Once accelerated, these particles are responsible for the continuum emission from the blazar. Observations of the synchrotron radiation emitted by the jets with radio telescopes have revealed substructures that appeared to surpass the speed of light [102]. This is called superluminal motion, an apparent effect caused by the plasma traveling close to the speed of light at a very small angle with respect to the observer [103]. When superluminal motion of the plasma takes place, its emission is beamed in such a way that the observer sees more intense emission [104]. The observed apparent speed of plasma is

$$\beta_{apparent} = \frac{\beta \sin\theta}{1 - \beta cos\theta}, \tag{2.4.1}$$

where $\beta = v/c$ is the bulk speed and θ the observation angle of the jet. The emission from the jet is boosted by a Doppler factor,

$$\delta = \left[\Gamma\left(1 - \beta\cos\theta\right)\right]^{-1}, \tag{2.4.2}$$

where $\Gamma = \left(1-\beta^2\right)^{-1/2}$ is the bulk Lorentz factor. Strong relativistic beaming in the jets could explain the rapid time variability [105, 106] and apparent luminosities of blazars [107, 108]. This argument does not depend on the physical mechanism that gives rise to the gamma-ray emission, but simply on the observed luminosity and variability time scales at high energies. Additionally, the time-scale of variability is ultimately linked to the time-scale of the variability of the energy source (black hole) which resides in the same rest frame as the observer.

High-energy photons can interact with photons of lower energies through the quantum electrodynamics (QED) pair production process, $\gamma + \gamma \rightarrow e^+ + e^-$, studied in more detail in Section 3.1. In the jet, this interaction can absorb γ rays and prevent them from escaping the source. Following Ref. [109], the pair production survival probability is related to the compactness of the source, which in the Thomson regime is

$$\ell_c = \left(\frac{L'}{R'}\right)\left(\frac{\sigma_T}{m_e c^3}\right). \tag{2.4.3}$$

Where L' is the source luminosity and R' is the size of the emission zone, both in a comoving frame. For simplicity, the emission zone is usually taken as a sphere of radius R'. The size of the sphere can be estimated with the observed time variability t_{var}, giving $R' = ct_{var}\delta_D/\left(1+z\right)$, as shown in Ref. [110]. The emission region is transparent to γ rays if the compactness of the source is $\ell_c \lesssim 40$ [97].

Models for the spectral energy distributions (SEDs), the flux as a function of frequency weighted with the frequency νF_ν, of blazars are reviewed in Ref. [47]. Blazar SEDs display two characteristic bumps at different energies, see Figure 2.4.2. Synchrotron emission of relativistic charged particles is used to explain the low energy part of the SEDs. The energy loss rate of electrons and positrons due to synchrotron radiation in the presence of a magnetic field is given by Eq. 2.1.3. The high energy bump can be explained with leptonic emission models or models that combine hadronic and leptonic emission [111, 112]. In the case of leptonic models, the energy of photons can be boosted by IC scattering with relativistic electrons. Inside the jet, these photons can come from the same parent population of electrons due to synchrotron radiation [113], like in the

SSC model described in Section 2.1. The photon energies can also be boosted with seed photons coming from outside the jet, this is often called external Compton (EC). External seed photons can come from the accretion disk [114], optical/UV emission from the BLR clouds [115, 116] or the infrared radiation from hot dust in the obscuring torus [117]. The energy loss rate of charged particles in the Thomson regime due to IC scattering is characterized by Eq. 2.1.5. In the Klein-Nishina regime, the electron loses a large fraction of its energy in a single collision, thus the energy loss is not continuous anymore. See Fig. 2.4.2 for an example of blazar SED.

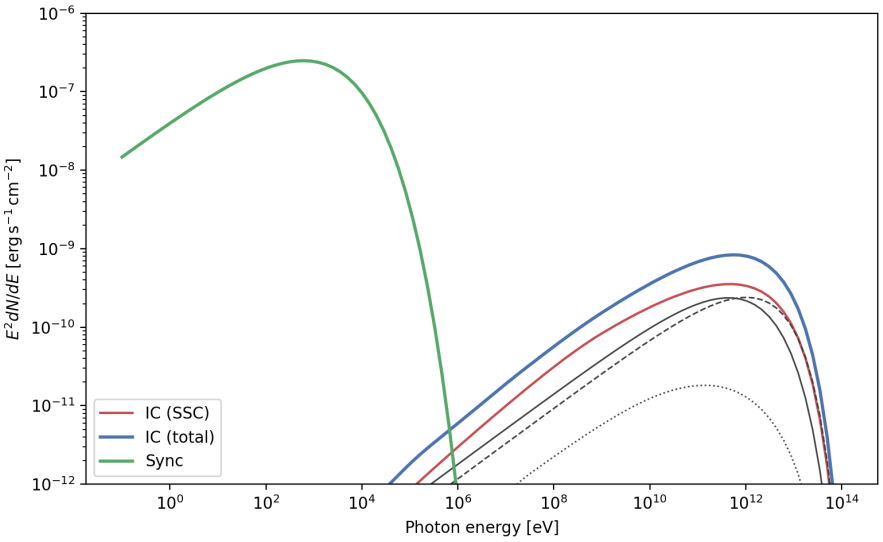

Figure 2.4.2: SEDs for different radiative processes assuming spherical source of radius 2 pc and exponential cut off parent electron distribution. The synchrotron and IC peaks are around 1 keV and 1 TeV, respectively. Naima python code for SEDs calculation, from Ref. [118], `https://naima.readthedocs.io/en/latest/radiative.html`.

In Ref. [119], the SEDs of different blazars were studied with the purpose of searching for a mechanism that connects the differences between BL Lacs and FSRQs. Average SEDs for the total sample of blazars were binned according to radio luminosity, independently of the blazar class. This is known as the blazar sequence. Analytic curves based on the synchrotron and IC continuum emission models were used. The authors find a correlation between the two peaks and the luminosity of the source. As luminosity increases, both peaks of the SED move to lower frequencies and the γ-ray peak becomes more dominant. The γ-ray dominance is computed as the ratio between the luminosity of the γ-ray peak and the synchrotron peak. Blazars with high synchrotron peak have the lowest luminosity and are the least γ-ray dominant.

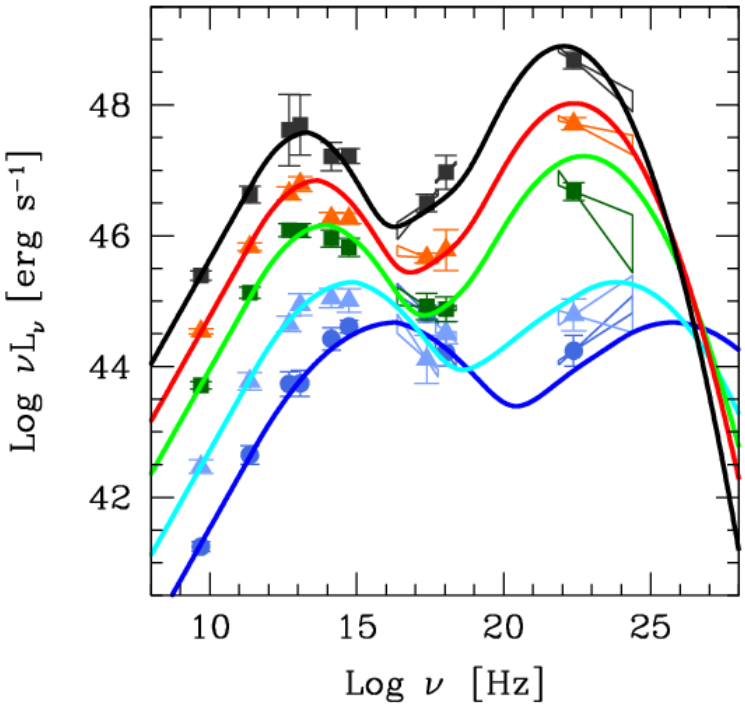

Figure 2.4.3: The blazar sequence, constructed with the 126 blazars observed from radio to gamma bands. Only 33 out of the 126 blazars were detected by CGRO/EGRET. Orginal from Ref. [119], adaptation from Ref. [120].

More recent works on the blazar sequence try to explain the differences between BL Lacs and FSRQs with differences in the accretion rate [121]. A lower accretion rate could result in a reduction of the seed photon population for the IC scattering, allowing the electrons in the jet to reach higher energies. In this scenario, the SEDs peaks are shifted towards higher energies, giving a BL Lac as a result. It has also been proposed that the black hole mass and the accretion rate, the two fundamental parameters governing the accretion process, are sufficient to determine the SEDs of all blazars [122]. This can be tested with the current γ-ray telescopes and the information from Swift in the optical/X–ray energy bands.

Chapter 3

PROPAGATION AND DETECTION OF GAMMA RAYS

The space between stars and galaxies is filled with photon backgrounds at different energies. A relevant example of these backgrounds is the CMB radiation, evidence of the epoch of recombination in which atom formation made the early Universe transparent to radiation [123].

Another important background is the extragalactic background light, the accumulated light in the Universe due to star formation processes and AGN (see e.g. Refs. [124, 125] for in-depth reviews). The flux of extragalactic γ-ray sources is attenuated due to electron-positron pair production processes of γ-ray photons with EBL photons. For this reason, the EBL is crucial in the observation of the γ-ray sky. It is the main source of opacity for the Universe to γ rays. It is also important for re-ionization models in cosmology and galaxy formation and evolution [124].

After propagating through the intergalactic medium (IGM), gamma rays interact with the materials of our detectors. The dominant interaction of HE photons with matter is pair production with the Coulomb fields of atomic nuclei. These photons can induce cascades of secondary particles in the material, which are also common with other cosmic rays [126]. For this reason, the Earth's atmosphere absorbs most radiation above the X-ray waveband, making γ-ray astronomy require space-based detectors. Additionally, HE photons pass through most matter and mirrors cannot be used for detection, therefore gamma-ray astronomy relies on pair production mechanism detectors.

As energy increases, the flux of γ rays decreases and satellite detection is not feasible

anymore due to prohibitive payload sizes. Fortunately, there is a way to reconstruct VHE photons events from the ground. Most of the charged particles in air showers travel faster than the speed of light in the medium, emitting Cherenkov radiation [127]. This light can be gathered by Cherenkov telescopes and analyzed in order to indirectly observe the γ-ray sky. For this chapter we follow the reviews from Refs. [128, 129].

In Section 3.1, we describe the extragalactic background light that affects γ-ray photons in their way to our planet. This includes the theoretical framework required for the calculation of the EBL intensity and a discussion of EBL models. The techniques used in γ-ray astronomy are presented in Section 3.2, as well as a description of the *Fermi*-LAT and Cherenkov telescopes.

3.1 EXTRAGALACTIC BACKGROUND LIGHT

3.1.1 Two-photon annihilation

In Section 2.4.3, we briefly mentioned the consequences of the QED pair production process, $\gamma + \gamma \rightarrow e^+ + e^-$(seen in Fig. 3.1.1), in AGN. It turns out that this interaction is the main physical effect that contributes to the photon propagation in the IGM.

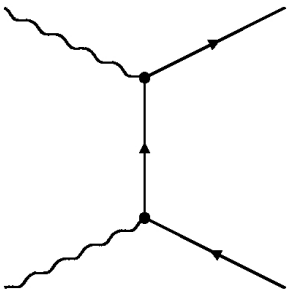

Figure 3.1.1: QED Feynman diagram of the pair production process. Two photons (wiggly lines) annhilate into a electron and a positron (straight lines).

The absorption probabilities for the pair-production process are computed in detail in, e.g. Ref. [130]. The cross-section for the interaction of two photons of energies E and ϵ is,

$$\sigma_{\gamma\gamma}(\beta) = \frac{3\sigma_T}{16}(1-\beta^2)\left[-4\beta + 2\beta^3 + (3-\beta^4)\ln\left(\frac{1+\beta}{1-\beta}\right)\right], \tag{3.1.1}$$

where $\beta = (1-\epsilon_{thr}/\epsilon)^{1/2}$, σ_T is the Thomson cross-section, and ϵ_{thr} is the energy threshold needed for the process to take place.

For two photons colliding at an angle θ between them, the energy threshold is given by:

$$\epsilon_{thr} = \frac{2\left(m_e c^2\right)^2}{E(1 - cos\theta)} = \frac{2\left(m_e c^2\right)^2}{E(1-\mu)}. \tag{3.1.2}$$

Eq. 3.1.1 has its maximum at $\beta = 0.70$. For this value, the relevant wavelength of low-energy photons mainly interacting with the energetic photon of energy E_γ is given by

$$E_\gamma(\mathrm{TeV}) = \frac{0.86\lambda(\mu\mathrm{m})}{(1-\mu)}, \tag{3.1.3}$$

where λ is the EBL photon wavelength, typically between $0.1 - 1000\ \mu$m. From this equation, we can see that the energies that maximize cross-section fall in the γ ray band.

3.1.2 The extragalactic background light intensity

The absorption of radiation in a medium is quantified with the optical depth parameter τ, which is the logarithm of the incoming flux divided by the flux transmitted by the material. In the laboratory frame, the optical depth for γ rays with energy E_0 and redshift z_0 is given by [124]:

$$\tau_{\gamma\gamma}(E_0, z_0) = \int_0^{z_0} dz \frac{\partial L}{\partial z}(z) \int_0^{\infty} d\epsilon \frac{\partial n}{\partial \epsilon}(\epsilon, z) \int_{-1}^{+1} d\mu \frac{1-\mu}{2} \sigma_{\gamma\gamma}\left[\beta(E_0, z, \epsilon, \mu)\right]. \tag{3.1.4}$$

Here we also adopt the notation from Ref. [124]. The first term in the equation is the integration over the line of sight with distance element $\partial L/\partial z$. From Ref. [131], in the standard flat Λ-CDM cosmological model, this term is,

$$\frac{\partial L}{\partial z} = \frac{c}{H_0} \frac{1}{1+z} \frac{1}{\sqrt{\Omega_\Lambda + \Omega_M (1+z)^3}} = \frac{c}{H_0} \frac{\partial \ell}{\partial z}, \tag{3.1.5}$$

where Ω_Λ and Ω_M are the energy densities of the cosmological constant Λ and matter, respectively, and H_0 is the Hubble constant at present day. These values are summarized in Ref. [132]. The term inside the second integral is the density of EBL photons per infinitesimal energy ϵ and redshift z. The last term involves the pair production cross section of Eq. 3.1.1, with a correction on the energies due to redshift, $E_0 = E/(1+z)$. The cross-section term can be worked out analytically with the change of variable

$\mu \to \beta$, giving a simplified expression for the optical depth,

$$\tau_{\gamma\gamma}(E_0, z_0) = \frac{3}{4}\frac{c\sigma_T}{H_0}\int_0^{z_0} dz \frac{\partial \ell}{\partial z}(z) \int_0^{\infty} d\epsilon \frac{\partial n}{\partial \epsilon}(\epsilon, z) \frac{1}{(1+z)^2}\left(\frac{m_e^2 c^4}{E_0 \epsilon}\right)^2 P(\beta_{max}), \quad (3.1.6)$$

with $P(x)$ being an analytical function given in Ref. [124] and $\beta_{max} = \beta(\mu = 0)$.

In order to evaluate the optical depth parameter we need to know the evolution of the EBL number density. In a comoving frame, the specific EBL intensity is related to the number density by [125]

$$\nu I_\nu(\nu, z) = \frac{c\epsilon^2}{4\pi} n(\epsilon, z), \quad (3.1.7)$$

and it is often given in units of $\mathrm{nWm^{-2}sr^{-1}}$. Surveys carried out with the Spitzer and Herschel satellites show that the number density has a strong dependence on the redshift [133, 134].

Direct measurements of the EBL are very difficult due to the presence of other foregrounds. In the solar system, the main source of contamination is the bright zodiacal light from interplanetary dust. Emission coming from stars and the interstellar medium of the galaxy constitutes another source of background. A review of the astronomical challenges involved in direct observations can be found in Ref. [135].

Upper limits on the EBL intensity can be derived from direct measurements, but these are subject to large uncertainties. Lower limits can be obtained with galaxy counts, integrating the light emitted by resolved galaxies. However, this method does not make certain that all of the EBL intensity is measured, since faint emission and diffuse background components may be missed out [136, 137]. Additionally, if the fluxes of individual sources are below a certain value, they cannot be distinguished from random background fluctuations. The stacking of astronomical images at a given wavelength intensifies the signal of sources relative to the fluctuations [133].

Furthermore, there are years of data from γ-ray telescopes that can be used to constrain the EBL intensity. The flux of γ-ray sources is attenuated along the line of sight due to the pair production mechanism with EBL photons. This absorption feature is used for a wide variety of blazars in order to have an indirect measurement of the EBL [124]. The latest results from the H.E.S.S. collaboration can be found in Ref. [138] and are displayed in Fig. 3.1.2, with other measurements, in good agreement with existing upper and lower limits.

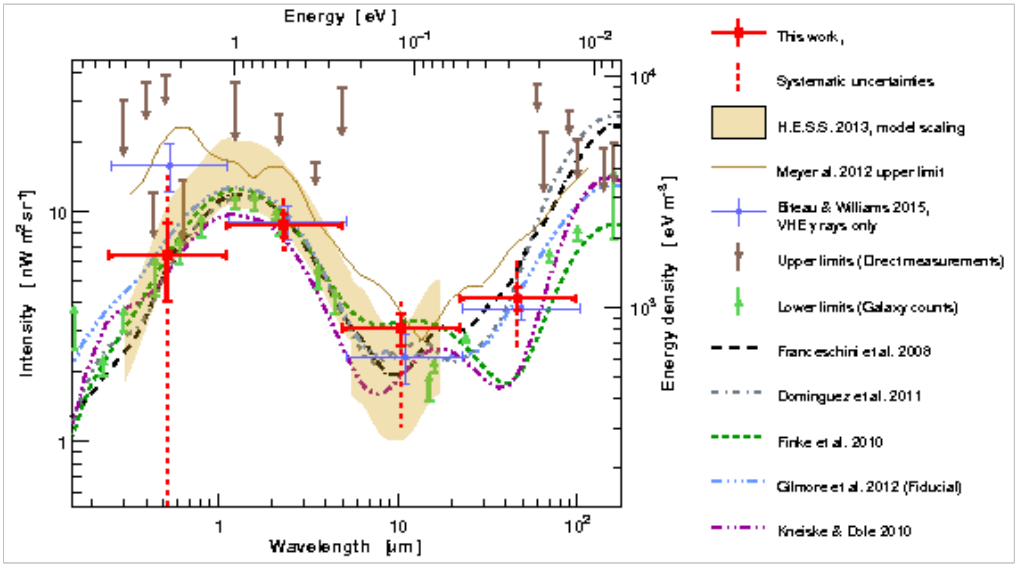

Figure 3.1.2: Results from different experiments of the EBL intensity at $z = 0$ as a function of wavelength. Upper limits are shown in brown and lower limits in green. H.E.S.S results, displayed as red data, are derived from gamma-ray observations. Adapted from Ref. [138].

3.1.3 Models

The many different approaches used to model the intensity of the EBL at $z = 0$ are described in detail in, e.g. Ref. [135]. The goal of these models is to obtain the evolution of the comoving specific luminosity $\mathcal{L}_\nu(\lambda, z)$ with redshift. If the SEDs of galaxies and the comoving number density did not evolve in time then $\mathcal{L}_\nu(\lambda, z)$ would not depend on z.

Backward evolution

Backward evolution models determine $\mathcal{L}_\nu(\lambda, z)$ starting from its value at $z = 0$. These models begin with a set of SEDs of galaxies from the local Universe and extrapolate their spectral properties back in time. The EBL intensity from the local Universe is used as integral constraints. All types of galaxy morphologies and activities must be taken into account. Some examples can be found in, e.g. Refs. [139, 140, 141].

Forward evolution

Forward evolution models begin with the cosmic star formation rate in order to determine the evolution of $\mathcal{L}_\nu(\lambda, z)$ [142]. In addition, these models have to take into account the light that is absorbed by dust and the spectrum of the infrared reemission, which depends on the properties of the dust. Examples of these models can be found in Refs. [143, 144]. A recent derivation of the cosmic star formation rate can be found in Ref. [145].

Cosmic chemical evolution

Cosmic chemical evolution models try to determine the luminosity evolution by treating the Universe as a closed system. Within this system, chemical evolution equations are used to describe the evolution of its contents, namely stars, interstellar gas, metallicity and radiation. See, e.g. Ref [146].

Semi-analytic models

Semi-analytic models calculate $\mathcal{L}_\nu(\lambda, z)$ by merging all the appropriate physical processes within the ΛCDM cosmological model, with its parameters estimated from Wilkinson Microwave Anisotropy Probe (WMAP5) observations [147]. These models are the most complex and require a large amount of input parameters. See, e.g. Refs. [148, 149] for examples and more detailed descriptions.

A comparison of optical depths computed with different EBL models is displayed in Fig. 3.1.3. Different colors correspond to different models, whereas different line styles indicate a change in redshift. The optical depth parameter increases with energy and redshift.

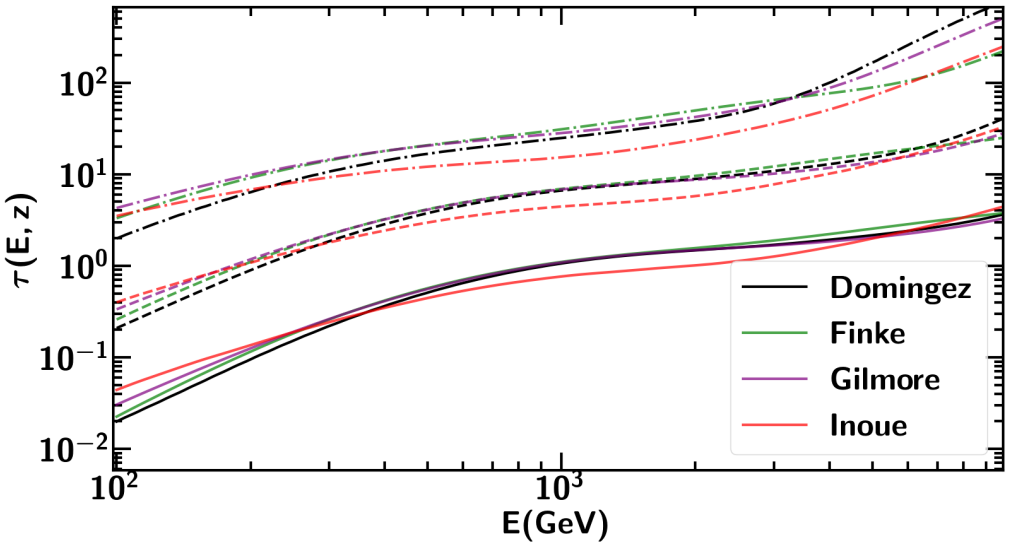

Figure 3.1.3: Optical depth for different EBL models. The solid lines represent z=0.1, the dashed lines are for z=0.5 and the dash-dotted lines are for z=2.0. The original tables were derived in Refs. [150, 143, 149, 148].

3.2 DETECTION TECHNIQUES IN GAMMA-RAY ASTRONOMY

3.2.1 Space-based detectors

The γ-ray band covers different orders of magnitude in the spectrum, therefore a wide variety of detection techniques is required. The type of detector depends upon the type of interaction γ-ray photons undergo in every specific energy range.

The dominant absorption mechanism in the medium-energy range, from 1 to 30 MeV, is Compton scattering, described in Section 2.1. Compton telescopes, such as COMPTEL [151], consist of two detectors, put one after the other, that record the information of the Compton scattering the photon experiences. The energy and direction of the primary are derived from the energy of the recoil the electrons in each scintillator. New proposed missions to observe the sky in this energy range are ComPair [152] and eASTROGAM [153].

In the HE part, from 30 MeV to 100 GeV, pair production is the dominant absorption process. The basic design of γ-ray pair conversion telescopes features three parts, namely a tracker, a calorimeter and an anti-coincidence detector. In the tracker, the conversion of photons into electron-positron pairs takes place. The pairs are used to reconstruct the direction of the primary γ ray. The energy measurement occurs in the calorimeter. A large number of background events in the form of cosmic rays also reach the telescope at any time, hence anti-coincidence shields are needed for background rejection. AGILE [154] and the *Fermi*-LAT [155] are examples of pair conversion telescopes. An schematic representation of pair-production telescopes is displayed in Fig. 3.2.1.

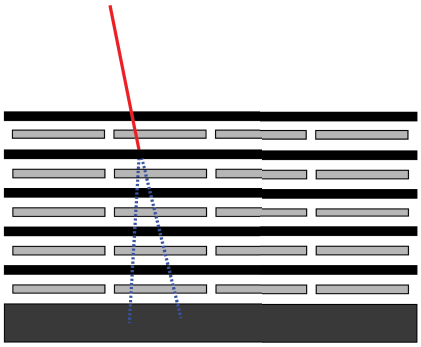

Figure 3.2.1: Schematic representation of pair production telescopes. A photon enters the instrument and turns into an electron-positron pair in the interleaved tracker. The pair finally stops in the calorimeter, in which the energy is measured.

Primary photons initiate electromagnetic cascades while traveling through matter. The initial photon creates an electron-positron pair, which undergoes Bremsstrahlung and further pair production processes. From, e.g. Refs. [156, 157], the photon mean free path in pair production interactions is $7/9X_0$, where X_0 is the radiation length given by:

$$X_0 = \frac{716.5A}{Z(Z+1)\ln\left(287/\sqrt{Z}\right)} \quad \mathrm{g\,cm^{-2}}. \tag{3.2.1}$$

In this approximated equation, A is the atomic mass in $\mathrm{g\,mol^{-1}}$ and Z is the atomic number. For a photon with initial energy E_0, the number of particles in the cascade is increased exponentially after each radiation length, reaching a maximum at $N_{max} \sim E_0/E_c$ and $X_{max} \sim X_0 \ln(E_0/E_c)$, where E_c is the critical energy at which ionization

losses overshadow Bremsstrahlung losses, given by:

$$E_c = \frac{800}{Z + 1.2}\ \text{MeV}. \tag{3.2.2}$$

The arrival direction is derived from the electron-positron pairs in the tracker, which have an average separation angle $\theta \sim m_e c^2/E_0$ in the observer's rest frame. However, multiple Coulomb scattering [158] can occur, limiting the precision of the measurement. For a particle of charge q, moving at speed βc and with momentum p, the root mean square of the scattering angle is

$$\theta_A = \frac{13.6\text{MeV}}{\beta c p} q \sqrt{l/X_0}\left[1 + 0.038 \ln\left(l/X_0\right)\right], \tag{3.2.3}$$

where l is the distance traveled and $n = l/X_0$ is number of radiation lengths. As we can see from Eq. 3.2.3, the number of radiation lengths has to be small in order to reduce the effect of multiple scattering. Therefore, particle trackers are designed in such a way that a minimum amount of material is used. This is why the energy is measured in a separate calorimeter. The probability distribution function (p.d.f.) of the reconstructed direction is described by the point spread function (PSF). Ultimately, the PSF depends on the photon energy, the arrival angle respect to the detector and the detector structure. A photon from a point source will be reconstructed with a 68% probability inside a radius r_{68}, computed by integrating the PSF. The energy resolution is computed in a similar manner with the energy dispersion, the probability distribution of the reconstructed energy.

3.2.2 The *Fermi* Large Area Telescope

The *Fermi* Gamma-Ray Space Telescope (FGST), initially known as Gamma-ray Large Area Space Telescope (GLAST), is a satellite designed for γ-ray astronomy. A detailed description of the mission is given in Ref. [155]. It was launched on 11 June 2008 into a near Earth orbit at an altitude of $\sim$ 565 km with a period of $\sim$ 1.5 hours, as a joint effort between NASA, the United States Department of Energy, and government agencies in France, Germany, Italy, Japan, and Sweden. The main instrument on board is the Large Area Telescope, intended to survey the γ-ray sky for the study of astrophysical and cosmological phenomena. The dimensions of the LAT are 0.72 m $\times$ 1.8 m^2, with a total mass of 2789 kg. An additional instrument is the Gamma-ray Burst Monitor

Quantity	LAT(Min.)	AGILE (GRID)	EGRET
Energy range	20 MeV - 300 GeV	30 MeV - 50 GeV	20 MeV - 30 GeV
Effective area	>8000 cm^2	$\sim$ 500 cm^2 (100 MeV)	1500 cm^2
Field of view	>2 sr	$\sim$ 3 sr	0.5 sr
Angular res.	<0.15°(>10 GeV)	0.7°(1 GeV)	5.8° (100 MeV)
Energy res.	<10%	10% (?)	10%
Deadtime (event)	<10 μs	100 μs	100 ms

Table 3.1: Specifications and performance of the LAT (Pass 7) compared to EGRET and AGILE. Sources: `https://fermi.gsfc.nasa.gov/science/instruments/table1-1.html`, Ref. [160]

(GBM), which is in charge of detecting GRBs and alerting other observatories [159].

3.2.2.1 Telescope specifications and parts

The LAT is a pair conversion telescope sensitive to γ rays with energies between $\sim$ 20 MeV and more than 300 GeV. The field of view (FoV) is 2.4 sr at 1 GeV. A summary of the relevant parameters of the LAT are shown in Table 3.1. A schematic view of the instrument is shown in Figure 3.2.2.

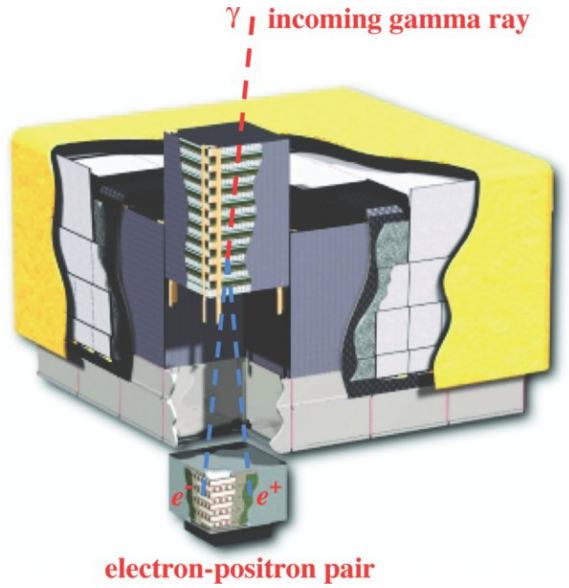

Figure 3.2.2: Schematic representation of the LAT and one of its towers. An incoming gamma ray hits the tracker and turns into an electron-positron pair that, ultimately, reaches the calorimeter. Adapted from Ref. [155].

The LAT is in sky-survey mode $\sim$ 80% of the time. In this mode, the observation axis points at the sky alternating between the northern and the southern hemispheres in each orbit, covering the whole sky every 3 hours. The rest of the time is spent in Galactic center observations, targets of opportunity or autonomous report requests. Roughly a $\sim$ 15% loss of observing time happens when the instrument is transiting the South Atlantic Anomaly (SAA). In this region, the instrument is protected from the high flux of charged particles trapped by the Earth's magnetic field.

Tracker

As seen in Fig. 3.2.2, an incoming gamma ray passes through the anticoincidence detector and continues until it converts into an electron-positron pair in the tracker, described in depth in Ref. [155]. The LAT is divided in 16 modular towers with size $40 \times 40 \times 66$ cm, featuring individual trackers and calorimeters. Each tracker consist of interleaved layers of tungsten foils and silicon-strip detectors (SSDs). The pair conversion takes place in one of the tungsten foils (with atomic number Z=74), while the tracks of the charged particles are measured by the 18 SSDs. Since SSDs are single-sided, strips are alternated in two directions in order to measure the x and

y coordinates. The separation between the lower SSDs and the neighbouring tungsten foil is 30 mm.

In order to improve the relation between the resolution at low energies due to multiple scattering and the required material to provide a good effective area at high energies, the tracker is divided into front and back. The thickness of the first 12 foils (front) is of 0.027 radiation lengths, whereas the last 4 layers (back) are around 0.18 radiation lengths. The PSF also depends on where the conversion takes place. Roughly $\sim 63\%$ of the events are converted in the tracker when they hit the instrument perpendicularly. For more details about the design and performance of the tracker see Ref. [161].

Calorimeter

After passing through the tracker, the particles enter the calorimeter and start losing their energy in electromagnetic cascades. The calorimeter in each tower consists of 96 CsI(Tl) scintillator crystals organized in layers, each containing 8 crystals with a thickness of 8.6 radiation lengths. The layers are arranged in a hodoscopic structure, meaning they are rotated 90 degrees with respect to the previous one. Photodiodes at the end of both crystal edges measure the light from the scintillation and the intensity difference is used to estimate where in the crystal the energy deposition took place. The structure of the calorimeter makes it possible to image a three-dimensional profile of the shower and reconstruct the direction of the primary particle. The imaging feature allows to measure the longitudinal shower development and gives the opportunity to estimate showers that are not fully contained in the instrument, increasing the energy range of the LAT above 300 GeV [162]. The transversal shower development is characterized by the Molière radius [35], which is $R_M = 3.8$ cm for the LAT [155].

Anti-coincidence detector

The majority of events detected with the LAT are background events, since the flux of cosmic rays is much higher than the flux of photons from γ-ray sources. These cosmic rays are mostly charged particles and γ-rays produced from the interaction of other cosmic rays with the Earth's atmosphere [163]. An anti-coincidence detector (ACD) covers the LAT in order to minimize the charged particles background. The ACD consists of 89 overlapping individual tiles of plastic scintillator and bundles of scintillation fibers in-between the tiles. Each tile is connected to two photomultiplier

tubes (PMTs). This design offers a background rejection with a high efficiency and reduces the chance of a false veto due to charged particles created inside the instrument that hit the ACD, known as backsplash effect [164]. Finally, the outer layer of the instrument is wrapped in material that protects against micrometerites and space junk, and provides thermal insulation.

3.2.2.2 Data acquisition system and event reconstruction

As mentioned in the previous section, the events of scientific interest are a very small fraction of all the events that hit the detector. The whole procedure of event reconstruction is explained in depth in Refs. [165, 155]. Before events are publicly available for science, they undergo two steps: on board hardware trigger and on-ground event reconstruction.

The on-board hardware trigger of the LAT is designed to keep γ-ray like events with maximum efficiency and to lower the dead-time down to $\sim$10%. Each one of the different detectors in the telescope can initiate trigger requests for events, which are then combined to begin reading the event information of all subsystems. One example of trigger request is the tracker trigger, which requires a signal from three x–y paired consecutive layers within a single tower, above a certain threshold. All trigger requests are collected in the Central Trigger Unit. If a combination of trigger requests is positive the event acquisition starts. After this step, the event is passed through different on-board filtering algorithms in order to improve background rejection. The LAT on-board analysis reduces raw trigger rate from $\sim$10 kHz down to $\sim$400 Hz. All the relevant information of these events is stored in packets, which are then transferred to a Solid Sate Recorder and finally sent to Earth for further analysis.

On the ground, event reconstruction translates the previously stored event information from each subsystem into physical parameters of the primary γ ray. For this purpose, several algorithms are used. The latest version of the event reconstruction is called Pass 8 [166]. The energy of each event is evaluated with the information from the shower deposited in the crystals of the calorimeter. The amount of energy deposited in the tracker is also taken into account, it is especially relevant for the reconstruction of low-energy events. The direction of the γ ray is estimated with the information from the tracker hits, comparing the results of two different tracking algorithms to get the best candidate track. The data from the tracker and calorimeter are then combined with the ACD information in order to evaluate how likely the event is a γ ray or a

background particle. After this stage, each event is saved with an array of the relevant physical quantities for scientific analysis. In this stage, the $\sim$ 400 Hz trigger rates are reduced to $\sim$ 1 Hz - 10 Hz.

The γ-ray purity of each reconstructed event is classified according to some quality parameters derived in the reconstruction stage. Event classification is useful for deciding what data to include in different astrophysical source analyses. In the Pass 8 release, from lower to higher purity, the classes are: TRANSIENT, SOURCE, CLEAN, ULTRACLEAN. The first class is used for transient sources, which do not require a high purity since the short time scales limit the amount of background counts. The standard point source analysis is performed with SOURCE events. SOURCE and ULTRACLEAN events provide lower background at the cost of lower effective areas. Events within a class can also be subdivided into other types, according to: position in the tracker where the conversion took place (FRONT/BACK), quality of energy reconstruction (EDISP) and quality of the direction reconstruction (PSF).

3.2.2.3 Data analysis and performance

In order to obtain physical results, a quantitative data analysis is needed. Such analyses begin with a list of reconstructed events that come from the region of interest (ROI) we want to study. The LAT team has developed and maintains science analysis tools (ScienceTools) for analyzing LAT data [167] with the maximum likelihood method.[1] The likelihood function L is the probability of observing the data given an input model. The ScienceTools use as input model the spectral information of all the γ-ray sources in the ROI. For a binned analysis, the functional form of the likelihood is the product of the probabilities of observing the detected counts in each bin. The observed number of counts per energy bin is described by a Poisson distribution, hence the probability of detecting n_i counts in the i-th bin is

$$p_i = m_i^{n_i} \frac{e^{-m_i}}{n_i!}, \tag{3.2.4}$$

[1] A full description of the likelihood analysis in the *Fermi* ScienceTools as well as tutorials can be found in: `https://fermi.gsfc.nasa.gov/ssc/data/analysis/`

where m_i is the expected number of counts given by the input model. Since the values per bin are independant, the likelihood is

$$L = \prod_i p_i = e^{-N_{exp}} \prod_i \frac{m_i^{n_i}}{n_i!}. \tag{3.2.5}$$

The first factor in Eq. 3.2.5 depends only on the input model, with $N_{exp} = \sum_i m_i$. One can use L to get the an unbiased estimate of the parameters, which defines the best fit of the model to the data. Ultimately, the likelihood ratio test this allows us to compare between models, for instance in source detection.

A key part of the ScienceTools are the instrument response functions (IRFs) that carry the information of the instrument's performance. The LAT performance depends mostly on the hardware design, the event reconstruction algorithms and the background selections. Event classes depend on the background rejection, hence they have to be considered in the IRFs too. The IRFs are derived with MC simulations of photon interactions with the detectors and can be divided in three factors [155, 165]:

- The effective area, $A_{eff}(E, \hat{v}, s)$, describes the detection efficiency of a γ ray with energy E, a given selection cut s and direction $\hat{v}$. Examples of effective areas can be seen in Fig. 3.2.3.

- The point-spread function, $P(\hat{v'}, E, \hat{v}, s)$, is the p.d.f. of the reconstructed direction of an event, $\hat{v'}$. A photon from a point source will be reconstructed with a certain probability p inside a circle of radius r_p. See Fig. 3.2.3 for examples.

- The energy dispersion, $D(E', E, \hat{v}, s)$, is the p.d.f. of the reconstructed energy of an event, E'. The energy uncertainty ΔE is computed as an integral over the energy dispersion, usually 68%. See also Fig. 3.2.3 for examples.

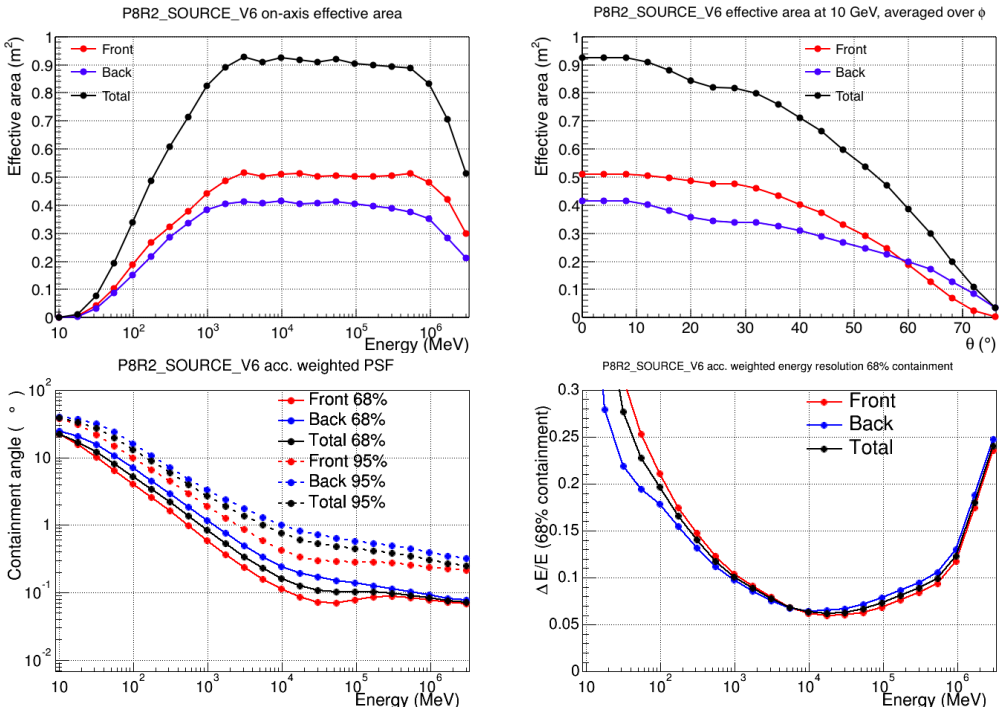

Figure 3.2.3: Summary of the LAT IRFs derived from Monte-Carlo simulations. For the SOURCE event class, latest Pass 8 version, and FRONT/BACK/TOTAL conversion. The acceptance is defined as the effective area integrated over solid angle. **Top left**: the effective area as a function of the energy for normal incidence photons. **Top right**: the effective area as a function of the incidence angle. **Bottom left**: containment angles of the acceptance weighted PSF as a function of the energy. **Bottom right**: Acceptance weighted energy resolution as a function of energy. From `https://www-glast.stanford.edu/instrument.html`.

The IRFs enter the likelihood in the computation of the expected number of counts per energy bin for a given model. The expected number of counts between energies E_1 and E_2 for a source is

$$N_{E_1 E_2} = \int S(E)\epsilon(E)dE, \tag{3.2.6}$$

where $S(E)$ is the spectral model of the source and ϵ is the exposure map. The exposure map is an integral of the total response functions over the entire ROI. Since the response function is a function of the photon energy, the exposure map is also a function of this energy.

3.2.3 Observations from the ground

In spite of the atmosphere being opaque to γ-rays, we can still use the showers they produce in order to reconstruct the events. Depending on the type of primary particles, namely photons and electrons, and hadrons, atmospheric showers are classified as electromagnetic or hadronic, respectively. Electromagnetic air showers started by a γ-ray photon produce first an electron-positron pair due to the electromagnetic fields of atomic nuclei. The pair then radiates more photons through Bremsstrahlung caused by the same fields. This cycle repeats itself, developing a cascade, until the energy of the product particles becomes small enough for the cascade to finally die out.

The distribution of particles as a function of atmospheric depth is known as longitudinal shower development and it depends on the energy of the primary particle. The higher the energy, the longer the cascade develops and the higher the maximum number of particles [168]. The transverse development or lateral spread in the shower is mostly due to the scattering of electrons away from the primary particle direction axis and it is related to the Molière radius, as seen in Section 3.2.1. The CORSIKA code is often used for Monte Carlo simulations of air showers initiated by HE cosmic rays [169].

Whereas electromagnetic showers involve mainly two well-known processes, hadronic showers display a larger complexity. The latter produce many different particles, such as mesons and light baryons. Part of the initial energy goes to electromagnetic subshowers that come from the decay of neutral pions [126]. Nucleons keep developing the hadronic component. Pions and kaons produce mesons until they decay into muons. In contrast to electromagnetic showers, the lateral development of hadronic showers is larger due to the increased transverse momentum from scatterings and decays. The complexity of the shower interactions also leads to more fluctuations. Additionally, the mean free path of hadrons due to nuclear interactions is larger, resulting in a deeper reach of the shower in the atmosphere. An example of both types of showers can be seen in the figure below.

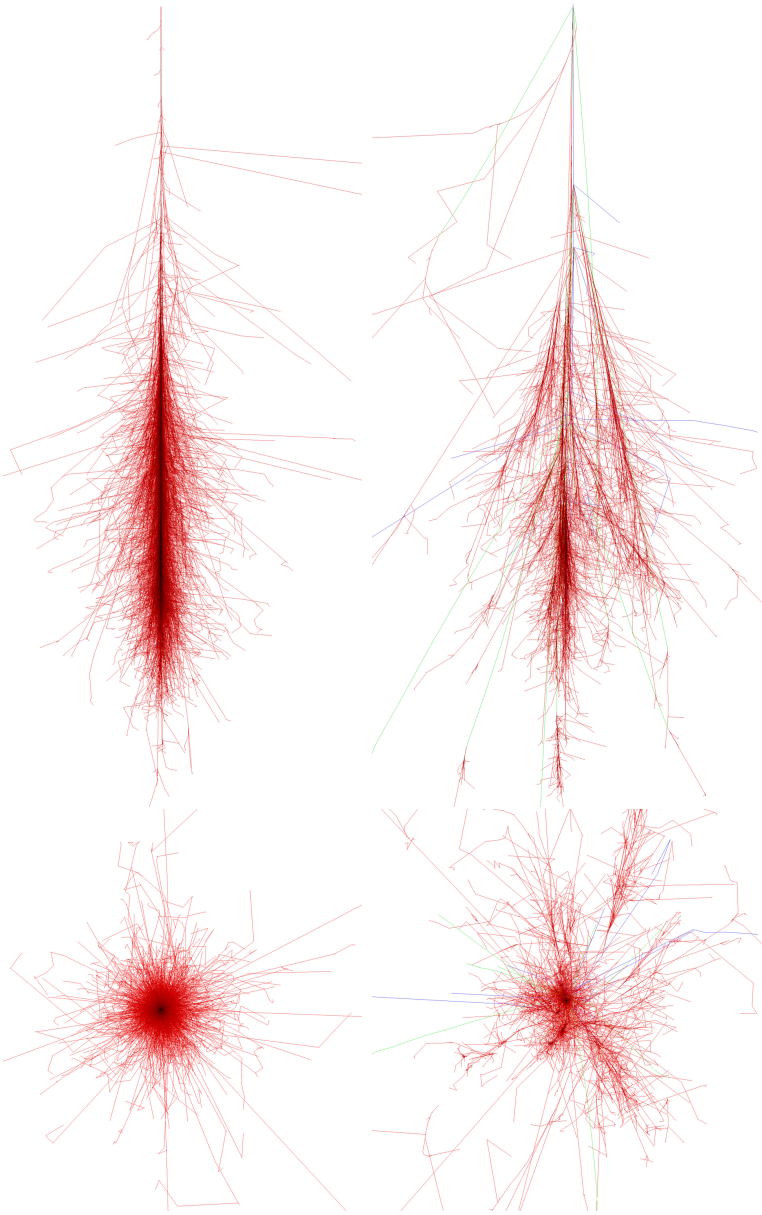

Figure 3.2.4: **Left**: CORSIKA shower images for primary photons of 100 GeV. **Right**: shower images for protons of 100 GeV. F. Schmidt, J. Knapp, "CORSIKA Shower Images", 2005, `https://www-zeuthen.desy.de/~jknapp/fs/showerimages.html`.

When a charged particle travels faster than the speed of light in the medium, Cherenkov radiation is emitted in a small cone centered on the axis of the trajectory of the particle

[127]. The emission angle with respect to this axis is given by

$$\cos\theta = \frac{1}{\beta n}, \tag{3.2.7}$$

where βc is the speed of the particle, $n = c/c'$ is the refractive index and c' is the speed of light in the atmosphere. From this equation, the speed factor threshold required for Cherenkov emission is $\beta_{thr} = 1/n$, thus the energy threshold is:

$$E_{thr} = \frac{mc^2}{\sqrt{1-\beta^2}} = \frac{mc^2}{\sqrt{1-n^{-2}}}. \tag{3.2.8}$$

This equation is proportional to the mass of the charged particle, hence Cherenkov emission is dominant in electromagnetic components of shower. The refractive index depends on the altitude h due to changes in the air density within the atmosphere. If the atmosphere is assumed to be isothermal, the barometric formula [35] gives the dependence of the index with height:

$$n(h) = 1 + \eta_0 \cdot \exp\left(-\frac{h}{h_0}\right). \tag{3.2.9}$$

Here, $\eta_0 = 2.9 \cdot 10^{-4}$ and $h_0 = 7.1$ km. From Eqs. 3.2.7 and 3.2.9, we see that the Cherenkov angle increases with the shower development, until a value of $\theta \simeq 1.4°$ at sea level. Therefore, the image on the ground is an overlapping of Cherenkov light emitted in cones along the charged particles trajectories.

The energy of the primary γ ray can be inferred from the number of Cherenkov photons measured on the ground. These photons are mostly emitted around the shower maximum, which is proportional to the energy of the initial particle. This is used by Cherenkov telescopes in order to reconstruct the energy of the initial γ ray that caused the shower. Arrays of telescopes are often used to view the shower from different angles. This is called the stereoscopic approach and it used to geometrically derive the arrival direction of the γ ray [170]. A graphic representation of this technique is shown in Fig. 3.2.5 .

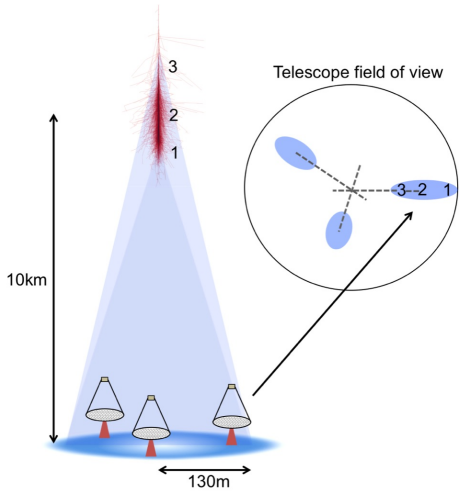

Figure 3.2.5: Illustration of an IACT and the stereoscopic reconstruction. An atmospheric shower develops in the atmosphere due to a primary cosmic ray. The resulting Cherenkov radiation pool is observed by an array of telescopes on the ground. The field of view of the array and the directional reconstruction are shown within the circle. Adapted from Ref. [171], which also gives a detailed summary of the Cherenkov telescopes imaging technique.

Currently, there are three major ground based Imaging Atmospheric Cherenkov Telescope (IACTs) arrays operational for the 50 GeV - 50 TeV energy range: HESS, MAGIC and VERITAS.

Chapter 4

AXION-LIKE PARTICLES

Noether's theorem [172], published in 1918, is one of the most important results in physics. It established a relationship between symmetries and conservation laws, which had a crucial role in the development of modern physics. The Standard Model is built upon invariance under gauge symmetries [173]. Besides continuous symmetries, the Lagrangians of fundamental theories can also be invariant under discrete symmetries. Three relevant discrete symmetries in the SM are:

- Parity (P), the spatial inversion through the origin.
- Charge conjugation (C), the operator that changes the sign of all charges of a particle.
- Time reversal (T), the transformation of time.

It was generally accepted that parity was conserved until 1957, year in which Wu's experiment discovered parity violation in the weak interactions, already proposed by Yang and Lee [174]. In 1964, CP violation in weak interactions was discovered too [175]. Nowadays, we know that any Lorentz invariant local quantum field theory with a hermitian Hamiltonian must be invariant under simultaneous transformations of charge, parity and time. This is known as the CPT theorem (see e.g. Ref. [176] for a review).

Symmetry groups have also important consequences in QCD. The presence of symmetries in the Hamiltonian of the theory translates into a degeneration in the spectrum of hadrons. The classic QCD Lagrangian has an apparent $U(1)_A$ symmetry that is not realized in the real world since it does not produce a corresponding hadronic light state.

This is known as the $U(1)$ problem, discussed by S. Weinberg in Ref. [177]. G. 't Hooft solved this problem by realizing that the vacuum of QCD has a non-trivial structure that allows a CP violating term in the QCD Lagrangian [178]. However, we do not observe CP violation in experiments, therefore the parameter governing this term must be extremely small, fine tuned. This is known as the strong CP problem. Axions arise from the Peccei-Quinn mechanism, a possible solution of the strong CP problem [179].

The strong CP problem, the Peccei-Quinn mechanism, axion-like particles and axions as dark matter candidates are briefly discussed in Section 4.1. A summary of the current limits on the photon-ALPs coupling constant and ALPs mass is given in Section 4.3. In Section 4.2, we introduce the photon-ALPs oscillations under a homogeneous magnetic field.

4.1 AXIONS AND AXION-LIKE PARTICLES

4.1.1 The Peccei-Quinn mechanism

In this section we follow the review given in Ref. [179] and references therein. The complex vacuum structure of non-Abelian gauge theories leads to an additional term in the QCD Lagrangian,

$$\mathcal{L}_\theta = \theta \frac{g_s^2}{32\pi^2} G^{\mu\nu} \widetilde{G}_{\mu\nu}, \tag{4.1.1}$$

where g_s is the strong coupling, $G_{\mu\nu}$ is the gluon tensor and its dual $\widetilde{G}^{\mu\nu} = 1/2\epsilon^{\mu\nu\rho\sigma} G_{\rho\sigma}$ and θ is a free parameter. Including the weak interactions, the quark mass matrix $\mathcal{M}$ must be diagonalized in order to have a physical representation. The coefficient of the Lagrangian becomes:

$$\overline{\theta} = \theta + \arg\det \mathcal{M}. \tag{4.1.2}$$

The existence of this term causes the electron dipole moment of the neutron to be $d_n \simeq e\theta m_q / m_N^2$ [180], where e is the electric charge, m_q is the mass of the quark and m_N is the mass of the neutron. Experimental results show that $d_n < 3 \cdot 10^{-26} e$ cm. This bound implies that $|\overline{\theta}| \lesssim 10^{-10}$. This is called the *"strong CP problem"*, there is no natural explanation for the fine tuning of the parameter $\overline{\theta}$ that preserves the CP symmetry in QCD. The strong CP problem remains as one of the unsolved problems in physics.

A solution for this problem was proposed by Peccei & Quinn in 1977, by including an

additional global $U(1)_{PQ}$ symmetry to the QCD Lagrangian [181]. This $U(1)_{PQ}$ symmetry turns the fixed parameter $\bar{\theta}$ into a dynamic field. If the symmetry is spontaneously broken, a pseudo Nambu-Goldstone boson arises, the axion. The full Lagrangian of the theory then reads:

$$\mathcal{L} = \mathcal{L}_{SM} + \bar{\theta}\frac{g_s^2}{32\pi^2}G^{\mu\nu}\widetilde{G}_{\mu\nu} + \mathcal{L}_{PQ}, \tag{4.1.3}$$

$$\mathcal{L}_{PQ} = -\frac{1}{2}\partial_\mu a \partial^\mu a + \mathcal{L}_{int}\left[\partial^\mu a/f_a, \Psi\right] + \xi\frac{a}{f_a}\frac{g_s^2}{32\pi^2}G^{\mu\nu}\widetilde{G}_{\mu\nu}, \tag{4.1.4}$$

where Ψ is any field in the theory, ξ is a model dependent parameter, f_a is the symmetry breaking scale and a is the axion field. Under the Peccei-Quinn (PQ) transformation, the axion field changes like $a(x) \to a(x) + \alpha f_a$, where α is the phase parameter of the transformation. The last term in Eq. 4.1.4 acts as an effective potential for the axion field. The minimum occurs at:

$$\left\langle \frac{\partial V_{eff}}{\partial a} \right\rangle = -\xi\frac{1}{f_a}\frac{g_s^2}{32\pi^2}\left\langle G^{\mu\nu}\widetilde{G}_{\mu\nu}\right\rangle = 0 \tag{4.1.5}$$

This equation is satisfied by the vacuum expectation value of the axion $\langle a\rangle = -\bar{\theta}f_a/\xi$. With this value, the $\bar{\theta}$ term dynamically cancels out, solving the strong CP problem.

In the original PQ model, the QCD Lagrangian needed two Higgs doublets, Φ_1 and Φ_2, in order to make the theory invariant under the PQ symmetry. The axion in this model is the phase field of both Higgs fields:

$$\Phi_1 = \frac{v_1}{\sqrt{2}}\begin{bmatrix}1\\0\end{bmatrix}\exp\left(i\frac{v_2}{v_1}\frac{a}{f_a}\right) \qquad \Phi_1 = \frac{v_2}{\sqrt{2}}\begin{bmatrix}0\\1\end{bmatrix}\exp\left(i\frac{v_1}{v_2}\frac{a}{f_a}\right). \tag{4.1.6}$$

In this equation, v_i are the Higgs vacuum expectation values and $f_a = \sqrt{v_1^2 + v_2^2} \simeq v = 250$ GeV, a value very close to the electroweak scale v. Different axion models can be obtained by changing the way in which the Higgs doublets couple to quarks and leptons in the SM Lagrangian [182].

The original Peccei-Quinn model and models that rely on this method have been ruled out by experiments (see e.g. Ref [183]). In principle, any value of f_a can still work for the dynamical cancellation of $\bar{\theta}$. *Invisible* axion models assume that $f_a \gg v$. Due to the relation between the axion mass and the symmetry breaking scale $m_a \sim 1/f_a$, axions in these models are very light and have a weak coupling. In addition, the decay of axions into photons depends on $\sim f_a^5$, which also makes them very stable. Another consequence

of $f_a \gg v$ is that only $SU(2) \times U(1)$ singlets can break the PQ symmetry. The axion then arises as the phase of the complex scalar field σ associated to $SU(2) \times U(1)$.

Two types of models have been proposed within this context, the Kim–Shifman–Vainshtein–Zakharov (KSVZ) [184] and the Dine–Fischler–Srednicki–Zhitnitsky (DFSZ) [185, 186] models. KSVZ axion models assume that the quark and leptons are PQ singles and that the σ field interacts with new heavy quarks Q through the Yukawa coupling. These new quarks carry the charge associated to the PQ symmetry. In contrast, DFSZ axion models do not add new quarks. Existing quarks and leptons carry the PQ charge and they interact with the axion only through other interactions that σ has with two new Higgs fields.

4.1.2 Axion-like particles

The SM provides a satisfactory characterization of the interactions of elementary particles. However, problems like the inclusion of gravity or the compelling evidence for the existence of dark matter in the Universe indicate that the theory is incomplete [187]. In theoretical physics, the SM is viewed as the low-energy limit of a more complete and fundamental theory of particle interactions. Axion-like particles are predicted by many of those fundamental theories and also arise as pseudo Nambu-Goldstone bosons from the breaking of different $U(1)$ symmetries. Theories such as supersymmetry models, Kaluza-Klein theories and superstring theories, predict the existence of ALPs [188, 189, 190, 191, 192, 193].

The ALPs Lagrangian is,

$$\mathcal{L} = \frac{1}{2}\partial^{\mu}a\partial_{\mu}a - \frac{1}{2}m^2a^2 - \frac{1}{4}g_{a\gamma}F_{\mu\nu}\tilde{F}^{\mu\nu}a, \tag{4.1.7}$$

where $g_{a\gamma}$ is the axion-photon coupling strength, m is the mass of the ALP and $F_{\mu\nu}$ is the electromagnetic tensor. The interaction of ALPs with Standard model particles is described by the last term of Eq. 4.1.7, from which we can see that ALPs only mix with photons. In the case of axions, the coupling constant is $g_{a\gamma} = \alpha g_{\gamma}/\pi f_a$, where g_{γ} is a model-dependent parameter. The mass and the coupling constant for ALPs are completely unrelated. Furthermore, rewriting the photons-ALP vertex in terms of the electric field $\mathbf{E}$ and the magnetic field $\mathbf{B}$ yields,

$$\mathcal{L}_{a\gamma} = -\frac{1}{4}g_{a\gamma}F_{\mu\nu}\tilde{F}^{\mu\nu}a = g_{a\gamma}\mathbf{E}\cdot\mathbf{B}a. \tag{4.1.8}$$

Eq. 4.1.8 is the cornerstone of ALP searches, since it implies that photons can mix with ALPs in the presence of electromagnetic fields. More specifically, off-diagonal elements in the mass matrix for the photon-ALP system appear, making the interaction eigenstates different from the propagation eigenstates. Parallel to neutrino oscillations, photon-ALP oscillations occur in the system [194]. ALPs are pseudo-scalar particles and thus have spin zero, whereas neutrinos have the same spin so oscillations can happen in vacuum. The spin discrepancy between photons and ALPs has to be compensated by external magnetic fields.

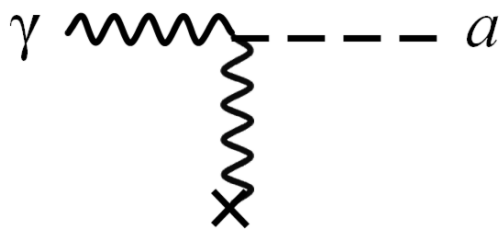

Figure 4.1.1: Feynman diagram of the photon-ALPs mixing. A photon turns into an ALP in the presence of a virtual photon from a magnetic field. Adapted from Ref. [195].

Figure 4.1.2 shows a diagrammatic representation of ALPs oscillations. In this scenario, photons emitted by sources can turn into ALPs while traveling in a magnetic region. Photons that oscillate do not interact with other SM particles and thus can traverse regions in which they would normally be absorbed. ALPs can convert back into photons in the presence of the same or a different magnetic field. The photon-ALP beam propagation will be treated in depth in Section 4.2.

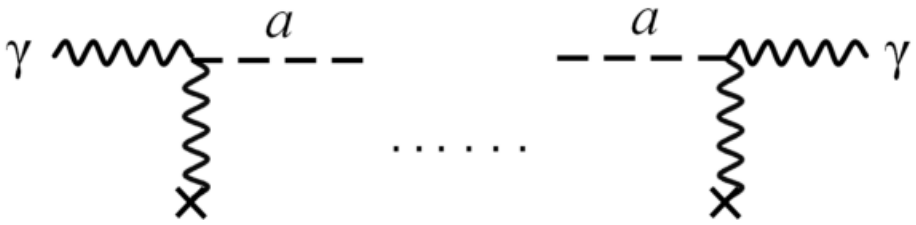

Figure 4.1.2: Diagram of photon-ALPs oscillations. A photon turns into an ALP in the presence of a virtual photon and oscillates back and forth. Adapted from Ref. [195].

4.1.3 Axions as dark matter candidates

Dark matter remains as one of the most important unsolved mysteries in physics. Among different approaches, the most probable candidates to explain the nature of dark matter are non-baryonic particles from theories beyond the SM. These particles are expected to have observational features due to annihilation or decay into SM particles.

Structure formation in the Universe suggests that the majority of dark matter is cold. The most popular dark matter candidates are Weakly Interacting Massive Particles (WIMPs), like the supersymmetric neutralino. Another well-motivated candidate is the axion, which has the additional advantage of solving the strong CP problem. In the rest of the section we follow the review of the axion cosmology found in Ref. [196].

Axions in the early Universe can be produced by thermal and non-thermal mechanisms. Among other processes, thermal axions come from reactions such as $q + g \rightarrow q + a$, where q and g stand for quark and gluon, respectively [197]. Non-thermal or cold axion contributions are expected to come from the vacuum misalignment mechanism [198, 199, 196] and decays of topological defects, such as cosmic axion strings and domain walls [200].

When the temperature T becomes of the order of the QCD scale parameter Λ_{QCD}, QCD instanton effects align the vacuum, producing a coherent state of non-relativistic axions. This is called the vacuum realignment mechanism. The potential for the axion field $\phi(x)$ due to the non-perturbative QCD effects is,

$$V_a = m_a(t)^2 f_a^2 \left[1 - \cos\left(\frac{\phi(x)}{f_a}\right)\right], \tag{4.1.9}$$

where the mass depends on the time t after the Big Bang. The critical time in which the axion potential turns on its mass, and it arises as the quanta of oscillation of its field, is $t_1 \simeq 2 \cdot 10^{-7} (f_a/10^{12}\text{GeV})^{1/3}\text{s}$. The average number density of axions at that time is $n_a(t_1) \simeq \pi f_a^2 t_1^{-1}$. The produced number of cold dark matter axions at a time t is,

$$n_a(t) \simeq \frac{4 \cdot 10^{47}}{\text{cm}^3} X \left(\frac{f_a}{10^{12}\text{GeV}}\right)^{5/3} \left[\frac{R(t_1)}{R(t)}\right]^3, \tag{4.1.10}$$

where $R(t)$ is the scale factor of the Universe and X is a fudge factor that depends on topological defects contributions and inflation. This factor changes if inflation happens before or after the PQ phase transition.

After they obtain mass, axions would have very small momenta compared to the temperature of the surrounding plasma, $T = 1$ GeV. This is one of the criteria necessary for cold dark matter, a non-relativistic population of axions, which could be produced in sufficient quantities to reach the required dark matter energy density. On the other hand, large values of f_a imply low decay times and weak couplings, which is the second requirement for a good dark matter candidate, weak couplings lead to effectively collisionless axions with the gravitational force being the only significant interaction.

Recent works explore also the possibility of cold dark matter axions forming Bose-Einstein condensates after thermalizing through their gravitational self-interactions [201]. As a result, axion dark matter differs from other WIMPs models, with consequences for the production of rotation in dark matter halos.

Nowadays, axion dark matter is predicted to be in the Milky Way in the form of a large halo of particles moving with relative velocities of the order of 10^{-3} c. They would have to be moving at speeds smaller than $\sim 2 \cdot 10^{-3}$ c, in order to be bound in our Galaxy [202].

4.2 PHOTON-ALPS OSCILLATIONS

Axion-like particles interaction with SM particles is characterized by the $a\gamma\gamma$ vertex in the Lagrangian. In analogy to neutrinos, the interaction eigenstates of the photon-ALP system are different from the propagation eigenstates, leading to the phenomenon of oscillations. The spin mismatch between a pseudo-scalar particle and a photon has to be compensated by an external magnetic field. In the rest of this section we will follow Refs. [203].

Let us consider the propagation of a photon with wave vector $\mathbf{k}$. The electric field of the photon is denoted by $\mathbf{E}$, while the external magnetic field can be split in two components, the longitudinal $\mathbf{B_L}$ and the transversal $\mathbf{B_T}$, along the propagation direction. Since $\mathbf{E}$ is perpendicular to $\mathbf{k}$, we find that the Lagrangian is reduced to $\sim a\mathbf{E} \cdot \mathbf{B_T}$, hence only the transverse component of the magnetic field is relevant for the mixing. Furthermore, we can separate $\mathbf{E}$ into $\mathbf{E}_\parallel$ and $\mathbf{E}_\perp$, the parallel and orthogonal components of the electric field along the plane spanned by $\mathbf{k}$ and $\mathbf{B}$, reducing the interaction

to $\sim a\mathrm{E}_{\parallel}\mathrm{B}_{\mathrm{T}}$. Not only the mixing only happens with the transverse component of the magnetic field but it solely affects linearly polarized photons along the direction of $\mathrm{E}_{\parallel}$. The latter is used to search for ALPs in polarization experiments.

The photon-ALP propagation for a monochromatic system along the y-axis can be described by [204],

$$\left(\partial_y^2 + E^2 + 2E\mathcal{M}_0\right)\psi(y) = 0 \tag{4.2.1}$$

where E is the photon energy, $\mathcal{M}_0$ is the mixing matrix and $\psi(y)$ is the beam state vector,

$$\psi(y) = \begin{pmatrix} A_x(y) \\ A_z(y) \\ a(y) \end{pmatrix} = A_x(y)\left|\gamma_x\right\rangle + A_z(y)\left|\gamma_z\right\rangle + a(y)\left|a\right\rangle. \tag{4.2.2}$$

The photon polarization amplitudes along the x- and z-axis are denoted by $A_x(y)$ and $A_z(y)$, respectively, while the ALP field amplitude is $a(y)$ and the basis $\{\left|\gamma_x\right\rangle, \left|\gamma_z\right\rangle, \left|a\right\rangle\}$ is given by the unitary vectors:

$$\left|\gamma_x\right\rangle = \begin{pmatrix} 1 \\ 0 \\ 0 \end{pmatrix} \qquad \left|\gamma_z\right\rangle = \begin{pmatrix} 0 \\ 1 \\ 0 \end{pmatrix} \qquad \left|a\right\rangle = \begin{pmatrix} 0 \\ 0 \\ 1 \end{pmatrix}. \tag{4.2.3}$$

Eq. 4.2.1 can be linearized for high photon energies $E \gg m_a$, or wavelengths much smaller than the length of the magnetic field, this is known as the *short-wavelength approximation* [205] :

$$\left(i\partial_y + E + \mathcal{M}_0\right)\psi(y) = 0. \tag{4.2.4}$$

Hence the photon-ALP system propagation problem can be reduced to a non-relativistic quantum system in three dimensions. In fact, it is a Schrödinger-like equation with time as the propagation direction and Hamiltonian $H_0(y) = -(E+\mathcal{M}_0(y,E))$. The evolution of the system is thus described by the transfer matrix $U(y,y_0)$ for an initial state at y_0. This matrix can be factorized as,

$$U(y,y_0) = e^{iE(y-y_0)}\mathcal{U}(y,y_0), \tag{4.2.5}$$

where $\mathcal{U}(y,y_0)$ is the transfer matrix of the reduced system $\left(i\partial_y + \mathcal{M}_0\right)\psi(y) = 0$. The conversion probability $P_{\gamma a}$ is then evaluated as the probability of the quantum mechanical transition between two states. For the final state we need the transfer matrix.

The mixing matrix is real and symmetric, and it involves different terms. The general

form is given by:

$$\mathcal{M}_0 = \begin{pmatrix} \Delta_{xx} & \Delta_{xz} & \Delta^x_{a\gamma} \\ \Delta_{zx} & \Delta_{zz} & \Delta^z_{a\gamma} \\ \Delta^x_{a\gamma} & \Delta^z_{a\gamma} & \Delta_{aa} \end{pmatrix}. \tag{4.2.6}$$

In Eq. 4.2.6, the $\Delta_{a\gamma}$-terms and the Δ_{aa}-term represent the mixing of photons with ALPs and ALPs self-interaction, respectively. The remaining terms depend on the properties of the medium, namely QED vacuum effects and absorption mechanisms. The former come from the Heisenberg-Euler-Weisskopf (HEW) effective Lagrangian for the photon one-loop vacuum polarization under an external magnetic field [206]:

$$\mathcal{L}_{\rm HEW} = \frac{2\alpha^2}{45m_e^4}\left[\left(\mathbf{E}^2 - \mathbf{B}^2\right) + 7\left(\mathbf{E}\cdot\mathbf{B}\right)^2\right], \tag{4.2.7}$$

where α is the fine structure constant and m_e is the electron mass. Vacuum QED terms can be ignored at high energies. The other contribution is due to background particles in the medium that may annihilate the primary photon, such as EBL.

To illustrate the oscillation phenomenon we will first derive the solutions for beam in a pure polarization state, propagating through the y-axis in the presence of a homogeneous magnetic field. The mixing matrix can be reduced to:

$$\mathcal{M}_0 = \begin{pmatrix} \Delta_{xx} & 0 & 0 \\ 0 & \Delta_{zz} & \Delta^z_{a\gamma} \\ 0 & \Delta^z_{a\gamma} & \Delta_{aa} \end{pmatrix}. \tag{4.2.8}$$

The Δ_{xz}-terms vanish because Faraday rotation effects are not relevant at high energies. The $\Delta^x_{a\gamma}$-terms disappear due to a choice coordinates in which $\mathbf{B_T}$ is homogeneous along the z-axis, with B_x= 0. The ALPs mixing terms are:

$$\Delta^z_{a\gamma} = \frac{g_{a\gamma}B_T}{2} \qquad \Delta_{aa} = -\frac{m_a^2}{2E}. \tag{4.2.9}$$

The Δ_{xx} and Δ_{zz} terms depend on other factors present in the medium. They are described by,

$$\Delta_{xx} = \Delta_{zz} = \Delta_{pl} + \Delta_{abs} = -\frac{w_{pl}^2}{2E} + \frac{i}{2\lambda_\gamma(E)}. \tag{4.2.10}$$

The first contribution, Δ_{pl}, arises from the fact that the beam propagates through cold plasma, in which the photon obtains an effective mass. The resulting plasma frequency

is,

$$w_{pl} = \sqrt{\frac{4\pi\alpha}{m_e} n_e}, \tag{4.2.11}$$

where n_e is the electron density of the medium. The second contribution comes from absorption mechanisms, such us pair production with other background photons, which yields a photon mean free path $\lambda_\gamma(E)$.

The conversion probability for a photon turning into an axion is computed by the transition probability between the initial and final states of the beam,

$$P_{\gamma\to a}(y) = \left|\langle a \left|\mathcal{U}(y, y_0)\right| \gamma_z\rangle\right|^2 \tag{4.2.12}$$

The phase of the full transfer matrix cancels out and we only have to compute the transfer matrix of the reduced system. In order find it, we have to solve a system of first order differential equations,

$$\partial_y \psi(y) = i\mathcal{M}_0 \psi(y), \tag{4.2.13}$$

whose solution is well known:

$$\psi(y) = \sum_{i=1}^{3} c_i e^{i\lambda_i (y-y_0)} V_i \qquad \mathcal{U}(y, y_0) = \sum_{i=1}^{3} e^{i\lambda_i (y-y_0)} T_i \tag{4.2.14}$$

In these equations, c_i are arbitrary constants obtained with the initial condition $\psi(y_0)$, λ_i are the eigenvalues of the mixing matrix, V_i are its eigenvectors, and T_i are matrices explicitly worked out in Ref. [203]. Ignoring Δ_{abs} contributions and for a beam that departs from y_0, the conversion probability from Eq. 4.2.12 is

$$P_{\gamma\to a}(y, E) = \left(\frac{g_{a\gamma} B_T}{\Delta_{osc}(E)}\right)^2 \sin^2\left(\frac{\Delta_{osc}(E)\,(y - y_0)}{2}\right), \tag{4.2.15}$$

where the oscillation term is given by

$$\Delta_{osc}(E) = \left\{\left(\frac{m_a^2 - w_{pl}^2}{2E}\right)^2 + \left(g_{a\gamma} B_T\right)^2\right\}^{1/2}. \tag{4.2.16}$$

The behavior of Equation 4.2.15 depends on the critical energy of the mixing. In units

of GeV, this quantity is defined as [207]:

$$E_c \sim 2.5 \frac{|m^2_{a,neV} - \omega^2_{pl,neV}|}{2 g_{11} B_{T,\mu G}} \,\mathrm{GeV}, \tag{4.2.17}$$

where the units of the parameters have been adjusted, $g_{11} = g_{a\gamma}/10^{-11}\mathrm{GeV}^{-1}$. If $E \lesssim E_c$, $P_{\gamma\to a}(E)$ displays an oscillatory nature, which is different from the oscillations in the y-axis, fixed now. For this specific magnetic morphology, these oscillations are too small to be observed, but they can be enhanced for intra-cluster magnetic fields, as seen in Ref. [207]. If $E \gg E_c$, the conversion probability is maximal and independent on the energy,

$$P_{\gamma\to a}(y) \simeq \sin^2\left(\frac{g_{a\gamma} B_T \,(y - y_0)}{2}\right). \tag{4.2.18}$$

In this strong mixing regime, a significant part of photons is converted to axions, which can evade absorption mechanisms and convert back to photons under a different magnetic field. Both regimes can be seen in Fig. 4.2.1. Notice that this solution is only for pure polarization beams traveling in a homogeneous magnetic field and cannot be applied directly to cosmic magnetic fields or photons emitted from a γ-ray source.

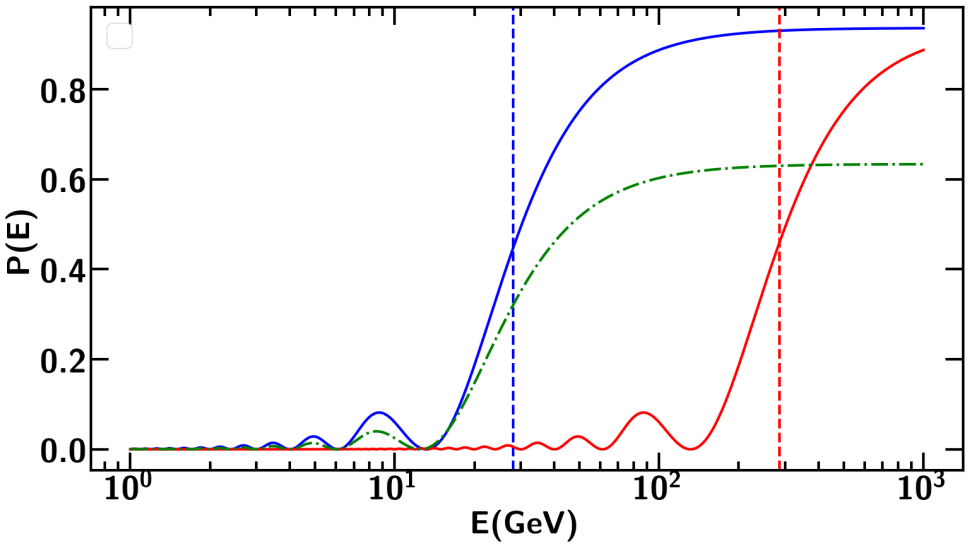

Figure 4.2.1: Photon-ALP conversion probability as a function of energy for some arbitrary parameters. **Blue**: probability for some arbitrary parameters (solid) and critical energy (dashed). **Red**: probability increasing the ALP mass (solid) and its corresponding shifted critical energy (dashed). **Green**: probability decreasing the product $B \cdot y$.

Examples of photon-ALPs conversion probabilities are displayed in Fig. 4.2.1. The solid lines are the probabilities for their corresponding critical energies, shown as dashed lines of the same color. Fixing all the parameters and increasing the ALP mass, makes Eq. 4.2.15 shift toward higher energies. For the dash-dotted line, we fix the parameters of the blue case and decrease only the product $B \cdot y$. This quantity regulates the amplitude of the conversion, if it is too small, the oscillations are not detectable.

However, astrophysical environments do not have perfectly homogeneous magnetic fields and current γ-ray telescopes are not designed to measure photon polarization due to technical challenges. Additionally, photon polarization depends on the emission mechanisms (described in Section 2.1) that are still under active research [208]. See Ref. [209] for an estimate of the sensitivity of the *Fermi*-LAT to γ-ray polarization.

All things considered, the photon-ALP beam has to be treated as unpolarized and general non-homogeneous magnetic fields need to be taken into account. The former

means that the wave equation $\psi(y)$ cannot be used. Instead, the beam is described by a polarization density matrix,

$$\rho(y) = \begin{pmatrix} A_x(y) \\ A_z(y) \\ a(y) \end{pmatrix} \otimes \begin{pmatrix} A_x(y) & A_z(y) & a(y) \end{pmatrix}^*, \tag{4.2.19}$$

that obeys the Von Neumann equation of non-relativistic quantum mechanics [203],

$$i\partial_y \rho = [\rho, \mathcal{M}] = \rho\mathcal{M}^\dagger - \mathcal{M}\rho, \tag{4.2.20}$$

where $\mathcal{M}$ is the mixing matrix. Again, the solution of the propagation of the beam is given by the transfer matrix,

$$\rho(y) = \mathcal{U}(y, y_0)\rho(y_0)\mathcal{U}^\dagger(y, y_0). \tag{4.2.21}$$

The transition probability from one state to another state is given by the trace of the projection of both states,

$$P_{\rho_1 \to \rho_2} = \mathrm{Tr}\left(\rho_2 \mathcal{U}(y, y_0)\rho_1 \mathcal{U}^\dagger(y, y_0)\right). \tag{4.2.22}$$

In order to deal with non-homogeneous magnetic fields, the magnetic region are often split into N domains with a homogeneous field in each one. In this case, $\mathbf{B_T}$ can no longer be aligned with the z-axis, but the problem can be simplified through similarity transformations,

$$\mathcal{M} = V^\dagger(\psi)\mathcal{M}_0 V(\psi), \tag{4.2.23}$$

where $V(\psi)$ is the rotation matrix in the $x - z$ plane perpendicular to the propagation direction and ψ is the angle $\mathbf{B_T}$ forms with the z-axis in each domain. See Ref. [203] for a whole derivation of the solutions under a general angle ψ. The full transfer matrix of the system across N domains is,

$$\mathcal{U}(E_0, z, \psi_1 ... \psi_N) = \prod_{i=1}^{N} \mathcal{U}(E_i, \psi_i) \tag{4.2.24}$$

The probability of transition between two states is then computed with Eqs. 4.2.22 and 4.2.24. If the magnetic field orientations are random in each domain, the propagation becomes a stochastic process and only the mean properties of the beam can be evaluated

over a large number of configurations. On the other hand, due to the lack of polarization measurements, we have to sum over the two final polarization states in order to compute a photon survival probability. Taking into account these two conditions, the probability of transition for a photon going to a photon, or photon survival probability, is,

$$P_{\gamma\to\gamma}(E_0, z) = \sum_{i=1,2} \mathrm{Tr}\left(\left\langle \rho_i \mathcal{U}(E_0, z, \psi_1 ... \psi_N) \rho_{\mathrm{unpol}} \mathcal{U}^\dagger(E_0, z, \psi_1 ... \psi_N) \right\rangle\right)_{\psi_1 ... \psi_N} . \quad (4.2.25)$$

4.3 EXPERIMENTAL SEARCHES

After several years from its theoretical proposition, the axion remains as a solid dark matter candidate and as a possible solution for the strong CP problem. It has motivated a wide variety of experiments built upon its mixing to photons in electromagnetic fields. These searches are divided in three categories, namely laboratory, astrophysical and cosmological.

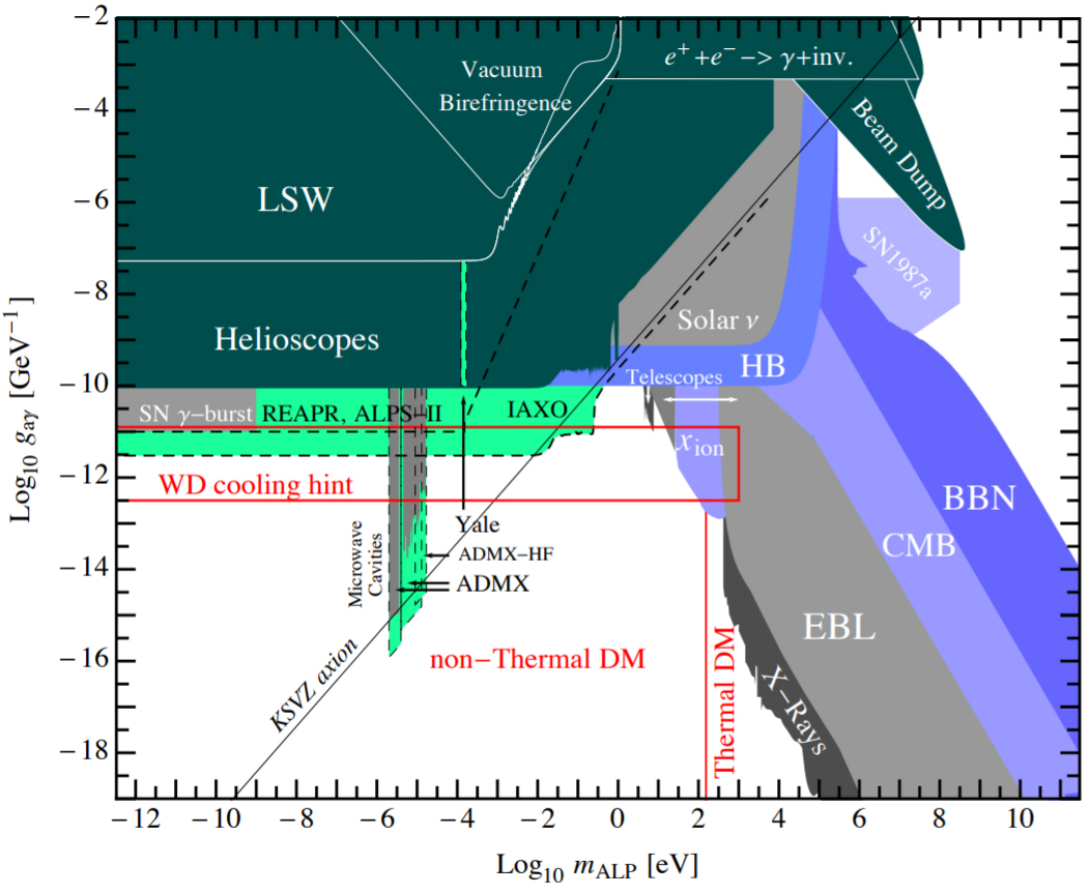

Figure 4.3.1: Parameter space of ALPs mass and photon-ALPs coupling. Light green regions represent expected sensitivities of future experiments. The rest of the shaded areas represent excluded parameters. The constraints were derived from laboratory, astrophysical and cosmological experiments, see the text for more information. The solid black line is for the invisible KSVZ axion model. Adapted from Ref. [210].

In this section, we summarize the current exclusion regions and expected sensitivities for ALPs in the $(m_a, g_{a\gamma})$ parameter space, displayed in Fig. 4.3.1. Reviews of this topic can be found in, e.g. Refs. [210, 211].

4.3.1 Laboratory experiments

Light shining through a wall

Light-shining-through-a-wall (LSW) experiments search for any kind of Weakly Interacting Sub-eV Particles (WISP), such as ALPs. [212]. These experiments send a laser beam through an opaque wall in the presence of a magnetic field. Due to Eq. 4.2.15, these photons could be converted into axions before the light-absorbing barrier, in the first magnetic region. If there is another magnetic region in the other side of the wall, ALPs that survive could convert back to photons. This is the laboratory analogy to the γ-ray opacity induced by the EBL in the Universe. The schematic process is shown in Fig. 4.3.2.

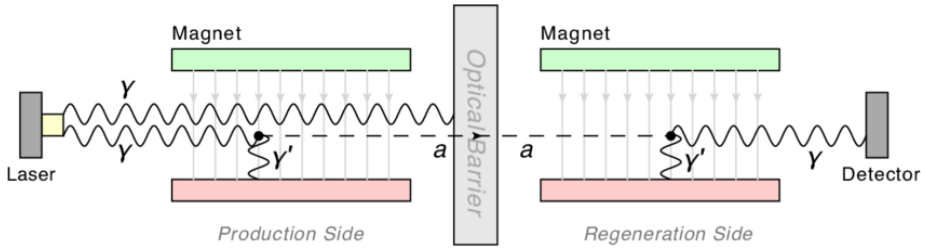

Figure 4.3.2: Schematics of the LSW experimental setups. A photon beam is emitted by a laser. Photons can convert into ALPs in the production region due to the magnetic field generated by the magnet (green) and pass through the optical barrier, and then ALPs may convert back to photons for detection. Adapted from `https://alps.desy.de/`.

Examples of LSW experiments are ALPS I (Any Light Particle Search) and OSQAR (The Optical Search for QED Vacuum Bifringence, Axions and Photon Regeneration). ALPS I was located at DESY Hamburg and was active from 2007 to 2010. In that time, ALPS I was able to probe a wide part of the ALPs parameter space due to the first successful integration of a large-scale optical resonator in the experimental setup, which allowed to amplify the photon flux in the production region and increase the sensitivity. ALPS II will upgrade the magnetic fields, laser power and detection system in order to improve the sensitivity by a few orders of magnitude for all the particles, as shown in Fig. 4.3.1. The non-detection of axion signals in LSW experiments resulted in bounds on the parameter space [213], labeled as "LSW" in Fig. 4.3.1.

Polarization effects

In Section 4.2, we saw that the photon-ALPs mixing strongly depends on the polarization state of the initial photon, opening up the possibility to search for ALPs observing changes in polarization of a laser beam in a magnetic field. The limits, derived by the PVLAS collaboration [214], are labeled as "vacuum birefringence" in Fig. 4.3.1. The sensitivity of polarization experiments is limited by the QED vacuum birefringence polarization effect [215]. This type of experiments is schematically represented in Fig. 4.3.3.

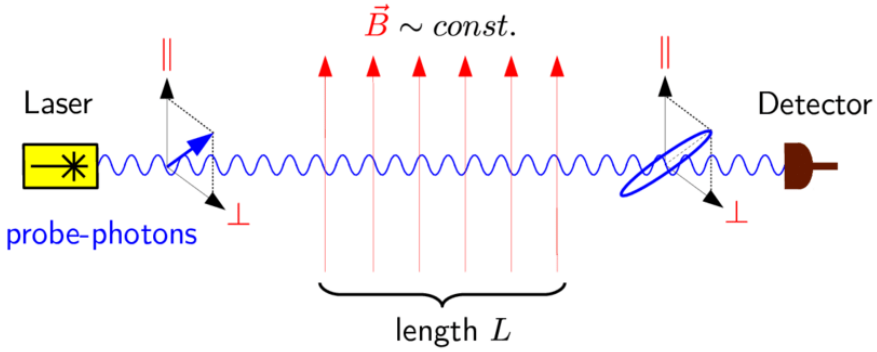

Figure 4.3.3: Setup of the polarization experiments. A laser beam is sent through a magnetic field in vacuum. The beam polarization changes due to ALPs and the QED vacuum birefringence. Adapted from Ref. [216].

Beam dumps

Proton or electron beam dump experiments constitute another method to search for ALPs in laboratories [217]. In these experiments, ALPs could be produced via the Primakoff process (see Fig. 4.3.4) after a coherent beam of particles collides with a target material composed of atoms with heavy nuclei. The production can be enhanced with heavier target nuclei and the cross-section can be easily computed for the process.

Bounds from these experiments are shown in the upper-right side of Fig. 4.3.1, labeled as "Beam Dump". The SHiP experiment proposal aims to improve the sensitivities of current beam dump experiments [218], searching for a wide variety of light weakly-coupled particles with high intensity beams.

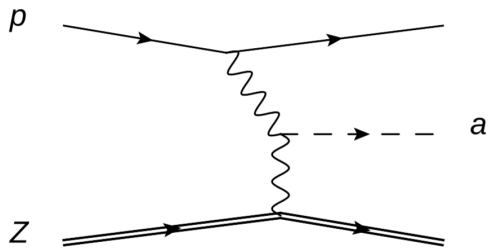

Figure 4.3.4: Primakoff effect for ALPs in proton-nucleon scattering. Adapted from Ref. [217].

4.3.2 Astrophysical searches

Cosmological bounds

Complementary bounds can also be derived from observable cosmological parameters [219]. In addition to the non-thermal ALPs population coming from the realignment mechanism, a thermal population of ALPs is also created in the early Universe. At some point, these ALPs decouple from the other SM particles, with an impact on cosmological events such as the big bang nucleosynthesis (BBN). The two relevant processes are the Primakoff process and ALPs decay into photons. If ALPs decay sufficiently early, they constitute an additional source of photon injection in the primordial plasma that dilute the baryon and neutrino densities. For instance, the neutron to proton ratio, n/p, depends on the $p + e^- \leftrightarrow n + \nu_e$ reaction freeze-out time. If ALPs exist, the process becomes ineffective sooner and thus the n/p ratio changes. Combined bounds from abundances and the neutrino density measured by the WMAP are shown in Fig. 4.3.1, labeled as "BBN". The characteristic slope of these limits mainly depends on the ALPs population decay time $\tau = 65\pi/(m_a^3 g_{a\gamma}^2)$.

Decays that take place after recombination, when the Universe becomes transparent to radiation, can also be used to constraint the ALPs parameter space. The photon flux due to the decay of a diffuse ALP population [220] contributes to the intensity of extragalactic background light. Limits from the absence of ALPs in the EBL [221] are labeled as "EBL" in Fig. 4.3.1. Limits derived from the lack of distortions on the CMB spectrum due to ALPs [222] are shown as "CMB". The same authors also

looked for ALPs decays as galactic lines, with the limits shown as "X-rays" in the limits plot. Finally, the injected photons can re-ionize the primordial hydrogen, producing free electrons that interact with the CMB photons and increase their optical depth. Limits on the re-ionization fraction x_{ion} were also derived using WMAP data [219].

Helioscopes

Photons and charged particles are available in large quantities in the stellar interiors, and therefore we expect a flux of axions or ALPs from stars [223]. Helioscopes, such as CAST (CERN Axion Solar Telescope), search for ALPs by pointing a magnet towards the sun. If ALPs exist, they could convert back to photons within the interior of the region surrounded by the magnet. Fig. 4.3.5 shows a schematic representation of the setups.

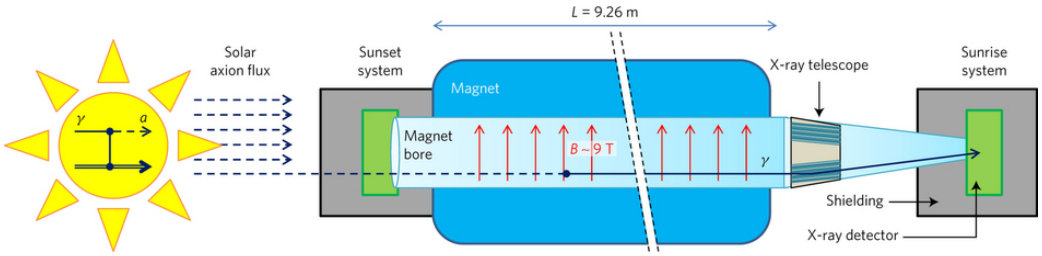

Figure 4.3.5: Schematic representation of the CAST experiment. Solar axions are produced by the Primakoff process inside the star and can be converted to X-ray photons within a strong magnetic on Earth. Adapted from Ref. [224]

Upper limits on the photon-ALPs coupling have been derived using CAST data and improved recently by the CAST collaboration [224]. These limits are shown as "Helioscopes" in the constraints from Fig. 4.3.1. The International Axion Observatory (IAXO) is a proposed new axion helioscope built to detect axions and other similar particles emitted by the Sun [225]. The expected sensitivity is also displayed in Fig. 4.3.1, in the light green shaded region labeled as "IAXO".

Haloscopes

Haloscopes, invented by P. Sikivie in 1983 [226], are instruments that consist of a resonant microwave cavity within a superconducting magnet in which axions can convert to

photons in the presence of the magnetic field. The signal is enhanced when the photon's frequency corresponds to the resonant frequency of the cavity. These experiments are used to search for cold dark matter axions from the galactic dark matter halo. The Axion Dark Matter eXperiment (ADMX), built in 1995 and located at the Center for Experimental Nuclear Physics and Astrophysics (CENPA), is an example of haloscope [227].

ADMX has been able to set mass constraints from 1.9 - 3.65 μeV [228]. At present, ADMX is undergoing an upgrade that will allow an enhanced sensitivity to reach a wide range of possible dark-matter axion parameter space [229]. The limits and expected sensitivities are shown as "Microwave Cavities" in Fig. 4.3.1.

Stellar energy loss effects

If ALPs exist, stars would have an additional energy loss channel due to the large mean free paths of these particles. More energy loss channels imply a modified stellar evolution, shortening the lives of stars [230]. A detailed derivation of the emission rates and axion processes in stars can be found in Ref. [231]. ALPs can be produced via the Primakoff process, whereas axions have additional contribution diagrams due to their coupling to fermions. As a consequence of energy loss, the production of ALPs would change the temperature of the star, leading to a boost in the neutrino flux. This enhanced flux can be measured to set limits on ALPs. The Solar Neutrino Observatory (SNO) derived upper limits based on this process [232], labeled in Fig. 4.3.1. as "Solar ν".

Globular clusters are gravitationally-bound systems of stars with similar formation times and masses, typically below one solar mass. These systems provide a good scenario for studying stellar evolution. Stars on the horizontal branch (HB) have reached the stage of helium burning, in which energy is generated fusing helium and creating heavier elements [233]. The additional Primakoff energy loss rate implies an accelerated consumption of helium that shortens the lifetime of such stars [223]. Measurements of the HB stars lifetimes in globular clusters have led to axion exclusion limits comparable to the CAST limit but extending to higher masses [234]. These constraints are shown in 4.3.1 under the "HB" label. Additionally, stars on the red-giant branch (RGB), can have helium ignition delayed by axion-electron interactions, setting limits on axion-electron coupling [235].

White dwarfs are the degenerate stellar core remnants produced at the end of the lives of low-mass red giant stars. The evolution of their luminosity comes from the emission of thermal energy, thus it is described by a cooling process. Axions would contribute to the cooling of such objects, allowing us to set constraints from the observation of white-dwarfs luminosity functions on the Yukawa coupling of axions [236, 237].

Neutron stars

Axions could also be produced by nucleon-nucleon Bremsstrahlung, see Fig. 4.3.6, in the interior of neutron stars. An increase in the axion flux from $1-150$ MeV is expected from this process, leading to a modification in the γ-ray spectra of the sources in that energy range. Limits were derived in Ref. [238] with *Fermi*-LAT data.

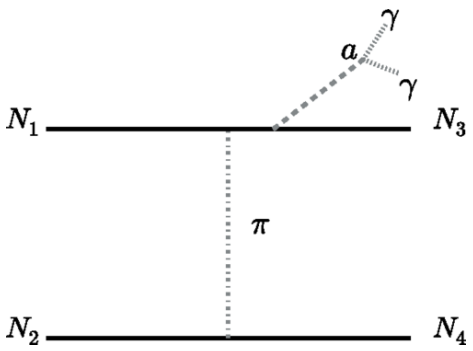

Figure 4.3.6: Diagram of the nucleon-nucleon Bremsstrahlung process. Adapted from Ref. [238].

Supernovae

The numbers, energies and distributions of neutrino events coming from supernova SN1987A were recorded by different detectors. A very dense proto-neutron star is expected to be born in the core collapse supernova, in which neutrinos are trapped, leading to a long burst duration [239]. If other weakly interacting particles, such as axions, are emitted then it would constitute a more efficient energy loss mechanism, resulting in a shorter neutrino burst duration. The SN1987A events agree with theoretical predictions, the duration of the neutrino burst was used to derive axions constraints [230], labeled as "SN1987A" in Fig. 4.3.1.

ALPs, produced via the Primakoff process between photons and the electromagnetic fields of charged particles, escape from the supernova and can eventually convert into γ-ray photons in the galactic magnetic field (GMF) [240]. No γ-ray signal was observed in coincidence with the neutrino signal from SN1987A, resulting in the bounds labeled as "SN γ-BURST" in Fig. 4.3.1. The expected sensitivity for ALPs produced in a galactic core-collapse supernova with the *Fermi*-LAT was computed in Ref. [241]. In case of non-detection, the limits would improve as seen in Fig. 4.3.1, labeled as "SN@GC". However, in a recent paper (see Ref. [242]), the authors find that these calculations are oversimplified and that these limits should be revised.

Spectral signatures from blazars

The photon-ALPs conversion probability, studied in depth in Section 4.2, exhibits two different behaviors around the critical energy of the photon-ALP mixing, E_c. Above the critical energy, the photon-ALP conversion probability becomes maximal, causing a hardening of the observed spectra of γ-ray sources (see, e.g. Refs. [243, 244, 245]). Below this critical energy, the mixing can also induce spectral irregularities that could be enhanced by certain magnetic field morphologies [207].

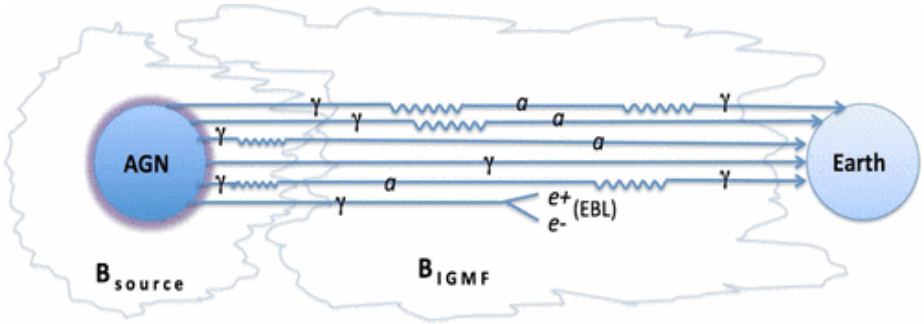

Figure 4.3.7: Graphical illustration of the propagation of photons emitted by an AGN. Within the SM, photons only interact with the EBL, producing pairs. If ALPs exist, photons could also mix with them, evading the EBL absorption and producing a hardening in the spectra of gamma-ray sources. Adapted from [246].

Sources in galaxy clusters are particularly interesting for ALP searches due to the strong magnetic fields extending all over the cluster. A set of upper limits was derived with the lack of spectral irregularities in the spectrum of the blazar PKS 2155-304 with H.E.S.S.

data [247]. More bounds come from the non-observation of irregularities from the radio galaxy NGC 1275 within the Perseus cluster by the *Fermi*-LAT collaboration [207].

As discussed in Section 3.1.2, HE photons undergo pair production absorption with the EBL photons, leading to a flux attenuation of γ-ray sources. A schematic representation of the possible interactions of a γ-ray photon in the IGM is depicted in Fig. 4.3.7. Without ALPs, the survival probability of a photon depends only on the EBL intensity. If ALPs exist, photons can turn into ALPs and evade the EBL absorption, increasing the photon survival probability and making the Universe more transparent in the γ-ray energy range. The works published in Refs. [248, 249, 250] show evidence for a more transparent Universe that could be attributed to ALPs mixing but the topic is still under discussion. We will further explore these effects in Chapter 5.

Chapter 5

COMBINED HIGHEST-ENERGY PHOTONS ANALYSIS

As a consequence of extragalactic background light interactions, the transparency of the Universe to γ rays decreases with the energy and the distance of the source of photons. Oscillations of these γ-ray photons into ALPs can take place in the large-scale magnetic fields of the different astrophysical environments where the traveling photon passes through. For energies above the critical energy, given by Eq. 4.2.17, the photon-ALP conversion takes place in the strong mixing regime and thus, more photons can survive the EBL annihilation. If ALPs convert back to photons in the vicinity of Earth, the transparency of the Universe to γ rays increases.

In this chapter, a search for axion-like particles through their effects on the transparency of the Universe with γ-ray telescopes is carried out. For this purpose, we combine the HEP events observed by the *Fermi*-LAT from different sources in a likelihood analysis. These events should change if the propagation model is different from conventional EBL models, reaching higher energies if ALPs increase the transparency of the Universe.

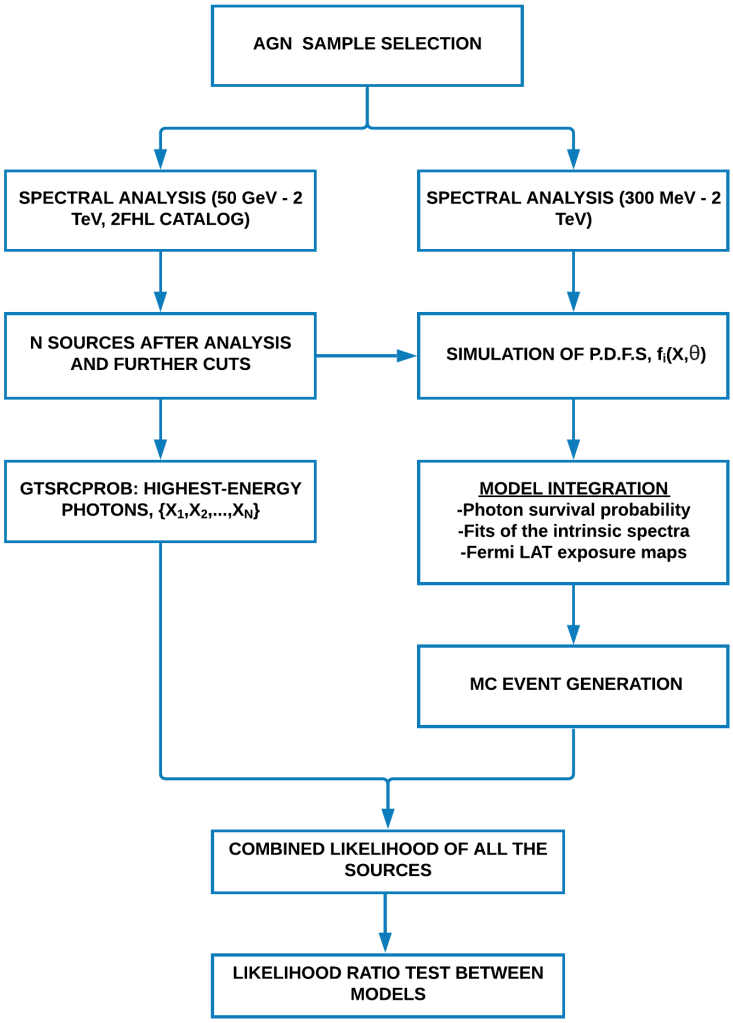

Figure 5.0.1: Flow chart of the analysis procedure. After source selection, results are taken from two independent analyses, one for the HEP and other for the intrinsic spectra. Observations are combined with the simulated p.d.f.s in order to perform a likelihood analysis in the end.

The flow chart displayed in Fig. 5.0.1 summarizes the work presented in this chapter. First, we choose a set of sources detected by the *Fermi*-LAT suitable for ALPs studies, namely, hard sources with observed photons above the critical energy of the mixing. The sources were already analyzed by the *Fermi*-LAT collaboration in the 2FHL catalog,

briefly discussed in 5.1.

From each source of the catalog, we require two measured quantities: the HEP energy and the observed spectrum. The former is already provided in the 2FHL catalog (left side of Fig. 5.0.1), whereas the latter involves an independent analysis and model dependent calculations (right side of Fig. 5.0.1) due to EBL and ALPs. The expected events from the source depend upon the propagation model and the intrinsic spectrum of the source, discussed in Sections 5.2 and 5.1, respectively.

The intrinsic spectra of the 2FHL sources are found by fitting the energy spectra from an independent analysis performed in Ref. [251], covering a lower minimum energy in which the EBL effects are negligible. These spectra are extrapolated into the absorbed region. This is possible as the high-energy spectra of AGN are smooth, as shown in Refs. [145, 252]. The propagation model describes the physics of photons traveling from the source to Earth and results in a photon survival probability that depends on the EBL model and the ALPs parameters. With the intrinsic spectrum of a source and a propagation model, we can simulate its probability p.d.f., from which the HEP event is a random variable.

Once we obtain the observed HEPs and their corresponding simulated p.d.f.s, we compute the combined likelihood for all the sources, which are independent. Further cuts based on redshift and event probabilities are applied before the analysis. Finally, we perform a likelihood ratio test between propagation models, namely, EBL and EBL with ALPs mixing in the IGM, in Section 5.4. For a value of the IGMF strength $B \leq 1$ nG we find no evidence for ALPs and exclude couplings above $1 \cdot 10^{-11}$ GeV^{-1} for ALP masses $m_a \lesssim 3$ neV. These limits are compatible with constraints imposed by other experiments and within the expected sensitivities of future experiments.

5.1 AGN SAMPLE

5.1.1 Highest-energy photons from the 2FHL catalog

The critical energy of Eq. 4.2.17 allows us to obtain the part of the ALPs parameter space that can be probed by γ-ray telescopes. Taking into account mixing in the IGM for $B = 1$ nG, $s = 1$ Mpc, $m_a \simeq 1$ neV and $g_{a\gamma} \simeq 7{\cdot}10^{-11}$ GeV^{-1}, typical critical energies lie between ~ 100 GeV and ~ 1 TeV. The *Fermi*-LAT usually measures photons between 20 MeV and 300 GeV, with the first *Fermi*-LAT catalog of hard sources (1FHL) [253]

being the first catalog of γ-ray sources from 10 GeV up to 500 GeV. The development of the Pass 8 [166] event-level analysis by the *Fermi*-LAT collaboration improved the instrument's sensitivity and its effective energy range up to 2 TeV, making it viable to observe the sky in the sub-TeV region.

The energy range of the LAT covers part of the ALPs parameter space in terms of critical energy, allowing us to search for ALPs effects. We use the sources from the Second Catalog of Hard *Fermi*-LAT sources (2FHL) [17], which reports the properties of 360 γ-ray objects significantly detected by the LAT from August 2008 to April 2015 in the 50 GeV–2 TeV range. More than 80% of the sources registered in the catalog are extragalactic and more than 75% are AGN.

In the analysis carried out in Ref. [17], data were filtered by cutting out time periods when the instrument was not in sky-survey mode and by excluding photons detected at zenith angles larger than 105°. The zenith angle cut was done in order to avoid the contamination from the γ-rays background generated by cosmic-ray interactions in the planet's atmosphere. In order to detect sources, the sky was divided in 154 ROIs with radii between $10° - 20°$, optimized to contain no more than 45 potential sources. A model that includes all candidates and the latest galactic and isotropic diffuse backgrounds was built for each ROI. This model was fit to the observed data with an unbinned maximum likelihood analysis, performed with the *Fermi* ScienceTools.[1] Finally, as in the 1FHL catalog, the spectra of individual sources were assumed to be power laws.

The catalog also offers the probabilities of each photon event belonging to each one of the sources in the ROI.[2] The probability that a specific photon event, measured with energy E' and direction $\hat{v}'$, can come from source i in the ROI depends on the model density,

$$M_i(E', \hat{v}', t) = \int dE d\hat{v}\ S_i(E, \hat{v})\ A_{eff}(E, \hat{v})\ P(\hat{v}', \hat{v}, E, t)\ D(E', E, \hat{v}, t), \tag{5.1.1}$$

where S_i is the spectral density of source i, and the rest of quantities are the effective area, point-spread function and energy dispersion, described in Section 3.2.2.3. The probability is then given by,

$$p_i = \frac{M_i}{\sum_j M_j}. \tag{5.1.2}$$

[1] The *Fermi* ScienceTools are publicly available at `https://fermi.gsfc.nasa.gov/`.

[2] Gtscrprob computes events probabilities, it is a part of the *Fermi* ScienceTools.

Among all events with a probability $P \geq 0.85$ assigned to source i, we take the one with maximum energy as the HEP. For the combined likelihood analysis, we will introduce different quality cuts with probabilities until $P \geq 0.99$. This cut improves the background rejection but it also entails a reduction in statistics.[3] Furthermore, out of these available sources, we only use sources with redshifts $z \geq 0.1$, since the effects of the mixing in the IGM increase with distance. For smaller values of redshift the effects of ALPs above the critical energy are too small to be detected by the *Fermi*-LAT.

The list of sources used in this analysis can be found in the Appendix A, and their sky positions are displayed in Fig. 5.1.1.

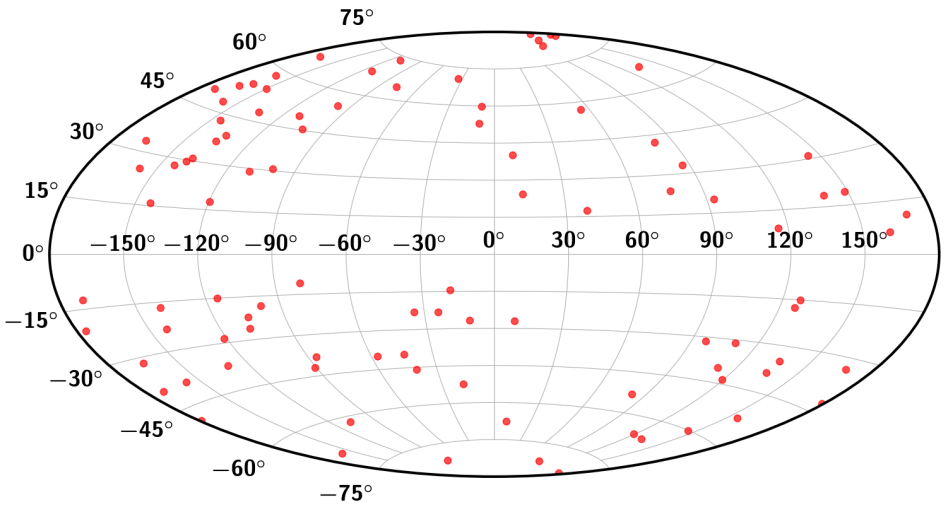

Figure 5.1.1: 2FHL catalog source positions projected over a sky map in galactic coordinates, for sources with redshifts above 0.1. Most of the sources lie outside the galactic plane. Data were taken from Ref. [17].

[3]The effects of this cut will be discussed further in Section 5.5.

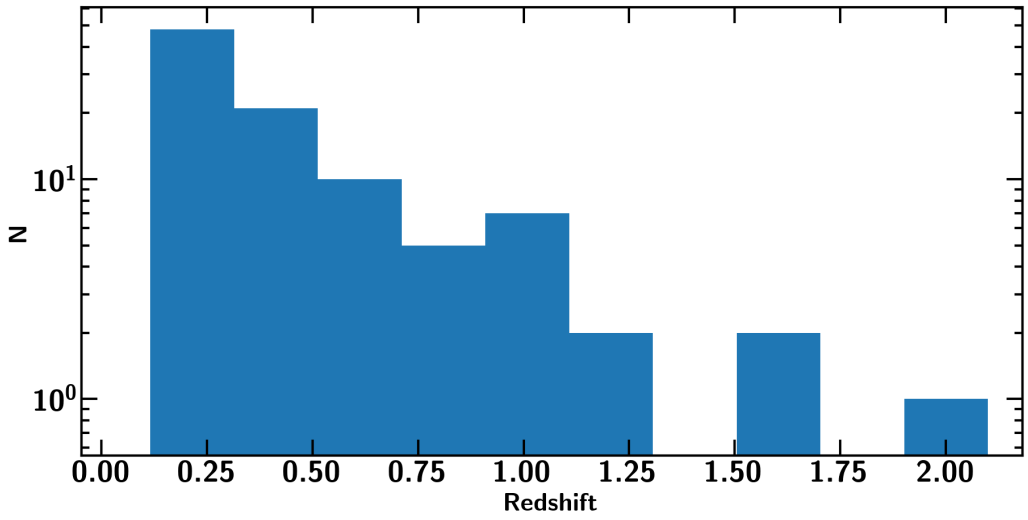

Figure 5.1.2: Sources distribution according to redshift. Data were taken from Ref. [17].

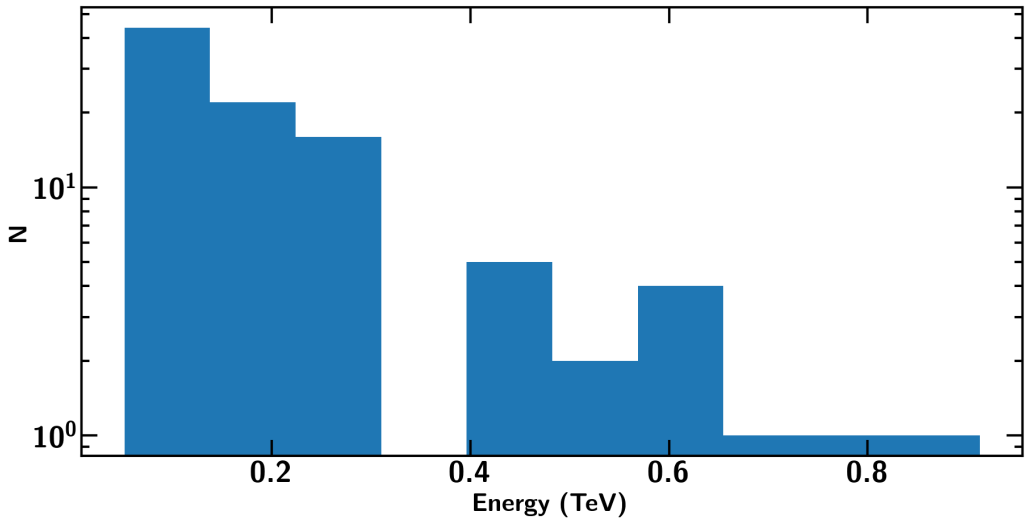

Figure 5.1.3: Source distribution according to the energy of the HEP. Data were taken from Ref. [17].

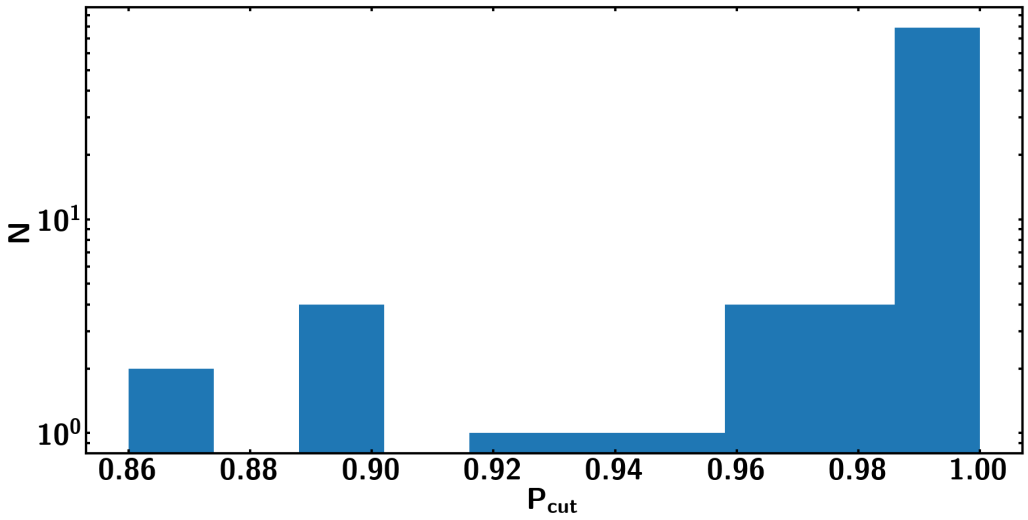

Figure 5.1.4: Source distribution according the probability of the HEP. Data were taken from Ref. [17].

The source distributions as a function of redshift and HEP energy are given in Figs. 5.1.2 and 5.1.3, respectively. The number of events increases for smaller values of energy and distance, which is expected based on the optical depth shape. In Fig. 5.1.4, the distribution of sources according to their HEP probability is shown. For all the sources, the probabilities are higher than 85%, with a peak around 99%. This is due to the low background of the LAT at high energies. All the sources we use are blazars, with roughly $\sim 90\%$ of them BL Lacs and the rest FSRQs.

5.1.2 Intrinsic spectra of the 2FHL sources

In order to make predictions for a source, we need an intrinsic spectral model. We extrapolate the spectra measured in the unabsorbed region to higher energies. This is possible as the high-energy spectra of AGN are smooth, as was shown in Refs. [145, 252]. In Section 2.4.3, we saw that the SEDs of blazars, from non-thermal emission mechanisms in the jets, present two characteristic peaks at different energy ranges. The low-energy bump is often explained with synchrotron radiation of relativistic electrons, whereas the HE part admits both types of production mechanisms, leptonic and hadronic. In the former, radiation is emitted by IC scattering of low-energy seed photons with the electron population in the blazar jet. In this case, the γ-ray spectral shape depends

upon the distribution of relativistic electrons, which is derived from the acceleration mechanisms discussed in Section 2.2, usually taken as power laws.

However, IC scattering also depends on the energies of the seed photons. For optical to ultraviolet photons (e.g. from the BLR), the scattering takes place in the Klein-Nishina regime. For photons with larger energies, coming from the same electrons in the jet or emitted by the torus, the scattering usually occurs in the Thomson regime. Changes in the underlying electron population or the regime in which the scattering happens cause the γ-ray part of the SEDs to deviate from a power law.

In this dissertation, we use the results derived in Ref. [251], in which nine years of *Fermi*-LAT data from the 2FHL blazars with known redshift were re-analyzed from 300 MeV up to 2 TeV. The reason for making use of an independent analysis is that the spectral information provided in the 2FHL catalog was derived by de-absorbing EBL models from 50 GeV to 2 TeV, energy range with non-negligible EBL features.

The data were treated with Pass 8 event-level analysis[4] and its corresponding instrument response functions. Data were filtered by removing time periods when the instrument was not in sky-survey mode and by excluding photons detected at zenith angles larger than 90°. The latter was done in order to reduce background from the Earth's limb. In contrast to the original analysis carried out in the 2FHL catalog, each ROI was centered at the source location and "SOURCE" class events were selected within a 15 degrees radius. For the spectral and spatial models, all the sources from the 3FGL catalog with a detection significance above 2σ were used, as well as the latest isotropic and Galactic backgrounds. The spectral points were calculated through a binned likelihood analysis and points below 1.5 σ significance were taken as upper limits.

We fit the spectral points from 1 GeV to the energy bin in which $\tau(E) \sim 0.1$ using a χ^2 minimization method. One spectral point more is taken below 1 GeV for distant sources. This value of $\tau(E)$ is chosen because EBL effects are not relevant at those energies and the intrinsic curvature of blazars might already take place. Lower values of τ yield spectra not compatible with the data given in the 2FHL catalog. It has been shown that the spectra of blazars is smooth and can be fit to power laws and logarithmic parabolas over sufficiently small energy ranges [145, 252], hence we use these spectral shapes. Power laws are given by,

[4]The *Fermi* ScienceTools version v10r0p5 was used.

$$\frac{dN}{dE}(E) = K\left(\frac{E}{E_0}\right)^{-\Gamma}, \tag{5.1.3}$$

where Γ is the spectral index, K is the flux normalization factor and E_0 is the pivot energy. Log parabolas are given by,

$$\frac{dN}{dE}(E) = K\left(\frac{E}{E_0}\right)^{-\alpha-\beta\log(E/E_0)}, \tag{5.1.4}$$

where α and β are the spectral indices, and E_0 is the energy scale. Examples of blazar spectra for each functional form can be seen in Figs. 5.1.5 and 5.1.6, and summary tables with all the fits quality parameters are provided in Appendix B.

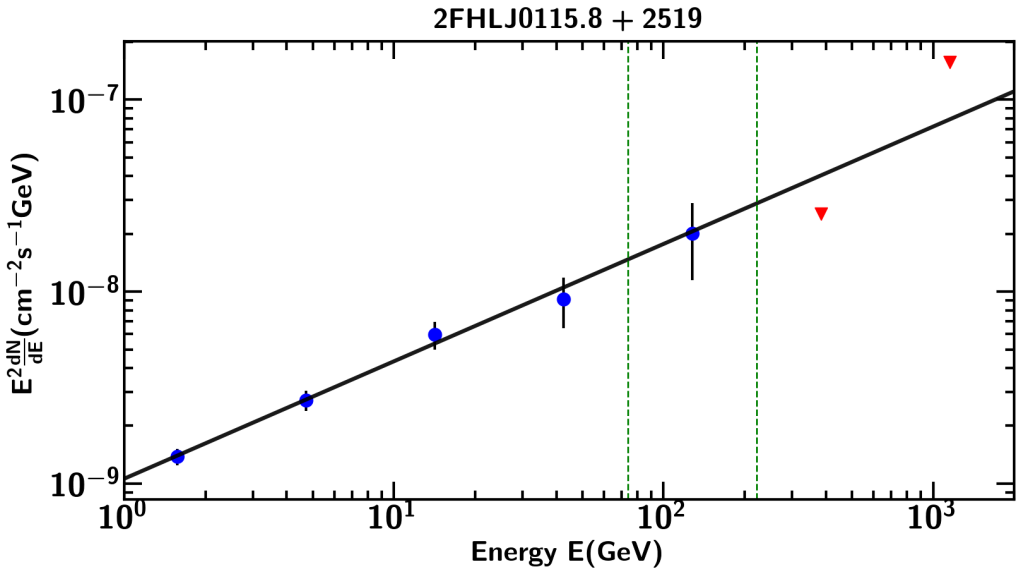

Figure 5.1.5: Example of power law fit for one of the sample sources. The blue points are the data and the red arrows are upper limits. The green dashed lines represent the energy bin for which the optical depth parameter is around 0.1. Data were taken from Ref. [251].

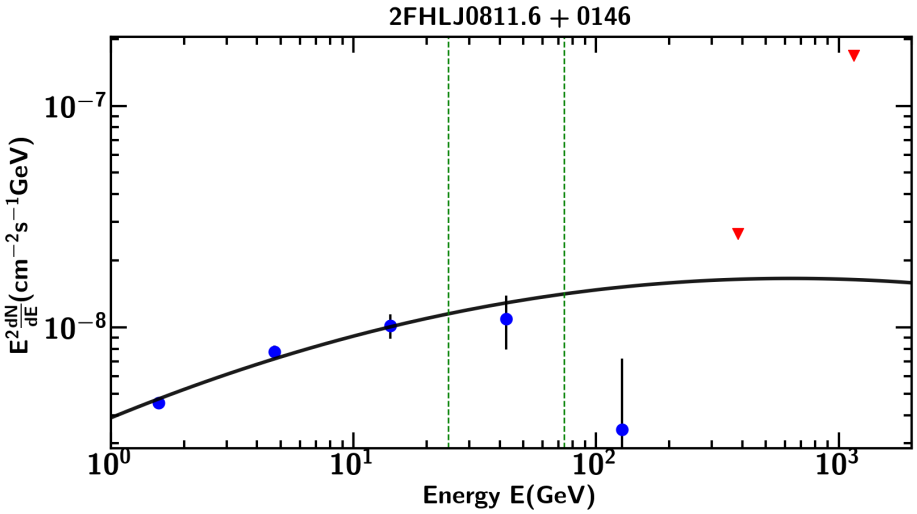

Figure 5.1.6: Example of log parabola fit for one of the sample sources. The blue points are the data and the red arrows are upper limits. The green dashed lines represent the energy bin for which the optical depth parameter is around 0.1. Data were taken from Ref. [251].

5.2 GAMMA-RAY TRANSPARENCY OF THE UNIVERSE

5.2.1 Conventional propagation of photons

The survival probability (or attenuation factor) of γ rays due to the EBL is described by a decreasing exponential of the optical depth parameter, $\tau_{\gamma\gamma}(E, z)$. This model dependent parameter is an increasing function of the photon energy and the distance to the source. The observed γ-ray spectra of sources are then described by,

$$\phi_{obs}(E, z) = \phi_{int}(E) \cdot \exp\left(-\tau(E, z)\right), \tag{5.2.1}$$

where ϕ_{obs} and ϕ_{int} are the observed and intrinsic spectra, respectively. The intrinsic spectral shapes and fits were discussed in the previous section.

Throughout this work we use the observationally-based Dominguez et al. model [150]. The overall spectrum of the EBL is derived directly from galaxy SED observations over a

wide redshift range. Data from the All-wavelength Extended Groth Strip International Survey (AEGIS) [254] of ∼6000 galaxies with redshifts between 0.2 and 1 are combined with the observed evolution of the rest-frame K-band galaxy luminosity function up to redshift 4 [255]. We decided to use the Dominguez et al. model due to its observational method and wide range of redshifts covered, but there is no particular reason to choose any EBL model over others derived under different approaches, since their predictions are compatible with the current constraints. The effects of choosing a different EBL model in our analysis will be discussed in Section 5.5.

Fig. 5.2.1 shows the optical depth parameter for different values of redshift computed with the Dominguez et al. model. Correspondingly, Fig. 5.2.2 displays the photon survival probabilities computed with the optical depths for each case. We can see that the survival probability of a γ-ray photon of energy E propagating through the IGM decreases with energy and traveled distance.

The bumps in the EBL intensity from Fig. 3.1.2 are reflected in the optical depth parameter. The initial rise until optical wavelengths results in a rapid growth of $\tau_{\gamma\gamma}$ until ∼500 GeV. Between 1 and 10 TeV, the slope of $\tau_{\gamma\gamma}$ becomes smaller due to a decrease in the EBL intensity. This energy dependence causes spectral breaks on γ-ray sources [125].

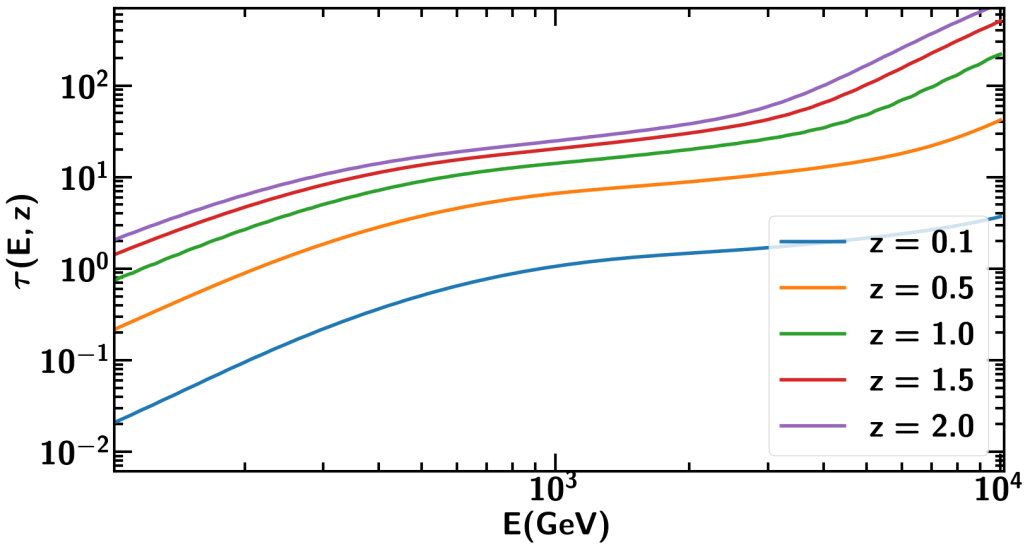

Figure 5.2.1: Photon survival probabilities for the Dominguez et al. EBL model at different redshifts. Data were taken from Ref. [150].

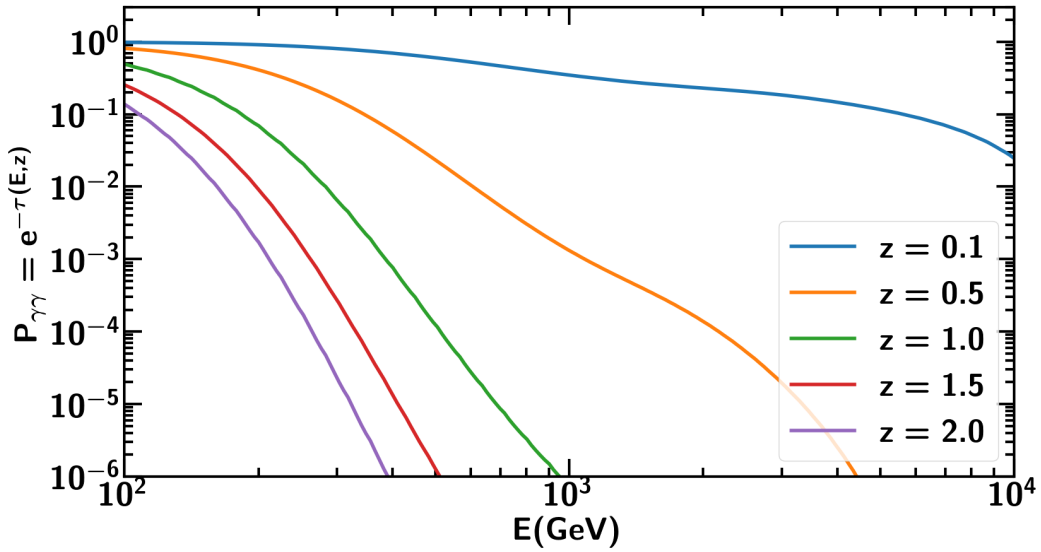

Figure 5.2.2: Photon survival probabilities for the Dominguez et al. EBL model at different redshifts. Data were taken from Ref. [150].

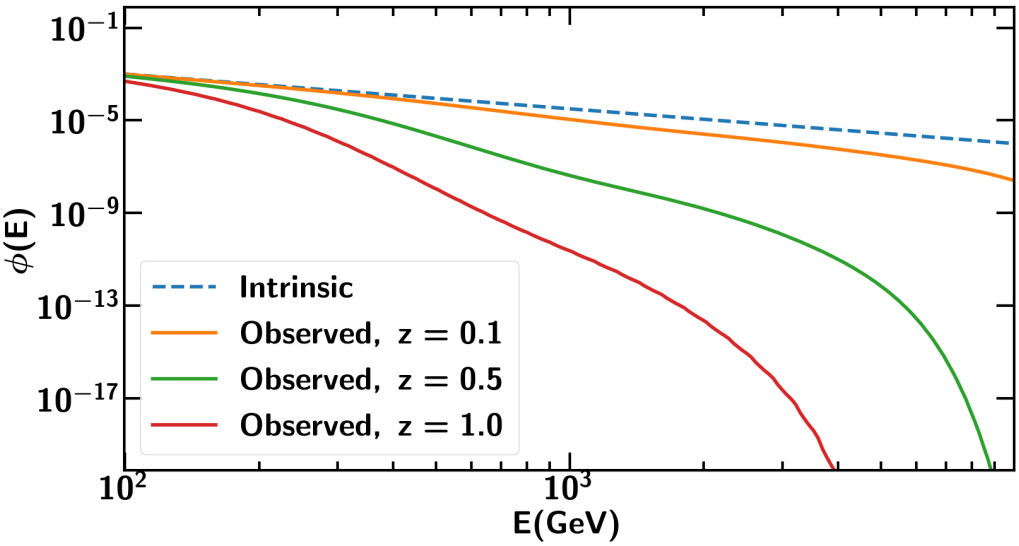

Figure 5.2.3: Dashed line: power law intrinsic spectrum of a blazar. Solid lines: observed spectrum for different redshifts, after EBL attenuation. Computed with the Dominguez et al. model. The flux normalization is taken as unity, the pivot energy is 1 GeV and the spectral index is 1.5.

An example of intrinsic spectrum of a blazar and EBL absorption is given in Fig. 5.2.3 computed with Eq. 5.2.1 and with the power law shape of Eq. 5.1.3. The figure displays the spectral attenuation that increases with energy and distance to the source. The observed spectra cannot be described by a power law over the entire energy range but can be fit to two different power laws in two different energy ranges that depend on the redshift.

Gamma ray telescopes observe mostly the attenuated emission. As we discussed in the previous Section, in order to obtain the intrinsic spectrum of a source, a fit can be done in the region in which EBL effects are negligible. A intrinsic spectral index Γ_{GeV} is obtained from this fit. Assuming that the intrinsic spectral shape of the source does not change for higher energies, an spectral break is expected to happen. The observed spectral index in the TeV range Γ_{TeV} increases due to the EBL absorption. The presence of this spectral break has been confirmed [125] and can be used for studying the EBL with blazar observations.

The cosmic γ-ray horizon (CGRH) is the curve, given by the values of E_0 and z, at which the optical depth parameter becomes unity, $\tau(E_0, z) = 1$. The solid black line displayed in Fig. 5.2.4 is the CGRH derived with the Dominguez et al. model. Above this curve, the survival probability of HE and VHE photons decreases exponentially as the optical depth parameter increases, therefore the Universe becomes less transparent to γ rays. In the region below the CGRH, the survival probabilities are larger and the Universe is more transparent to γ rays. It is less probable that photon events of energy E_0, that come from a source located at z, survive the EBL absorption for large values of τ and appear in the plot, hence the density of events is larger below the horizon. For a given redshift, the CGRH quantifies the maximum energy of photons that survive the EBL.

If there were modifications of the expected γ-ray propagation, the observed HEP event for each source, shown in Fig. 5.2.4, should change correspondingly, allowing us to search for ALPs with these events. Since the EBL intensity determination is still an open problem, we also expect transparency discrepancies between EBL models. In Section 5.4, we also test how a different EBL model affects our results.

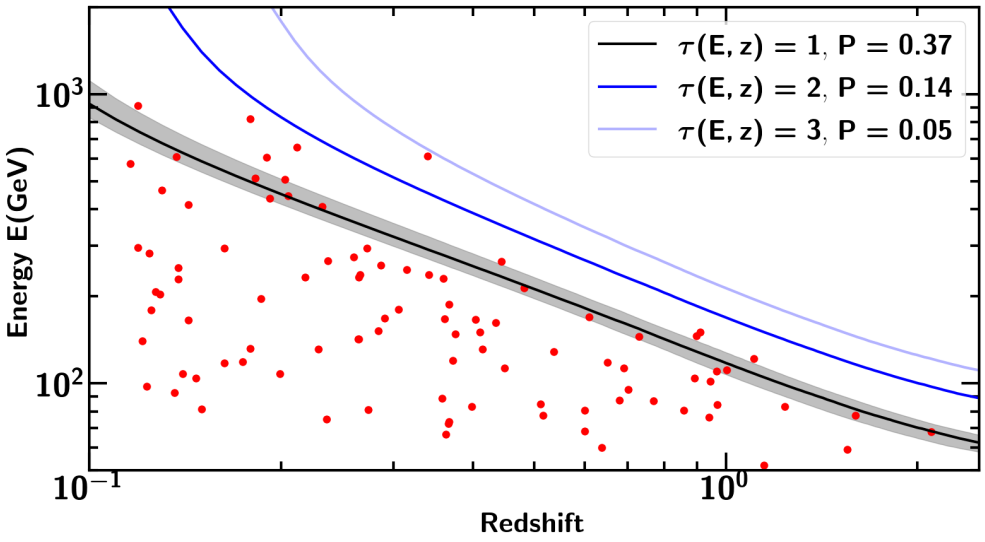

Figure 5.2.4: HEP energy vs redshift. Red points represent the observed energy of the 2FHL catalog sources HEP with the *Fermi*-LAT. The solid black line is the CGRH computed with the Dominguez et al. EBL model, with its uncertainties as a shaded grey band. Solid lines represent other constant survival probabilities, P. Data were taken from [17].

5.2.2 Conversion in the intergalactic medium

The detection of cosmic magnetic fields, for which evidence suggests their presence at all scales in the Universe [256], is a challenging and active research topic in astrophysics. We can indirectly observe the effects of these fields on the acceleration of cosmic rays and on the propagation of radiation. For a review on the topic of magnetic fields detection see e.g. Ref. [257]. Synchrotron radiation, Faraday rotation and Zeeman splitting are the three observational quantities used to study the morphologies cosmic magnetic fields.

Synchrotron emission of relativistic electrons allows us to estimate the strength of the fields, while the polarization degree of the emission provides information about the homogeneity and overall structure of the fields [257]. The polarization angle change induced by Faraday rotation in linearly polarized photons is given by,

$$\phi = (\mathrm{RM})\lambda^2 + \phi_0, \tag{5.2.2}$$

where RM is a quantity that depends on the electron density and magnetic components along the line of sight, λ is the wavelength of the radiation and ϕ_0 is the initial polarization angle [258]. Regarding galactic observations, the spectral lines of the emission split through the Zeeman effect in the presence of magnetic fields, but observations are difficult [259]. Additionally, polarization observations of optical starlight due to magnetic dust grains provides complementary information for GMFs [260]. The magnetic fields of some stars [261], galaxies [262], and the Milky Way [263] have been detected using these methods. Upper limits exist for other environments, such as the IGMF [264].

The origin of cosmic magnetic fields, or magnetogenesis problem, is still open to research. For reviews on the topic see, e.g., Refs. [14, 257]. The problem can be divided into two parts: the creation of weak magnetic fields at some point in the history of the Universe and how those fields were amplified to the currently observed values of 10^{-6} G in galaxies. Fields of the order of 10^{-20} G can be generated during galaxy formation due to the Biermann battery mechanism [265], in which magnetic fields are produced in ionized plasmas when there are non-parallel gradients in temperature and density. Alternative seed generation scenarios include exotic processes in the early Universe [257, 266]. Amplification mechanisms include, for instance, the $\alpha - \Omega$ dynamo model discussed in Ref. [14].

As discussed in Section 4.3, the photon-ALPs mixing can take place in any astrophysical environment with strong electric or magnetic fields, summarized as follows:

- Mixing in the source: the interior of stars, supernovae, GRBs, AGN etc. Conversion can occur in the strong electric fields generated by charged particles within these objects or in the surrounding magnetic field regions.

- Mixing in galaxy clusters: the medium between stars and galaxies within a cluster. The mixing in this environment leads to spectral irregularities below the critical energy. Typical values for field strength in these environments are $B \simeq 10^{-6}$ G [207].

- Mixing in the Milky Way: there are models for the GMF, based on observations. The mixing in this region is important for ALPs masses above 1 neV. Typical values for the field strength are $B \simeq 10^{-6}$ G [267].

- Mixing in the intergalactic medium: the IGM is the space between stars and galaxies. It is pervaded with background radiation at different wavelengths and

diffuse matter [268]. Mixing in this region is important for ALP searches where the effects of EBL are non-negligible. Current upper limits are $B \leq 1$ nG over Mpc scales.

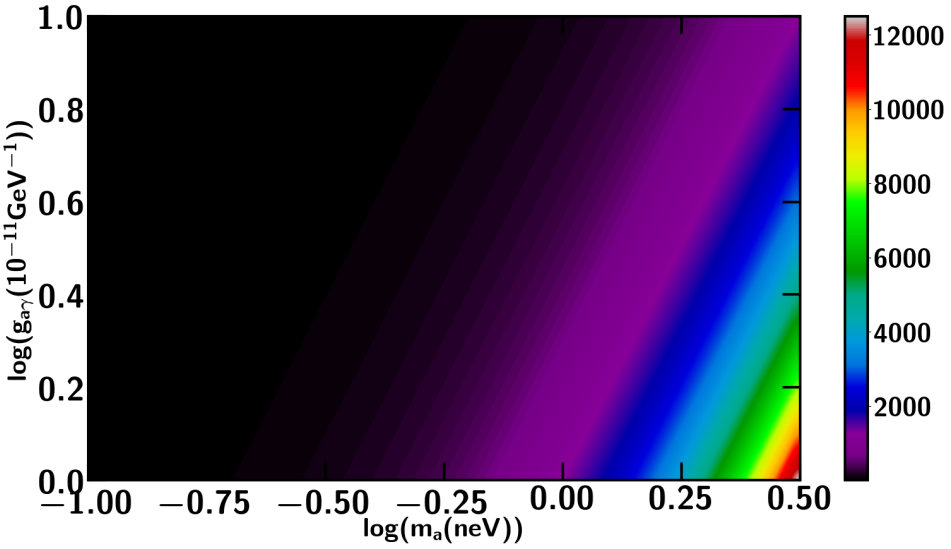

Figure 5.2.5: Critical energy in units of GeV (colorbar) projected over the ALPs mass-coupling parameter space. For magnetic field strength of 1 nG.

We have seen the analytic solution for the photon-ALP conversion probability under the assumptions that the magnetic field strength is homogeneous and that the beam is in a pure polarization state. In this case, the conversion probability, given by Eq. 4.2.15, becomes maximal above the critical energy of the mixing. An example of this quantity, for $B = 1$ nG, can be seen in Fig. 5.2.5. The constant critical energy lines are diagonals in the ALPs parameter space and they limit regions accesible to γ-ray telescopes for this particular magnetic field strength and morphology.

For the rest of the section, we will take into account only the mixing in the intergalactic field and use Eq. 4.2.25, derived for domain-like structures and unpolarized beams. Mixing in other magnetic environments will be discussed in the next Section. The IGMF is often modeled as a domain-like structure in redshift, with upper limits on B_0 depending on the coherence length of the field, s.

Fig. 5.2.6 shows upper and lower limits on the IGMF. The elipses and grey regions are known observational bounds from Ref. [264] (Zeeman splitting measurement, magnetic

diffusion, the Hubble radius, Faraday rotation measures [269, 270], cosmological observations of the CMB [271, 272, 273, 274], and galaxies and clusters). On the other hand, the propagation of ultra-high-energy extragalactic cosmic rays is affected by the IGMF, opening up a complementary method to probe these large-scale fields, shown in the plot as the hatched black regions [275, 276]. Using this technique, a recent work ruled out low values of B with γ-ray observations [277]. The lower-limits can be seen at the bottom part of the figure. The VERITAS collaboration also excluded values of B between $5.62 \cdot 10^{-15}$ G and $3.16 \cdot 10^{-14}$ G, using observations of the blazar 1ES1218+304 [278]. Orange hatched regions display the allowed part of the parameter space for magnetic fields generated in the early Universe.

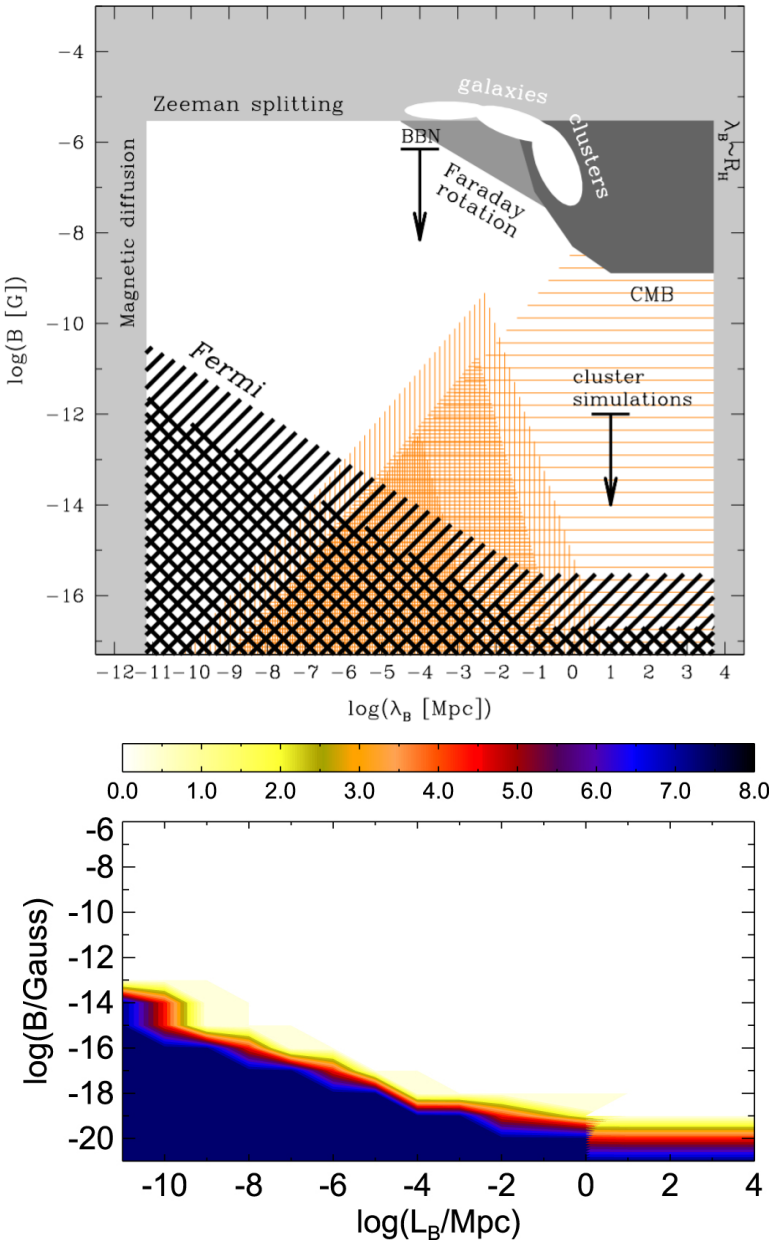

Figure 5.2.6: Top: limits on the IGMF. See text for a description. Adapted from Ref. [276]. Bottom: excluded region from BL Lac gamma-ray observations for the Finke et al. EBL model. The colors represent the significance of exclusion. Adapted from Ref. [277].

Following Eq. 4.2.25, we can evaluate the modified photon survival probability in this

scenario, but cosmological effects must be included due to the large redshifts of the sources considered. Due to the lack of observations of the Gunn-Peterson effect [279], it is hinted that the IGM is ionized, resulting in a high electrical conductivity with an electron number density that follows,

$$n_e(z) = \bar{n}_{e,0}\,[1+\delta(z)]\,(1+z)^3, \tag{5.2.3}$$

where $\bar{n}_{e,0}$ is the average density in the local Universe and $\delta(z) = (\rho(z) - \bar{\rho}(z))/\bar{\rho}(z)$ is the mass density contrast. If the IGM is highly conductive, the magnetic field lines are frozen inside the medium. During the expansion of the Universe, flux conversation requires that B scales as,

$$B = B_0(1+z)^2, \tag{5.2.4}$$

where B_0 is the magnetic field strength in the local Universe. Finally, the energy correction is given by,

$$E = E_0(1+z). \tag{5.2.5}$$

We divide the IGM in domains equally spaced in redshift, along the line of sight of each source. The number of domains crossed by the beam is $N_d = z/\Delta z$, where Δz is the domain length. For the n-th domain, evolutionary cosmological effects can be neglected within individual domains and just taken into account for the jump between different domains. Next, we compute the mixing matrix terms of Eq. 4.2.8 with all the redshift corrections per domain. The absorption Δ-term cannot be neglected in the IGM, as a consequence of the EBL interactions with γ-ray photons. However, ignoring cosmological effects inside the domain, the optical depth can be expressed as,

$$\tau_{\gamma\gamma}(E, D) = \frac{L}{\lambda_\gamma(E)}, \tag{5.2.6}$$

where L is the proper source distance and $\lambda_\gamma(E)$ is the photon mean free path. The first term of Eq. 3.1.4 can be used to convert the domain length to proper units,

$$L(z_a, z_b) = \int_{z_a}^{z_b} dz \frac{dl}{dz} \simeq 4.29 \cdot 10^3 \int_{z_a}^{z_b} \frac{dz}{(1+z)\sqrt{0.7 + 0.3\,(1+z)^3}}\,\text{Mpc}. \tag{5.2.7}$$

We can now compute the photon mean free path due to the EBL interactions needed for the absorption Δ-term of the mixing matrix. The expression for the n-th cell is

given by,

$$\lambda_{\gamma}^{(n)}(E) = \frac{s^{(n)}}{\tau_{\gamma\gamma}(E_n, n\Delta z) - \tau_{\gamma\gamma}(E_n, (n-1)\Delta z)}, \tag{5.2.8}$$

where $s^{(n)}$ is the coherence length for the n-th domain evaluated with Eq. 5.2.7, and $E_n = E_0\,[1 + (n-1)\Delta z]$ is the energy in the n-th domain. The magnetic field of Eq. 5.2.4 for the n-th domain is given by

$$B_n = B_0\,[1 + (n-1)\,\Delta z]^2\,. \tag{5.2.9}$$

An example of the model for one field realization can be seen in Fig. 5.2.10. Random angles were generated in each domain for $B_0 = 1$ nG and $s = 1$ Mpc.

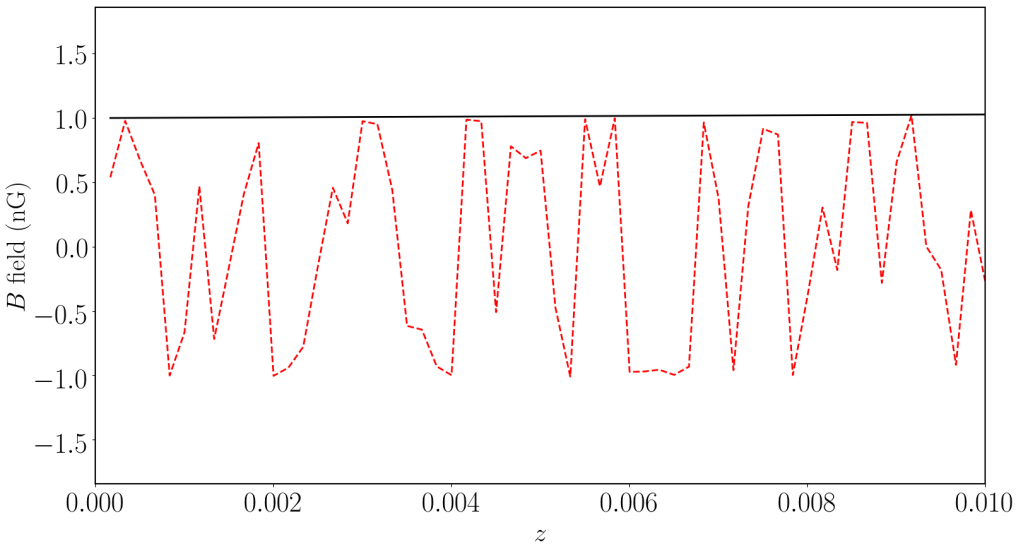

Figure 5.2.7: Solid black line: magnetic field strength as a function of redshift for the IGM, from Eq. 5.2.4. Dashed red line: transverse component (projected over the cosine) of the field for one realization. Random angles were uniformly generated in each cell from 0 to 360 degrees. Image created using gammaALPs code by M. Meyer, found in `https://github.com/me-manu/gammaALPs`.

Regardless of the magnetic field values, the photon-ALP beam propagation has also a dependency on the content of the medium. The plasma frequency of the medium,

computed with Eq. 5.2.3, gives the photon an effective mass. The electron density of the IGM is $n_{e,0} \simeq 10^{-7}\,\mathrm{cm}^{-3}$ [280], resulting in a plasma frequency $w_{pl} \simeq 1.17 \cdot 10^{-14}\,\mathrm{eV}$, value compatible with the WMAP7 upper bound on the baryon density [281]. The parameters of the model, in the local Universe, are summarized in Table 5.2.2.

The solution of the propagation problem is given by the product of transfer matrices for all the domains. For a single source, the full procedure goes as follows. First, we randomly generate the orientation angle of the transverse field with respect to the fixed z-axis for each domain, $\psi_n \in [0, 2\pi]$. This constitutes one magnetic field realization across a line of sight in the sky. Next, we evaluate the transfer matrix of each individual domain and the full transfer matrix of the system as the product of individual matrices. After this, we compute the photon survival probability and then average it over many realizations following Eq. 4.2.25.

Examples of $P_{\gamma\gamma}(E, z)$ as a function of the beam energy and for different redshifts can be seen in Figs. 5.2.8 and 5.2.8. The survival probabilities for different redshifts were computed with the Dominguez et al. EBL model and with ALPs mixing in the IGM. From these results, in this scenario, it can be seen that there is a modification of the transparency of the Universe to γ rays dependent upon the energy of the beam. Below the critical energy, the Universe becomes more opaque in comparison to conventional EBL models. Above the critical energy, the Universe gets more transparent compared to EBL models. However, the difference between models is more relevant for the TeV range. Below $z = 0.1$, the enhancement is too small in the *Fermi*-LAT energy range and only the survival probability decrease affects the spectra of γ-ray sources.

In Section 5.3, we use these results for the Monte Carlo simulations required to compare between models, for the selected sample of sources and different ALPs couplings and masses. Fig. 5.2.10 displays an example of photon attenuation applied to a power law spectrum of a blazar, which becomes harder above the critical energy.

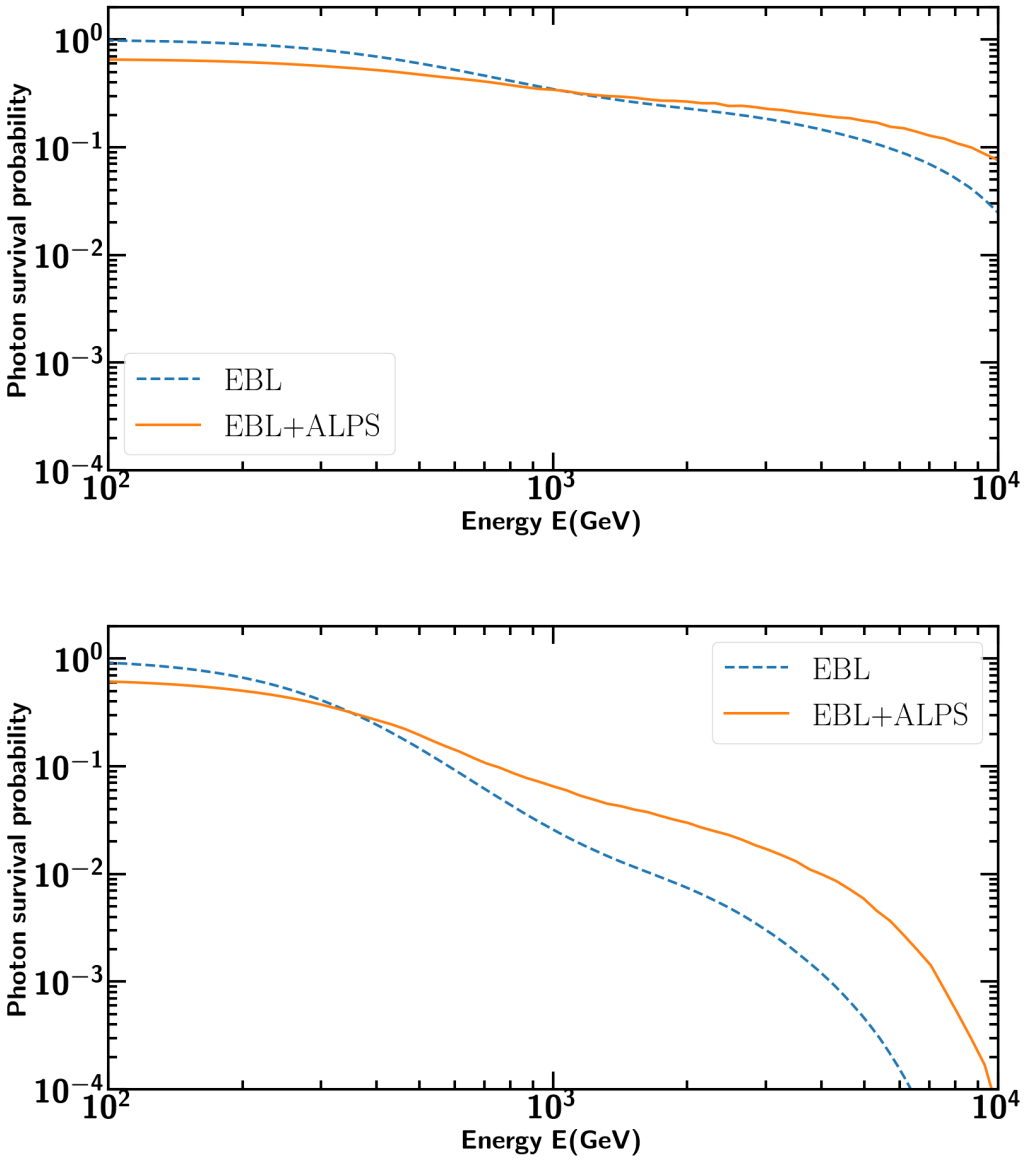

Figure 5.2.8: Survival probabilities for EBL (dashed lines) and EBL + ALPs models (solid lines). The plot on top corresponds to redshift 0.1, whereas the bottom one is 0.3. The ALPs parameters are $m = 1$ neV and $g_{11} = 7$. Image created using gammaALPs code by M. Meyer, found in `https://github.com/me-manu/gammaALPs`.

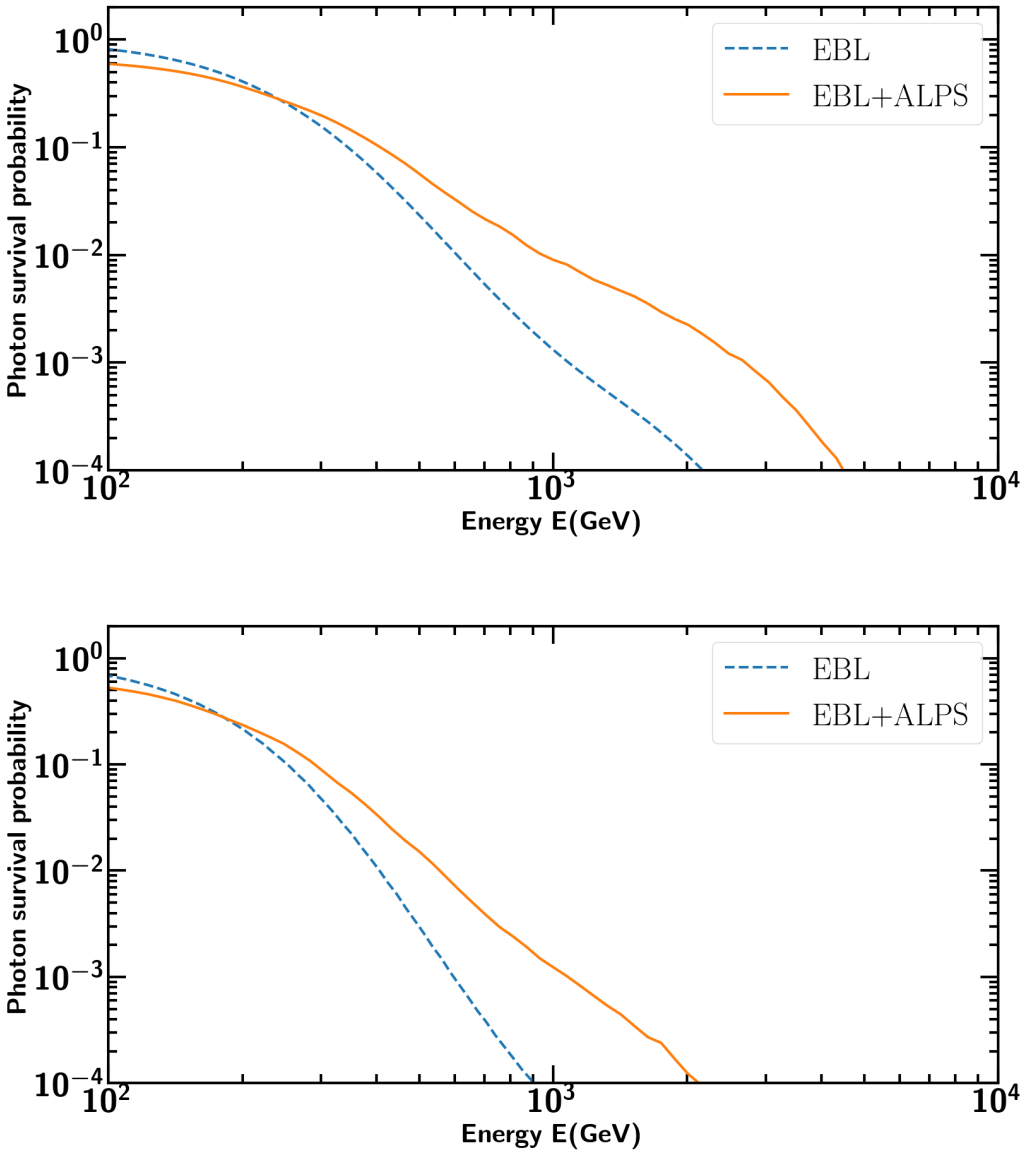

Figure 5.2.9: Survival probabilities for EBL (dashed lines) and EBL + ALPs models (solid lines). The plot on top corresponds to redshift 0.5, whereas the bottom one is 0.7. The ALPs parameters are $m = 1$ neV and $g_{11} = 7$. Image created using gammaALPs code by M. Meyer, found in `https://github.com/me-manu/gammaALPs`.

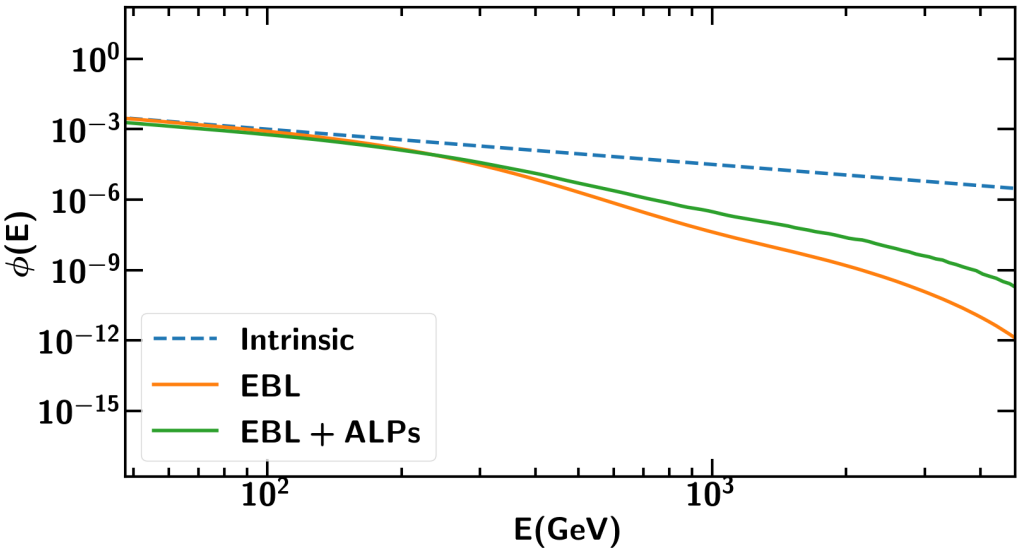

Figure 5.2.10: Spectrum of a source located at z=0.5. Dashed line: intrinsic spectrum. Orange line: absorbed by EBL. Green line: with ALPs. The ALPs parameters are $m = 1$ neV and $g_{11} = 7$. Image created using gammaALPs code by M. Meyer, found in `https://github.com/me-manu/gammaALPs`.

Parameter	Value
B_0	$0.1 - 1$ nG
s	$1 - 5$ Mpc
$n_{e,0}$	10^{-7} cm^{-3}
$\omega_{pl,0}$	$1.17 \cdot 10^{-14}$ eV

Table 5.1: Model parameters for the IGM used in this work.

5.2.3 Other possible γ-ray to ALPs conversion regions

Blazar magnetic fields

Other known conversion regions that are also relevant for the photon-ALPs mixing but not relevant for our analysis are discussed in this section. Conversion in blazars requires

two models, for BL Lacs and FSRQs. A recent work tried to observe the structure of the magnetic field in different BL Lac jets from $0.1 - 100$ pc and found that $\mathbf{B}$ is ordered, for the most part transverse to the jet and not compatible with a domain-like structure [282]. Studies of the SSC mechanism applied to SEDs of BL Lacs yield $B_{T,\ell} = 0.1 - 10\,\mathrm{G}$ and $n_{e,\ell} \simeq 5 \cdot 10^4\,\mathrm{cm}^{-3}$ [283], where ℓ stands for values inside the emission region. With these two results, the comoving transverse magnetic field and electron density profiles along the propagation y-axis are modeled as [284],

$$B_T(y) = \frac{\ell B_{T,\ell}}{y} \qquad n_e(y) = \frac{\ell^2 n_{e,\ell}}{y^2}, \tag{5.2.10}$$

for values of y above ℓ.

In contrast to BL Lac objects, the morphology of the magnetic field in FSRQs is more complicated because the BLR and the dusty torus reach distances larger than ℓ and there are magnetized lobes at the end of the jet. The parameter ℓ is taken three times larger to account for the larger variability time scales, and values of $B_{T,\ell} = 1 - 10\,\mathrm{G}$ and $n_{e,\ell} \simeq 10^4\,\mathrm{cm}^{-3}$from SSD modeling studies [285]. The geometry and strength of $\mathbf{B}$ are still unknown but Eqs. 5.2.10 can be used for simplicity. Additionally, the magnetic field in the lobes can be modeled with a domain-like structure with $B = 10^{-6}$ G and s =10 kpc.

In Ref. [284], using Eqs. 5.2.10, the authors find that the conversion in BL Lacs is non-negligible but it has a very large dependence on all the model parameters. These results were computed for ALPs masses $\sim 10^2$ neV, outside the parameter space we test in this work. In view of this, and due to the lack of field observations for all the sources in the sample, we do not consider mixing in this region.

Milky Way magnetic field

The latest GMF model, Jansson & Farrar, can be found in Ref. [267]. The authors use data from the WMAP7 galactic synchrotron emission map and extragalactic Faraday rotation measurements to find the best fit the parameters to constrain the model.

This GMF model consists of two parts, namely, a large-scale regular component and a small-scale random component. The latter will not be discussed here because the oscillation length of the ALPs mixing, Δ_{osc}, is much larger than the coherence length of the turbulences. For an arbitrary source in the sky, the transverse component of the galactic field forms an angle ψ with the z-axis of propagation coordinates.

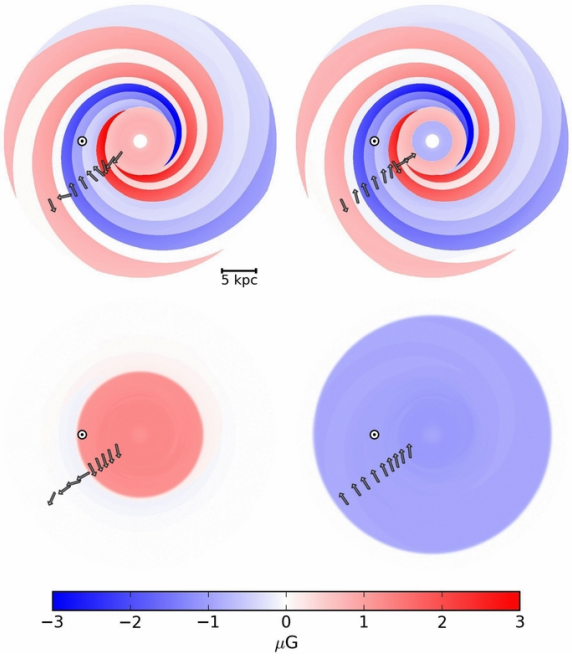

Figure 5.2.11: Slices of the magnetic field model in the $x-y$ plane of the galaxy. From left to right, the z coordinate is 10 pc, -10 pc, 1 kpc and -1 kpc. The color bar represents the magnetic field strength. The circle represents the sun, located at $x = -8.5$ kpc. Adapted from Ref. [267].

Examples of field dependence on the z-axis, in cylindrical coordinates with the Galactic center at the origin, are displayed in Fig. 5.2.11. From this, it can be seen that the photon-ALPs mixing in this environment strongly depends on the position of the source in the sky. Not only the distance traversed within the galaxy changes, but also the orientation and strength of the field varies between arms and galactic z. The survival probability can be computed with this model and Eq. 4.2.22.

The survival probability, taking into account conversion in the IGM and the Milky Way, for an arbitrary source, is shown in Fig. 5.2.12. The ALPs parameters taken for this example are $m_a = 30$ neV and $g_{a\gamma} = 7 \cdot 10^{-11}\,\mathrm{GeV}^{-1}$. In the TeV range, there is an further enhancement of the photon survival probability and a oscillatory behavior that depends on the ALPs parameters, for ALPs masses above ~ 10 neV. Below this mass, the difference between models decreases and the conversion occurs at lower energies. These values are outside the parameter space considered in this Dissertation, therefore we do not consider mixing in the GMF.

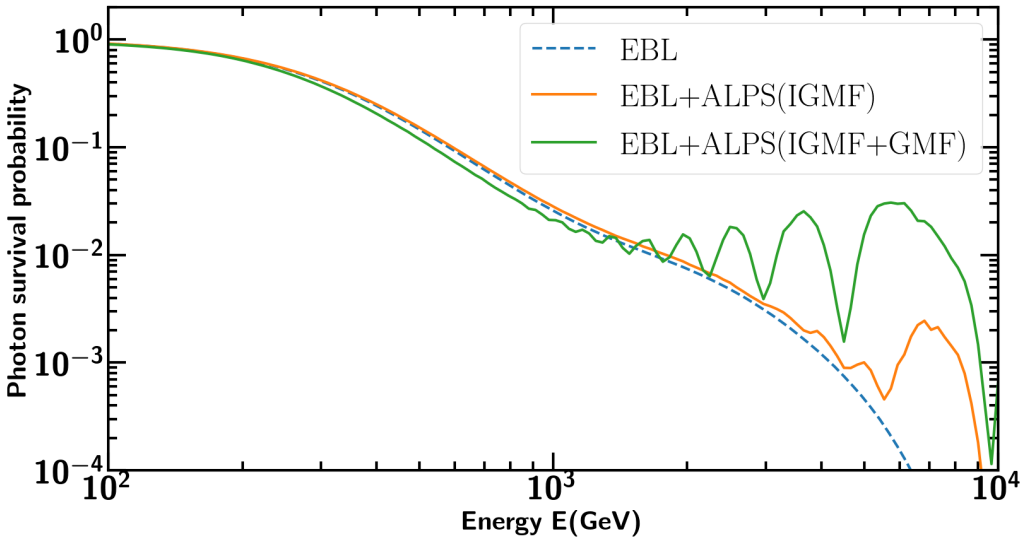

Figure 5.2.12: Photon survival probabilities for a source located at RA = 21h58m52.0s, DEC = -30d13m32s and z= 0.3. Image created using gammaALPs code by M. Meyer, found in `https://github.com/me-manu/gammaALPs`.

Intra-cluster magnetic field

Part of the AGN are embedded in galaxy clusters [286, 287]. There are hints of turbulent magnetic fields in these environments [288, 289, 290] that follow from Faraday rotation measurements, radio synchrotron emission and magneto-hydrodynamic simulations. The magnetic field strength depends on the electron density of the cluster, $n_e(r)$, and it is given by [291],

$$B(r) = B_0 \left[\frac{n_e(r)}{n_0}\right]^{\eta}, \tag{5.2.11}$$

where r is the distance to the center of the cluster, B_0 is the magnetic field strength at the center, η is a parameter between 0.5 and 1, and n_0 is the electron density at the center. The electron density is modeled as,

$$n_e(r) = n_0 \left(1 + r/r_{core}\right)^{-3\beta/2}, \tag{5.2.12}$$

where β is another parameter that takes typical values around 2/3. Values of $n_0 = 10^{-3}\,\mathrm{cm}^{-3}$, $r_{core} = 100$ kpc, $\eta = 1$, and $B_0 = 1\,\mu$G have been derived from observations of 3C 31 and 3C 449 [292, 293].

The field is modeled as a divergence-free homogeneous and isotropic Gaussian turbulent magnetic field with zero mean and σ_B variance, in a better agreement than a simple domain-like structure, according to observations [294]. Ref. [291] assumes a power-law power spectrum for the energy density as a function of the wave number k, $M(k) \propto k^q$, between the turbulence scales $k_L \leqslant k \leqslant k_H$, defined as $k_L = 2\pi/\Lambda_{max}$ and $k_H = 2\pi/\Lambda_{min}$. For a propagation direction along the x_3-axis, the transversal components $(i = 1, 2)$ of the field are,

$$B_i(x_3) = \sum_{n=1}^{N_k} \left[\frac{2\tilde{\epsilon}_\perp(k_n)\Delta k_n}{\pi} \ln\left(\frac{1}{U_{i,n}}\right) \right]^{1/2} \cos\left(k_n x_3 + 2\pi V_{i,n}\right), \tag{5.2.13}$$

where $U_{i,n}$ and $V_{i,n}$ are random numbers from a uniform distribution between $[0, 1)$, N_k is the number of spacings in k, and $\tilde{\epsilon}_\perp(k_n)$ is the correlation function on the line of sight for the transversal field components,

$$\tilde{\epsilon}_\perp(k_n) = \frac{\pi}{4}\sigma_B^2 F_q(k, k_L, k_H), \tag{5.2.14}$$

where F_q is a function given in the appendix of Ref. [291].

This model has been used in Ref. [295] in order to search for spectral irregularities in the spectrum of the NGC 1275 radio galaxy embedded in the Perseus cluster. A magnetic field realization as a function of the cluster distance can be seen in Fig. 5.2.13, where the fiducial parameter choices where taken from Ref. [295]. Two realizations of the photon survival probability for NGC 1275 is shown in Fig. 5.2.14, computed with the same parameter values, in which we can see the induced spectral irregularities below the critical energy. The part parameter space in which this effect occurs corresponds to higher masses than the ones used in this analysis. Since this magnetic configuration does not enhance the survival probability above the critical energy, we do not consider it in the mixing. Additionally, the parameter values of the field are only for the Perseus cluster and proper models for all the sources would require observations and models for all the clusters in which they are embedded.

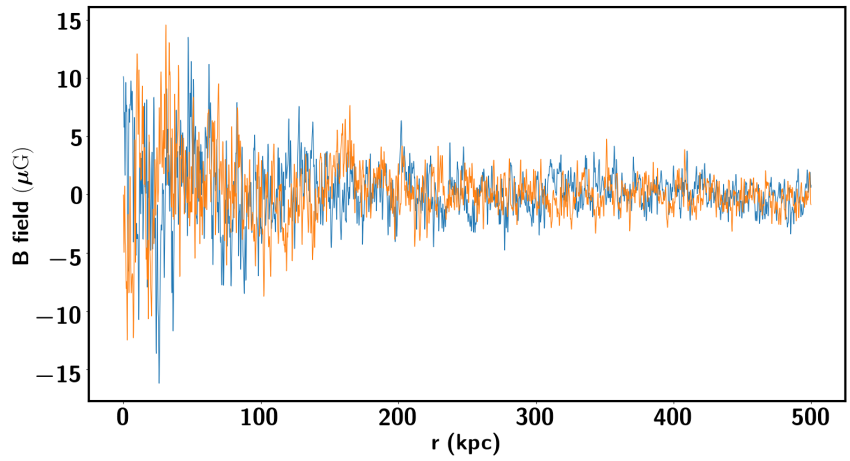

Figure 5.2.13: The two transversal components of the field, as described in Eq. 5.2.13, for the Perseus cluster. Image created using gammaALPs code by M. Meyer, found in `https://github.com/me-manu/gammaALPs`.

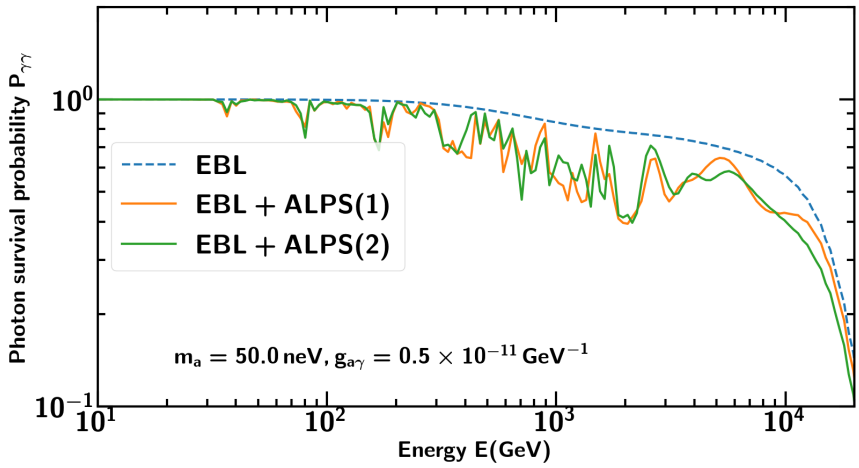

Figure 5.2.14: Survival probabilities for NGC 1275. Dashed line: EBL only. Solid lines: two different realizations of the field. Image created using gammaALPs code by M. Meyer, found in `https://github.com/me-manu/gammaALPs`.

5.3 PROBABILITY DISTRIBUTION FUNCTIONS SIMULATION

For each source of our sample, we simulate a HEP probability distribution from which we expect the measured HEP to be a random variable. In order to do this, we need to compute the model dependent expected number of counts per source between energies E_1 and E_2, given by,

$$N_{E_1 E_2} = \int_{E_1}^{E^2} \exp\left(-\tau(E, z, \theta)\right) \phi(E) \epsilon(E) dE. \tag{5.3.1}$$

The first term in the equation is the photon survival probability that depends on the propagation model, where the parameter $\theta = (m_a, g_{a\gamma})$ represents the mass of the axion and the coupling to photons. From now on, θ_0 and θ_1 represent the null and the alternative hypothesis, respectively. The alternative hypothesis is a composite hypothesis, since it consists of a set of points in the ALPs parameter space $(m_a, g_{a\gamma})$. The part of the parameter space we choose to test is a rectangular grid with $m_a \in (0.1, 10)$ neV and $g_{a\gamma} \in (0.5, 7) \cdot 10^{-11}\,\mathrm{GeV}^{-1}$. For higher masses, the photon-ALPs mixing in the IGM takes place at higher energies, outside the *Fermi*-LAT range. For lower couplings, the amplitude of the mixing is too small to be detected. All the survival probabilities were computed for both models, with the fiducial parameter values described in Section 5.2.2.

The second term is the intrinsic spectrum of each source, computed following the method of Section 5.1.2. All intrinsic spectral fits are shown in Appendix A. The last term is the exposure map of the *Fermi*-LAT, an integral of the total instrument response function over the entire ROI. In the *Fermi* ScienceTools, exposure maps, which are usually integrals of the effective area over exposure time, are integrals of the response functions over the entire ROI. They depend upon the photon energy due to the direct dependency of the IRFs on such variable. All the exposure maps at the source locations, taken from the 2FHL catalog analysis, can be seen in Fig. 5.3.1. From Eq. 5.3.1, we can compute the observed source counts in the entire ROI given a propagation model, an intrinsic spectral model and the exposure map.

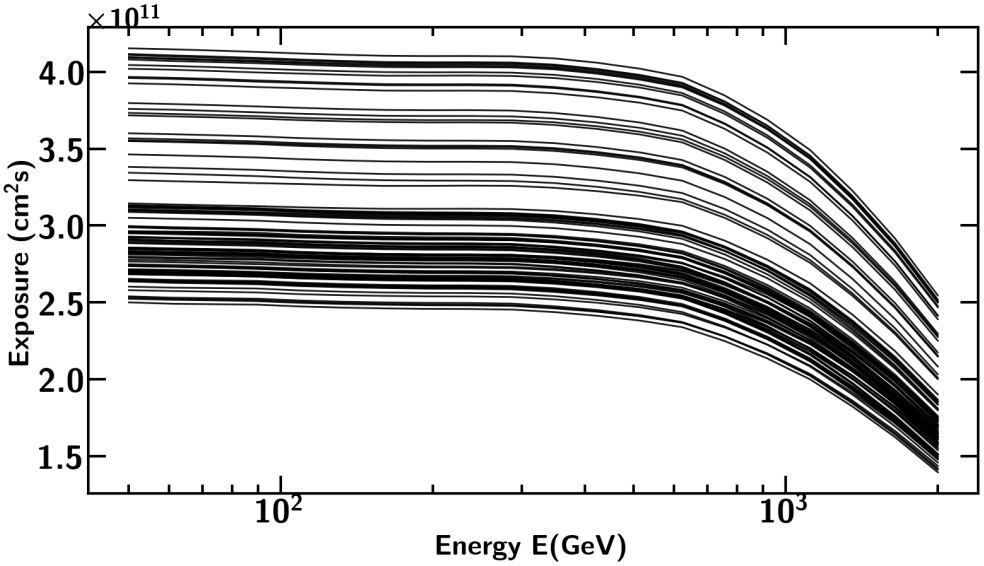

Figure 5.3.1: Exposure as a function of the energy, evaluated at the pixel location of each source in the 2FHL catalog ROIs. Data were taken from Ref. [17].

Through the whole simulation, we use 40 logarithmically spaced energy bins from 50 GeV to 2 TeV, the same range as in the 2FHL catalog. For each source, energy bin and propagation model, we compute the expected number of events with Eq. 5.3.1. An example can be seen in Fig. 5.3.3. The probability of detecting c counts is,

$$p = N^c \frac{\exp(-N)}{c!} \tag{5.3.2}$$

where N is the expected number of counts by the model, taken as the average frequency of the Poisson distribution. We use this equation to generate MC events per energy bin. One MC realization yields the simulated observed counts for a source during the chosen exposure time. For every realization, the last non-empty energy bin is taken as the bin with the HEP. In order to obtain the HEP p.d.f. for a given source and attenuation model, we repeat this process 10 thousand times. An example of the simulated HEPs can be seen in Fig. 5.3.2, examples of the expected counts can be seen in Figs. 5.3.2 and 5.3.3, and examples of the p.d.f.s. are displayed in Figs. 5.3.5, 5.3.6 and 5.3.7.

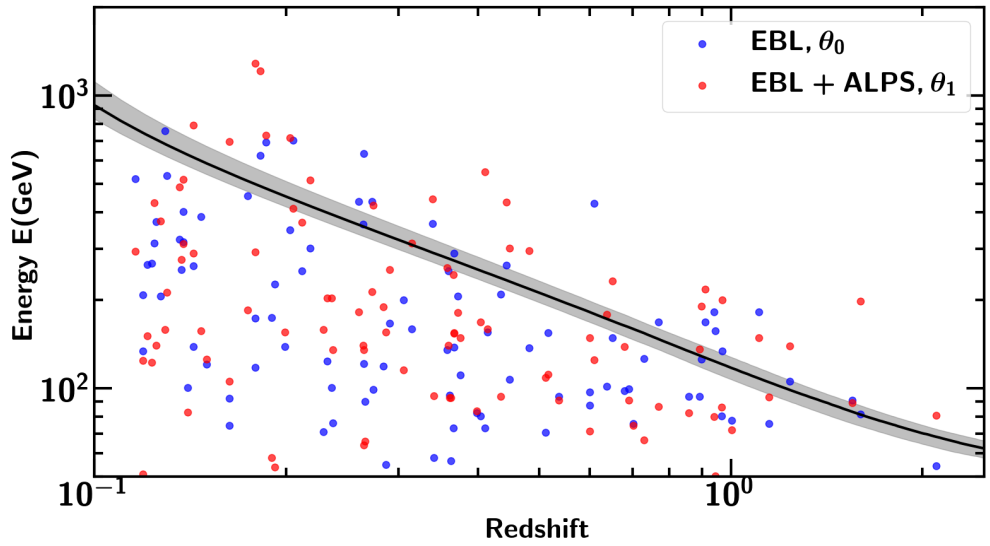

Figure 5.3.2: MC simulation of a set of HEPs. Blue points represent the null hypothesis, whereas red points correspond to the alternative hypothesis for $m = 1$ neV and and $g_{11} = 7$. The solid black line is the CGRH.

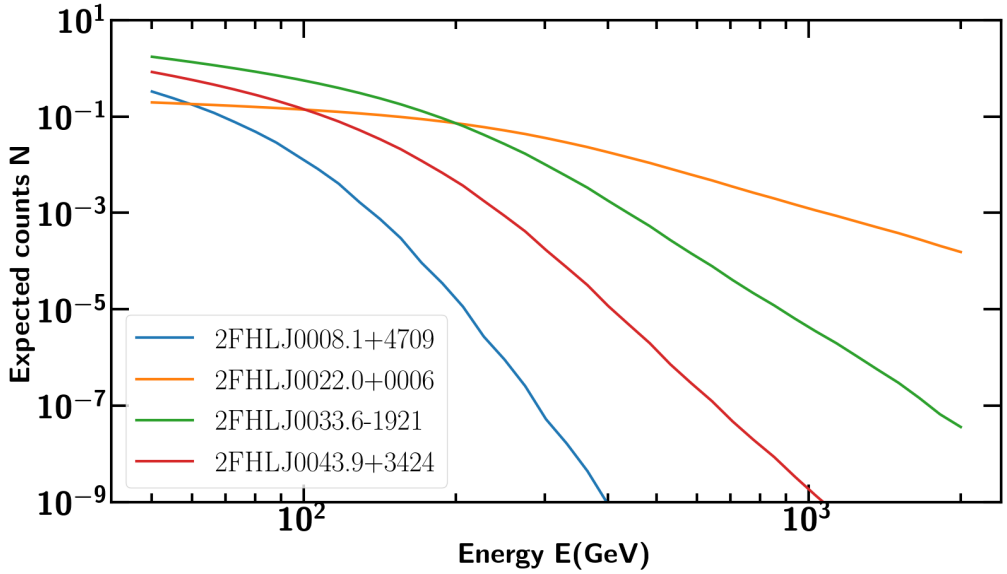

Figure 5.3.3: Expected counts for different sources in the sample, computed under the null hypothesis.

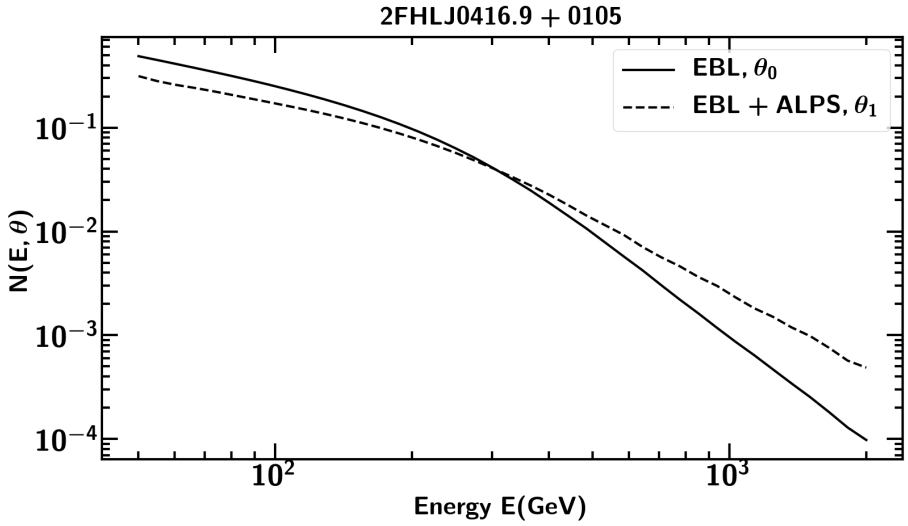

Figure 5.3.4: Expected counts for a source. Solid line: null hypothesis. Dashed line: alternative hypothesis for $m = 1$ neV and $g_{11} = 7$.

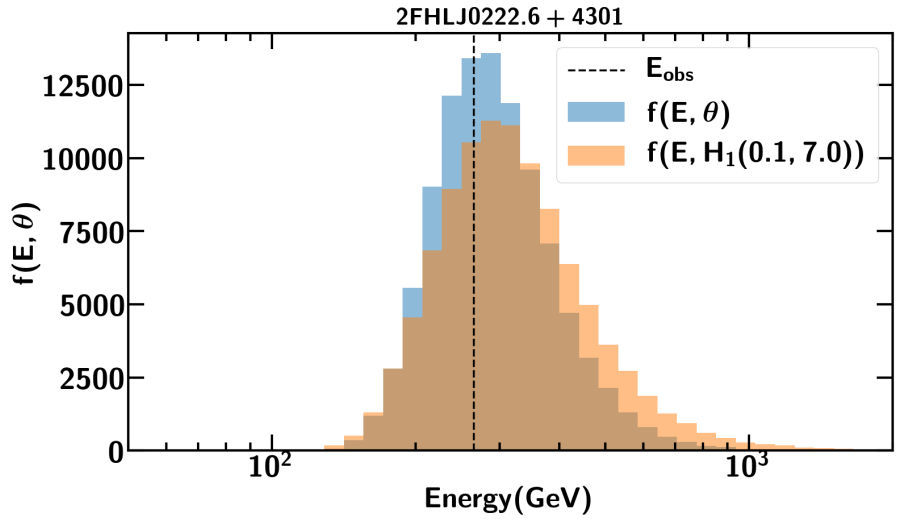

Figure 5.3.5: Simulated p.d.f.s. for a source in the sample. Blue: null hypothesis. Orange: alternative hypothesis for $m = 0.1$ neV and $g_{11} = 7$. The dashed line represents the observed HEP for the source.

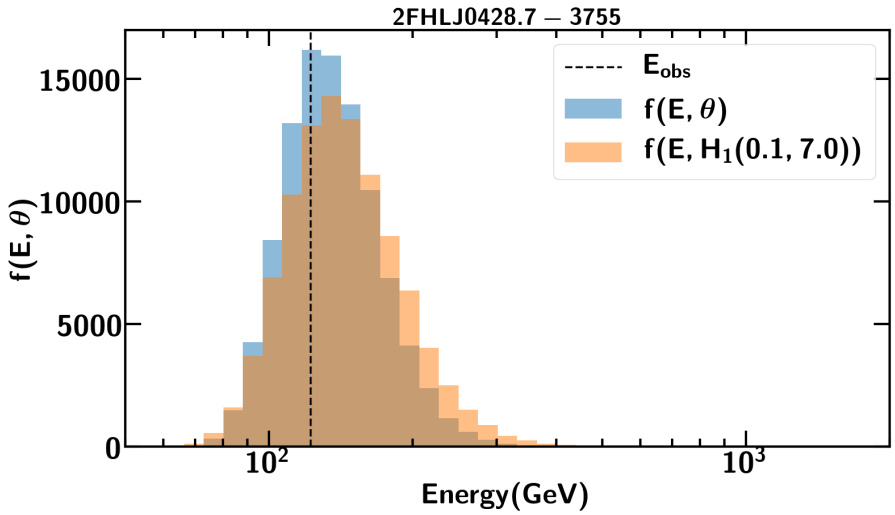

Figure 5.3.6: Simulated p.d.f.s. for a source in the sample. Blue: null hypothesis. Orange: alternative hypothesis for $m = 0.1$ neV and $g_{11} = 7$. The dashed line represents the observed HEP for the source.

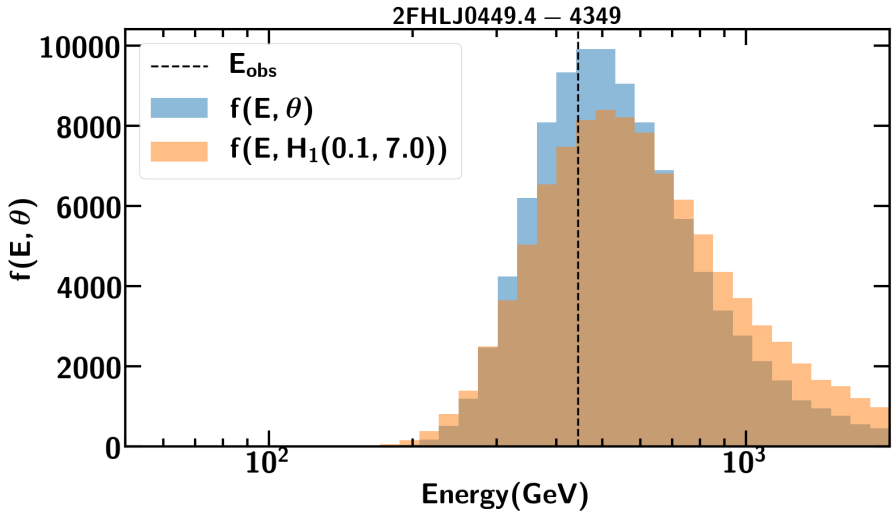

Figure 5.3.7: Simulated p.d.f.s. for a source in the sample. Blue: null hypothesis. Orange: alternative hypothesis for $m = 0.1$ neV and $g_{11} = 7$. The dashed line represents the observed HEP for the source.

5.4 COMBINED LIKELIHOOD ANALYSIS

5.4.1 The likelihood ratio test

For a random variable x, distributed according to a p.d.f., $f(x, \theta)$, where θ is any parameter of the function, the probability for a measurement x_i to be in $[x_i, x_i + dx_i]$ is $f(x_i, \theta)dx_i$. Assuming N independent observations of x, the joint likelihood function is [296],

$$L(x_1, x_2, ..., x_N|\theta) = \prod_{i=1}^{N} f(x_i, \theta). \tag{5.4.1}$$

In this analysis, the highest-energy photon of each source is the random variable of Eq. 5.4.1 and the probability distributions are the ones simulated in Section 5.3. Since the observations of different sources are independent, the joint likelihood is the product of likelihoods for each individual source. For the null hypothesis with no ALPs, the parameter θ is set to $\theta = (m_a, g_{a\gamma}) = (0, 0)$. For the alternative hypothesis, which includes ALPs, the parameter is $\theta = (m_a, g_{a\gamma})$. The joint likelihood function is given by

$$L(E_1, E_2, ..., E_N|m_a, g_{\gamma a}) = \prod_{i=1}^{N} f(E_i, m_a, g_{\gamma a}). \tag{5.4.2}$$

For each model and source, we compute the likelihoods of all the HEP events in our sample, and then combine them with Eq. 5.4.2. In order to draw any conclusions, we perform a statistical hypothesis test between the two models. The test-statistic (TS) is defined as the log-likelihood ratio test,

$$\Lambda(E_1, E_2...E_N) = 2\log\left(\frac{L(E_1, E_2, ..., E_N|\max\theta_1)}{L(E_1, E_2, ..., E_N|\max\theta_0)}\right). \tag{5.4.3}$$

In order to test each point in the parameter space, we compare the observed value of Λ, Λ_{obs}, with different thresholds of rejection or detection. These thresholds are computed from the simulated Λ test-statistic distributions. The null Λ distribution, $f(H_0)$, is derived by generating Monte Carlo events with the null hypothesis. Since the alternative hypothesis is composite, one distribution must be simulated per grid point, $f(H_1(m_a, g_{\gamma a}))$. In the same way that we derive the null distribution, the alternative distributions are obtained by generating events under the corresponding alternative hypotheses. Figs. 5.4.1 and 5.4.2 display the likelihood profiles over the chosen ALPs parameter space, for different values of the IGMF strength.

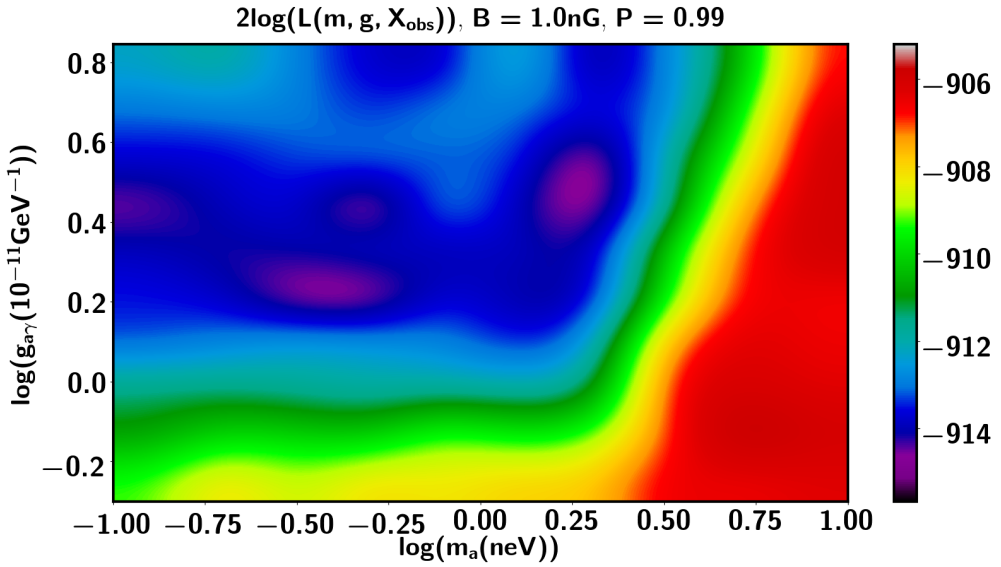

Figure 5.4.1: Likelihood as a function of the ALP mass and coupling, for $B = 1$ nG. $X_{obs} = (E_1, E_2, ...E_N)$ are the energies of the HEP events.

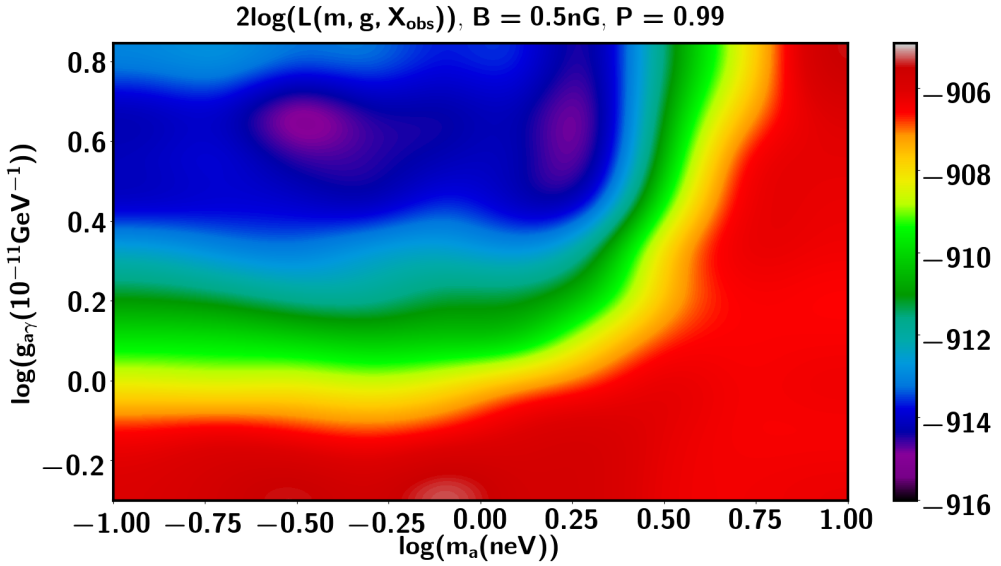

Figure 5.4.2: Likelihood as a function of the ALP mass and coupling, for $B = 0.5$ nG. $X_{obs} = (E_1, E_2, ...E_N)$ are the energies of the HEP events.

5.5 RESULTS

5.5.1 Resulting upper limits

We apply the likelihood analysis of the previous section to our sample of AGN and test ALPs parameters on a logarithmic 10×10 $(m_a, g_{a\gamma})$ grid where $0.1 \leq m_a \leq 10$ neV and $0.5 \leq g_{11} \leq 7.0$. An alternative TS distribution is simulated per grid point, and one example of such distributions for both hypotheses, $f(H_0)$ and $f(H_1(m_a, g_{a\gamma}))$, is shown in Fig. 5.5.1, for $m_a = 1.3$ neV and $g_{11} = 5.2$. The observed TS, $\Lambda_{obs} = -4.7$, found with the HEP data, is shown too. As can be seen in the plot, $\Lambda_{obs} < \Lambda_{thr}$, therefore no evidence for ALPs was found in these data, for this particular point in the parameter space. An upper limit is set by computing the 95% exclusion threshold $\Lambda_{exc}(m_a, g_{a\gamma})$, also shown in the figure, and testing if $\Lambda_{obs} < \Lambda_{exc}$.

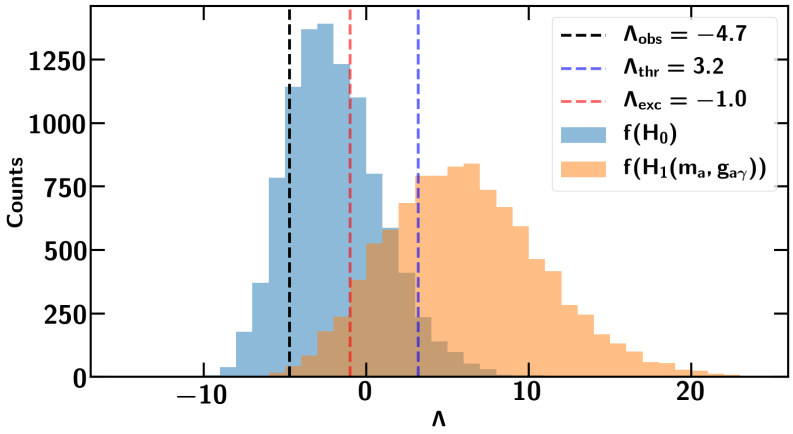

Figure 5.5.1: Blue: null TS distribution. Orange: alternative TS distribution for $m_a = 1.3$ neV and $g_{11} = 5.2$. Dashed black line: observed TS. Dashed blue line: 2σ detection threshold. Dashed red line: 95% confidence exclusion threshold.

The resulting upper limits can be seen in Fig. 5.5.2. Photon-ALP couplings between $1.0 \lesssim g_{11} \lesssim 7.0$ are excluded for masses below $m_a \lesssim 3.0$ neV, assuming that the IGMF strength is $B_T = 1$ nG. The right side of the contour follows the constant critical energy diagonal from Eq. 4.2.17, which is proportional to $\sim m_a^2/g_{11}$ for a fixed field strength. The lower part of the contour, the horizontal line around $g_{11} \sim 1$, depends on the amplitude of the oscillations, given by the product $B_T \cdot s$. For small values of this product, the conversion probabilities are too small to yield a significant difference

in the distributions. Since the product $B_T \cdot s$ does not depend upon the ALP mass, the limits extend to arbitrarily small masses, until $m_a^2 < \omega_{pl,neV}^2$ and the effective mass takes the value of the plasma frequency of the medium. This behavior was expected already in the homogeneous field case described in Section 4.2 and seen in the conversion probabilities of Fig. 4.2.1. The upper contour is the CAST limit [224]. The fluctuations in the contours are due to the limited number of MC simulations and magnetic field realizations.

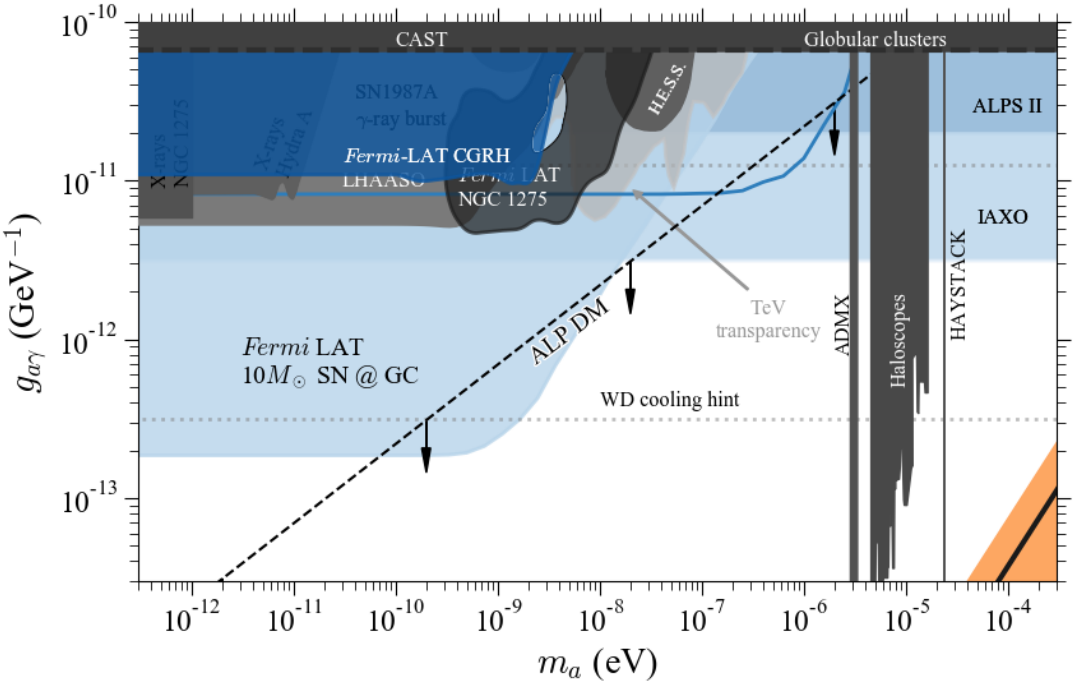

Figure 5.5.2: **Deep blue**: 95% confidence exclusion region derived in this work for $B = 1$ nG. **Grey**: limits from other experiments. **Sky blue**: sensitivities for future experiments. **Orange**: QCD axion. Below the black dashed line ALPs are candidates for the totality of cold dark matter in the Universe. It is important to underline that these limits strongly depend on the assumed fiducial magnetic field parameters for the IGMF. As shown in Fig. 5.5.3, reducing the magnetic field strength decreases the size of the exclusion region, until we cannot set any constraints, e.g. for B= 0.1 nG and $s = 1$ Mpc. Setting the the coherence length to larger values yields an exclusion region of larger size. This happens because the conversion probability depends on the $B{\cdot}s$ product and the critical energy, as seen in Eqs. 4.2.17 and 4.2.18. This means that we can derive sets of limits for a wide range of values of the magnetic field parameters. Our results take one of the best possible values within the allowed bounds of Fig. 5.2.6.

The limits derived in this work constrain a part of the unexplored parameter space, the hole around $g_{11} \sim 3$ and $m_a \sim 3$ neV on the limits derived by the NGC 1275 analysis performed by the *Fermi*-LAT collaboration. Our limits are also compatible with the limits of other experiments, the SN 1987A γ burst experiment results [240] and with previous *Fermi*-LAT limits [207]. At lower masses, they are also compatible with X-rays experiments, since the IGMF survival probabilities saturate. Even when most of the excluded region has already been covered by these experiments, it is a completely new area of the parameter space for current γ-ray telescopes, serving as a cross-check for all the limits derived under different conversion regions and astrophysical objects. All these bounds together strongly constrain part of the parameter space in which ALPs can contribute to the transparency of the Universe to γ rays. The constraints are also within the planned sensitivities of future ALPs experiments, such as ALPS II and IAXO, seen as the two sky blue horizontal bands in Fig. 5.5.2. None of these limits constrain the region where ALPs could compose the entirety of dark matter content of the Universe [222], which is below the dashed black line in Fig. 5.5.2.

It is important to remark that the magnetic field models cover a wide range of values that could be generated during the early Universe, at the epoch of Inflation, phase transitions or recombination [276], whereas our limits were derived assuming a specific set of magnetic field parameters corresponding to one of the best scenarios for the mixing. Due to this, we also derived different sets of limits by modifying these model parameters within allowed values. First, decrease the field strength to $B = 0.5$ nG and $B = 0.1$ nG. The former value yields a reduction in the excluded area of $\sim 30\%$ compared to the initial case, while for the latter we cannot set any upper limits. This is because the amplitude of oscillation, governed by $\sim g_{\gamma a} \cdot B \cdot s$, decreases to values in which the *Fermi*-LAT ceases to be sensitive. We also increase the coherence length of the field to $s = 5$ Mpc, which yields an increase of roughly $\sim 30\%$ in the limits. The results are seen in Fig. 5.5.3.

The limits presented in this work can be improved by extending the likelihood analysis to Cherenkov telescopes, which can observe the γ-ray Universe up to ~ 30 TeV. At these energies, the part of the parameter space corresponding to higher values of the ALPs mass can be probed. In this mass range, the conversion is further enhanced by the GMF, which needs to be taken into account. On the other hand, cosmic magnetic field morphologies are not fully understood yet. Better observations of such fields are needed in order to reduce the size of the magnetic field parameter space, which is of crucial importance for the photon-ALP mixing.astrophysical analyses. In this regard, future

experiments like JVLA, ALMA, and SKA will be able to improve cosmic magnetic fields measurements [297].

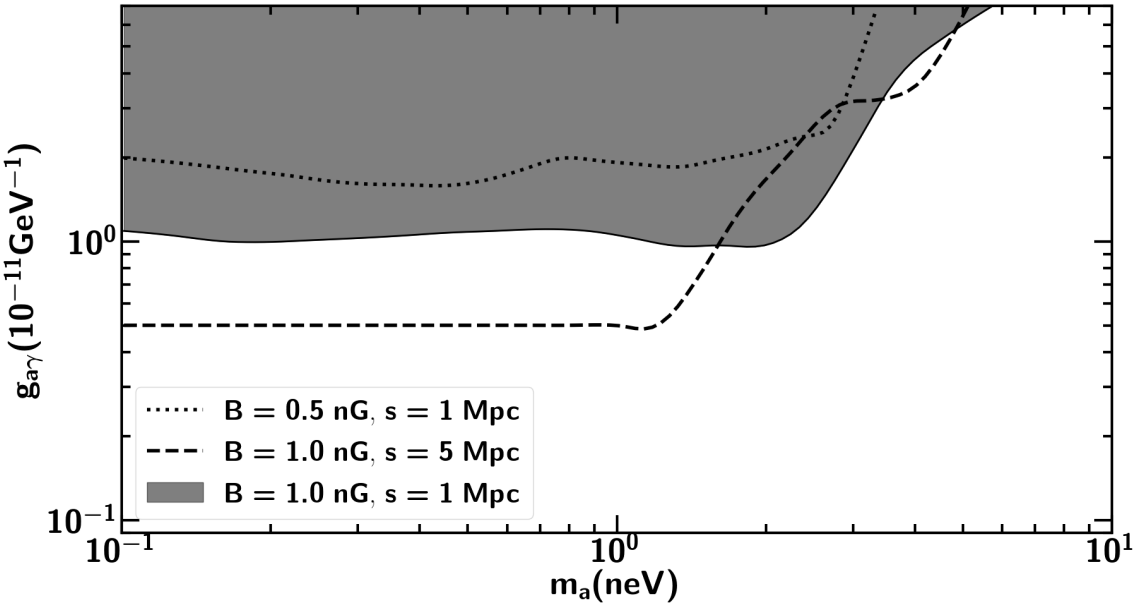

Figure 5.5.3: **Shaded region**: results of Section 5 derived with $B = 1$ nG and $s = 1$ Mpc. **Dotted line**: results derived withderived with $B = 0.5$ nG and $s = 1$ Mpc. **Dashed line**: results derived with $B = 1$ nG and $s = 5$ Mpc.

5.5.2 Systematic uncertainties

In order to evaluate systematics associated to model parameters and analysis choices, we derive different sets of limits repeating the simulation and analysis procedures of the previous sections and compute the percentual changes in the contours. All results presented in this work, were derived with the Dominguez et al. EBL model [150]. We test the effects of choosing a different model by repeating the analysis with the Finke et al. model [143]. This model is different than the default one and it is compatible with current EBL constraints. As seen in Fig. 5.5.6, the resulting upper limits increase by $\sim 15\%$.

Equation 4.2.25 computes the average survival probability over IGMF realizations along the line of sight of each source. The oscillating contours from Fig. 5.5.2 are due to a limited number of simulations and magnetic field realizations. These two effects are tested for a different set of pseudo experiments and field realizations, resulting in the limits of Fig. 5.5.4. The exclusion region area modifications are smaller than $\sim 10\%$.

In Section 2.4, we discussed the AGN data sample and took sources based on the HEP probability to belong to a source. All of the sources in the 2FHL catalog have a HEP with $P \geq 0.85$, with most of them above $P \geq 0.99$, due to the low background of the LAT at high energies. Selecting sources with higher values of P allows us to reduce the events that come from background. However, this also entails a reduction of statistics in our sample. We tested the effects of different HEP probability cuts within one realization, resulting in contours with area changes smaller than $\sim 10\%$, as displayed in Fig. 5.5.5.

Finally, we did not consider the uncertainties in the energy reconstruction in the simulation. The reason for this is that, above 1 GeV, these effects are below 10% at 68% confidence and therefore we do not expect a large impact in cutoff of hard sources, or in the HEP events.

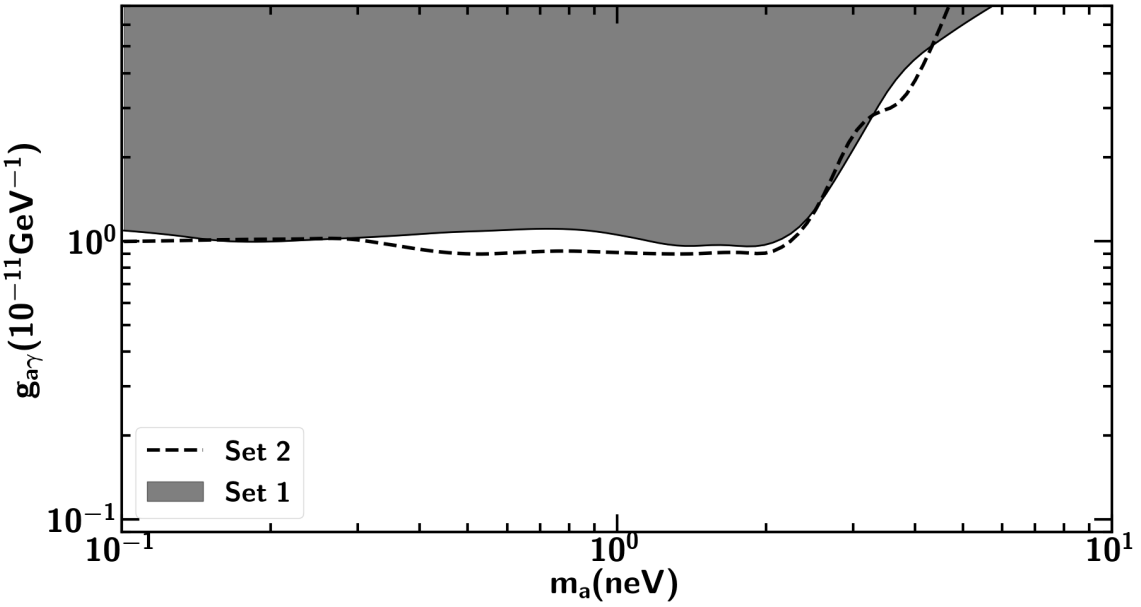

Figure 5.5.4: **Shaded region**: results of Section 5 derived with the average of a set of magnetic field realizations. **Dashed line**: results derived with a different set of realizations.

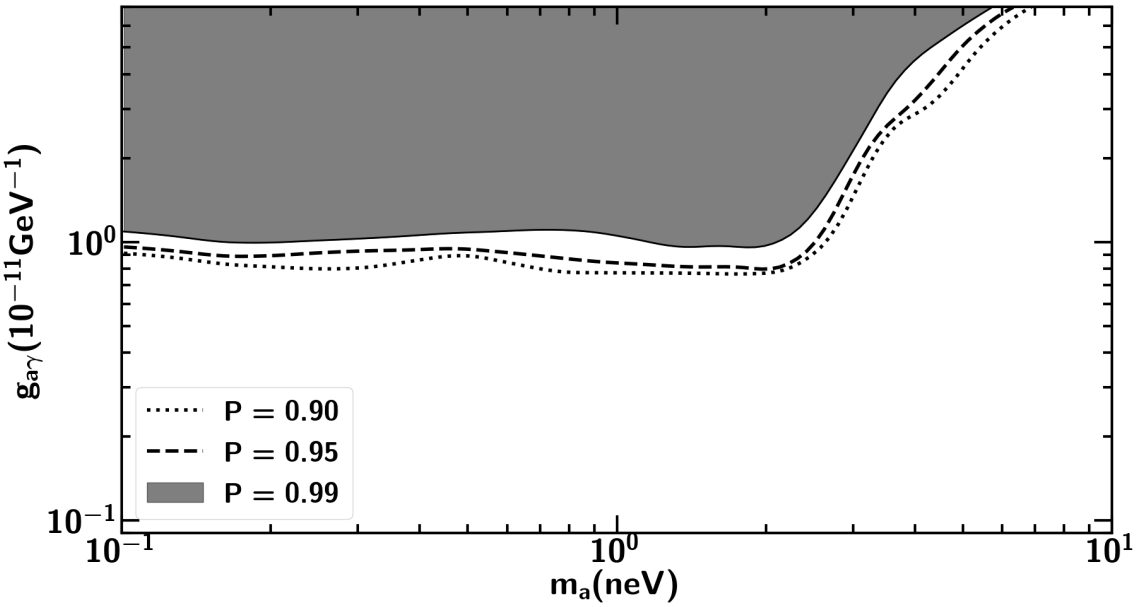

Figure 5.5.5: **Shaded region**: results of Section 5 derived with $P = 0.99$. **Dashed line**: results derived with $P = 0.95$. **Dotted line**: Results derived with $P = 0.90$.

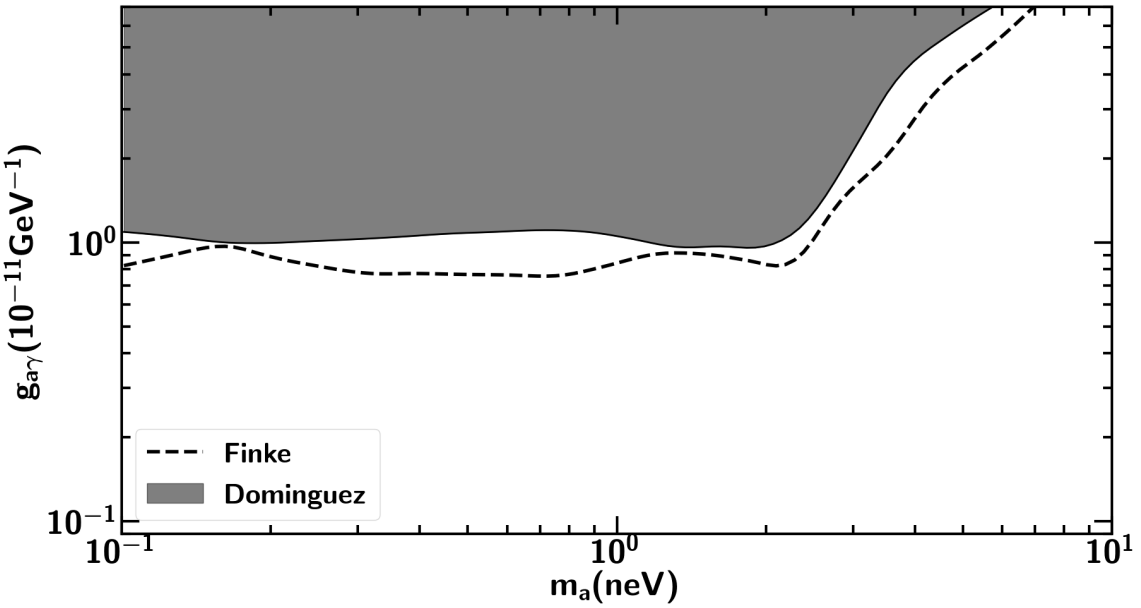

Figure 5.5.6: **Shaded region**: results of Section 5 derived with the Dominguez et al. EBL model. **Dashed line**: results derived with the Finke et al. EBL model.

Chapter 6

SUMMARY AND OUTLOOK

The non-observation of CP violation in neutron dipole moment experiments hints that a part of the QCD Lagrangian must be extremely small. This is known as the strong CP problem. Axions arise from the Peccei-Quinn mechanism as a possible solution to this problem. In a similar manner, theories beyond the SM predict the existence of ALPs, which can have observational effects on photons in the presence of magnetic fields. From synchrotron emission and Faraday rotation measurements, we know that magnetic fields exist over large scales in the Universe, opening up the possibility to search for these particles in astrophysics. If ALPs exist, γ-ray photons can oscillate into them in these cosmic magnetic fields. The conversion probability is maximal above a critical energy that depends on the ALPs parameters and the strength of the field.

Within the SM, the origin of the opacity of the Universe to γ-rays is the QED photon-photon annihilation process. HE and VHE photons undergo this annihilation mechanism with the EBL when they travel through the IGM. Thus, there is a survival probability for each γ ray that depends upon its energy and the traveled distance, and acts as an attenuation factor for the spectra of γ-ray sources. Due to this attenuation, the maximum energy of photons that survive the EBL is reduced for a given redshift. If a photon turns into an ALP, it avoids the EBL attenuation process, modifying the transparency of the Universe to γ rays. The observed HEP of a source should change according to the attenuation model, making it possible to search for ALPs with these HEP events.

In this Dissertation, we have studied the opacity of the Universe to HE γ-rays with the HEP events observed with the *Fermi*-LAT. As sample of sources, we used the AGN

registered in the 2FHL catalog. Only sources with redshift above $z = 0.1$ and event probabilities of belonging to the corresponding sources greater than $P = 0.99$ were taken into account. For these sources, we simulate the HEP p.d.f.s in the presence and absence of ALPs, with mixing in the IGM. We probed the ALPs parameter space between $0.1 \leq m_a \leq 10$ neV and $0.5 \leq g_{11} \leq 7.0$. For each source, we obtained the likelihood of the HEP event with its corresponding p.d.f. and then we carried out a joint likelihood analysis with all the sources. We found no evidence of an increased transparency of the Universe compatible with ALPs and thus we set upper limits. For $B = 1$ nG and $s = 1$ Mpc, we excluded photon-ALP couplings above $1 \cdot 10^{-11}$ GeV^{-1} for ALP masses $m_a \lesssim 3.0$ neV.

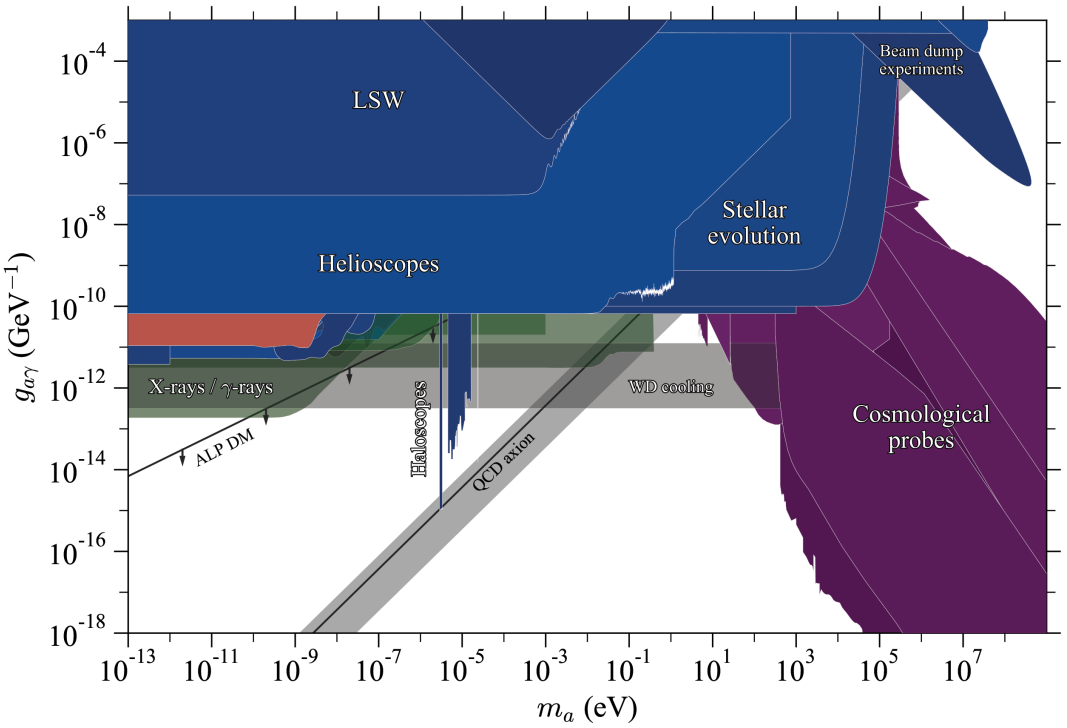

Figure 6.0.1: **Orange**: limits derived in this work. **Blue**: excluded regions with laboratory and astrophysical searches. **Purple**: excluded regions with cosmological searches. **Green**: expected sensitivities of future experiments. **Gray**: QCD axion. Fig. courtesy of Manuel Meyer.

A comparison of the results with all the previous limits and expected sensitivities can be seen in Fig. 6.0.1. The limits are compatible with other bounds derived under different mixing models, strongly constraining the part of the parameter space where

ALPs could modify the transparency of the Universe in the coincident regions. Our results are also within the sensitivities of future experiments, specifically IAXO and ALPS II, which will probe lower couplings and higher masses. A part of the parameter space where ALPs could affect the transparency of the Universe remains unexplored. For these masses, the critical energy of the mixing lies within the energy range of current Cherenkov telescopes and the future Cherenkov Telescope Array (CTA).

Unlike satellite γ-ray telescopes, Cherenkov telescopes have a higher background rate and the analysis cannot be extended with the individual HEP of each source. The number of observed events between energies E_1 and E_2 above the critical energy, can be used as the data, provided they satisfy a significance threshold. In this scenario, the p.d.f.s are model dependent Poisson distributions and do not need to be simulated. Additionally, the GMF must be included as a mixing region, since it enhances the survival probability at TeV energies for ALPs masses ≥ 1 neV. Regarding the intrinsic spectra of blazars, the fits can be carried out by de-absorbing spectral points below the critical energy, for which the conversion probability is still not maximal. ALPs masses up to 10 neV fall within the energy range of current Cherenkov telescopes, allowing us to probe part of the hole around $g_{11} \sim 3$ and $m_a \sim 3$ neV, which has not been excluded so far. A similar analysis could also be carried out with the future CTA, a γ-ray observatory that will be sensitive to photons up to 300 TeV. At these energies, ALPs masses until 10^2 neV can be explored, assuming that we use the same IGMF parameters used in this work, in addition to conversion in the GMF. Finally, better measurements of the EBL intensity and cosmic magnetic fields will be crucial for reducing the systematic uncertainties associated to these models.

The ALPs parameter space is large and invisible axion and ALPs models remain to be tested. These pseudo-scalar particles could be the key for solving the strong CP problem of QCD, with the additional advantage of being viable dark matter candidates and new particles beyond the SM.

Appendix A

SAMPLE OF SOURCES

Source	Redshift	Source	Redshift
2FHLJ0008.1+4709	2.100	2FHLJ1015.0+4926	0.212
2FHLJ0022.0+0006	0.306	2FHLJ1031.2+7441	0.123
2FHLJ0033.6-1921	0.610	2FHLJ1031.4+5052	0.361
2FHLJ0043.9+3424	0.966	2FHLJ1053.5+4930	0.140
2FHLJ0114.9-3359	0.482	2FHLJ1058.5+5625	0.143
2FHLJ0115.8+2519	0.358	2FHLJ1104.0-2331	0.186
2FHLJ0123.7-2308	0.404	2FHLJ1116.9+2014	0.138
2FHLJ0141.3-0927	0.730	2FHLJ1120.8+4212	0.124
2FHLJ0221.1+3556	0.944	2FHLJ1125.6-3555	0.284
2FHLJ0222.6+4301	0.444	2FHLJ1136.8+6737	0.136
2FHLJ0237.6-3605	0.411	2FHLJ1137.9-1710	0.600
2FHLJ0238.4-3116	0.232	2FHLJ1217.9+3006	0.130
2FHLJ0238.8+1631	0.940	2FHLJ1221.3+3009	0.182
2FHLJ0244.9-5820	0.265	2FHLJ1224.4+2435	0.218
2FHLJ0303.3-2407	0.260	2FHLJ1224.7+2124	0.435
2FHLJ0304.5-0054	0.511	2FHLJ1231.7+2848	0.236
2FHLJ0316.1+0905	0.372	2FHLJ1256.2-0548	0.536
2FHLJ0319.7+1849	0.190	2FHLJ1309.5+4305	0.691
2FHLJ0326.0-1644	0.291	2FHLJ1312.6+4828	0.638
2FHLJ0326.3+0227	0.147	2FHLJ1404.9+6555	0.363
2FHLJ0416.9+0105	0.287	2FHLJ1418.0+2543	0.237
2FHLJ0422.9+1947	0.516	2FHLJ1427.3-4204	1.552
2FHLJ0428.7-3755	1.105	2FHLJ1428.5+4239	0.129
2FHLJ0433.6+2907	0.970	2FHLJ1437.0+5639	0.150
2FHLJ0440.3-2458	0.600	2FHLJ1442.9+1159	0.163
2FHLJ0449.4-4349	0.205	2FHLJ1506.8+0813	0.376
2FHLJ0456.9-2323	1.003	2FHLJ1512.7-0906	0.360
2FHLJ0507.9+6737	0.340	2FHLJ1517.7+6526	0.702
2FHLJ0538.6-4406	0.892	2FHLJ1548.7-2249	0.192
2FHLJ0543.9-5533	0.273	2FHLJ1748.7+7004	0.770
2FHLJ0622.4-2604	0.414	2FHLJ1801.2+7828	0.680
2FHLJ0631.0-2406	1.238	2FHLJ1917.7-1921	0.137
2FHLJ0648.6+1516	0.179	2FHLJ1936.9-4721	0.265
2FHLJ0650.7+2502	0.203	2FHLJ1958.3-3011	0.119
2FHLJ0710.5+5908	0.125	2FHLJ2000.9-1749	0.652
2FHLJ0721.9+7121	0.127	2FHLJ2016.5-0904	0.367
2FHLJ0744.2+7435	0.315	2FHLJ2116.1+3339	1.596
2FHLJ0756.8+0955	0.266	2FHLJ2131.4-0914	0.449
2FHLJ0805.8+7534	0.121	2FHLJ2150.3-1411	0.229
2FHLJ0809.7+5218	0.138	2FHLJ2153.1-0041	0.341
2FHLJ0811.6+0146	1.148	2FHLJ2158.8-3013	0.116
2FHLJ0825.9-2230	0.911	2FHLJ2249.9+3826	0.119
2FHLJ0847.2+1133	0.199	2FHLJ2254.0+1613	0.859
2FHLJ0950.2+4553	0.399	2FHLJ2314.0+1445	0.163
2FHLJ0952.2+7503	0.179	2FHLJ2324.7-4041	0.174
2FHLJ0957.6+5523	0.899	2FHLJ2329.2+3754	0.264
2FHLJ0958.3+6535	0.367	2FHLJ2340.8+8014	0.274
2FHLJ1010.2-3119	0.143	2FHLJ2343.5+3438	0.366

Table A.1: List of sources with redshifts $z \geq 0.1$.

Appendix B

FIT QUALITIES

Source	**Shape**	χ^2	**ndf**	**p-val**
2FHLJ0008.1+4709	pow	3.213	2.0	0.201
2FHLJ0022.0+0006	pow	0.985	2.0	0.611
2FHLJ0033.6−1921	log	1.461	2.0	0.482
2FHLJ0043.9+3424	log	0.956	2.0	0.62
2FHLJ0114.9−3359	log	0.278	2.0	0.87
2FHLJ0115.8+2519	pow	0.648	3.0	0.885
2FHLJ0123.7−2308	pow	0.166	2.0	0.921
2FHLJ0141.3−0927	pow	0.983	3.0	0.805
2FHLJ0221.1+3556	log	1.48	2.0	0.477
2FHLJ0222.6+4301	log	1.43	2.0	0.489
2FHLJ0237.6−3605	pow	1.472	2.0	0.479
2FHLJ0238.4−3116	pow	6.716	4.0	0.152
2FHLJ0238.8+1631	log	1.454	1.0	0.228
2FHLJ0244.9−5820	pow	10.351	4.0	0.035
2FHLJ0303.3−2407	pow	7.601	3.0	0.055
2FHLJ0304.5−0054	pow	0.453	2.0	0.797
2FHLJ0316.1+0905	log	1.042	1.0	0.307
2FHLJ0319.7+1849	pow	1.018	3.0	0.797
2FHLJ0326.0−1644	pow	3.981	3.0	0.264
2FHLJ0326.3+0227	pow	2.419	3.0	0.49
2FHLJ0416.9+0105	pow	0.778	3.0	0.855
2FHLJ0422.9+1947	pow	2.702	2.0	0.259
2FHLJ0428.7−3755	log	2.528	1.0	0.112
2FHLJ0433.6+2907	log	1.692	2.0	0.429

Table B.1: Fit results for the 2FHL catalog sources with redshifts $z \geq 0.1$.

Source	**Shape**	χ^2	**ndf**	**p-val**
2FHLJ0440.3−2458	log	0.024	1.0	0.877
2FHLJ0449.4−4349	log	1.831	1.0	0.176
2FHLJ0456.9−2323	log	0.463	1.0	0.496
2FHLJ0507.9+6737	pow	4.778	2.0	0.092
2FHLJ0538.6−4406	log	0.093	1.0	0.76
2FHLJ0543.9−5533	log	0.82	2.0	0.664
2FHLJ0622.4−2604	pow	5.604	2.0	0.061
2FHLJ0631.0−2406	log	1.406	2.0	0.495
2FHLJ0648.6+1516	log	0.26	3.0	0.967
2FHLJ0650.7+2502	log	0.498	2.0	0.78
2FHLJ0710.5+5908	log	2.375	3.0	0.498
2FHLJ0721.9+7121	log	0.144	2.0	0.93
2FHLJ0744.2+7435	pow	1.828	3.0	0.609
2FHLJ0756.8+0955	pow	3.504	3.0	0.32
2FHLJ0805.8+7534	log	1.084	3.0	0.781
2FHLJ0809.7+5218	log	1.301	3.0	0.729
2FHLJ0811.6+0146	log	2.548	2.0	0.28
2FHLJ0825.9−2230	pow	2.181	2.0	0.336
2FHLJ0847.2+1133	pow	5.598	3.0	0.133
2FHLJ0950.2+4553	pow	3.59	2.0	0.166
2FHLJ0952.2+7503	log	0.27	1.0	0.603
2FHLJ0957.6+5523	log	2.064	2.0	0.356
2FHLJ0958.3+6535	log	0.983	1.0	0.322
2FHLJ1010.2−3119	pow	1.132	2.0	0.568

Table B.2: Fit results for the 2FHL catalog sources with redshifts $z \geq 0.1$.

Source	**Shape**	χ^2	**ndf**	**p-val**
2FHLJ1015.0+4926	log	3.0	2.0	0.223
2FHLJ1031.2+7441	pow	3.358	4.0	0.5
2FHLJ1031.4+5052	log	3.7	3.0	0.296
2FHLJ1053.5+4930	pow	7.557	5.0	0.182
2FHLJ1058.5+5625	log	5.509	4.0	0.239
2FHLJ1104.0−2331	pow	2.126	3.0	0.547
2FHLJ1116.9+2014	pow	5.681	4.0	0.224
2FHLJ1120.8+4212	log	1.971	3.0	0.579
2FHLJ1125.6−3555	pow	3.135	4.0	0.536
2FHLJ1136.8+6737	log	1.441	4.0	0.837
2FHLJ1137.9−1710	log	0.524	1.0	0.469
2FHLJ1217.9+3006	log	3.382	3.0	0.336
2FHLJ1221.3+3009	log	6.104	3.0	0.107
2FHLJ1224.4+2435	log	2.482	3.0	0.479
2FHLJ1224.7+2124	log	3.409	2.0	0.182
2FHLJ1231.7+2848	log	5.409	3.0	0.144
2FHLJ1256.2−0548	log	0.909	1.0	0.34
2FHLJ1309.5+4305	log	0.029	1.0	0.865
2FHLJ1312.6+4828	log	0.462	2.0	0.794
2FHLJ1404.9+6555	log	1.364	2.0	0.506
2FHLJ1418.0+2543	pow	0.782	3.0	0.854
2FHLJ1427.3−4204	log	1.192	1.0	0.275
2FHLJ1428.5+4239	log	0.146	2.0	0.929
2FHLJ1437.0+5639	log	1.467	3.0	0.69

Table B.3: Fit results for the 2FHL catalog sources with redshifts $z \geq 0.1$.

Source	**Shape**	χ^2	**ndf**	**p-val**
2FHLJ1442.9+1159	pow	0.651	2.0	0.722
2FHLJ1506.8+0813	log	4.451	3.0	0.217
2FHLJ1512.7−0906	log	0.121	2.0	0.942
2FHLJ1517.7+6526	log	0.009	1.0	0.922
2FHLJ1548.7−2249	pow	0.563	3.0	0.905
2FHLJ1748.7+7004	log	0.414	1.0	0.52
2FHLJ1801.2+7828	log	0.319	1.0	0.572
2FHLJ1917.7−1921	log	0.125	2.0	0.94
2FHLJ1936.9−4721	pow	1.958	3.0	0.581
2FHLJ1958.3−3011	log	1.526	2.0	0.466
2FHLJ2000.9−1749	pow	0.044	2.0	0.978
2FHLJ2016.5−0904	log	2.258	2.0	0.323
2FHLJ2116.1+3339	log	0.04	1.0	0.841
2FHLJ2131.4−0914	log	1.166	2.0	0.558
2FHLJ2150.3−1411	log	0.152	2.0	0.927
2FHLJ2153.1−0041	pow	0.175	2.0	0.916
2FHLJ2158.8−3013	log	2.695	2.0	0.26
2FHLJ2249.9+3826	pow	3.356	3.0	0.34
2FHLJ2254.0+1613	log	1.116	2.0	0.572
2FHLJ2314.0+1445	log	3.726	4.0	0.444
2FHLJ2324.7−4041	log	0.36	1.0	0.548
2FHLJ2329.2+3754	log	1.792	2.0	0.408
2FHLJ2340.8+8014	log	1.622	2.0	0.444
2FHLJ2343.5+3438	pow	0.579	3.0	0.901

Table B.4: Fit results for the 2FHL catalog sources with redshifts $z \geq 0.1$.

ACKNOWLEDGEMENT

I would like to thank a lot of persons who supported and helped me during my PhD:

- my supervisors, Dr. Gernot Maier and Dr. Rolf Buehler, for allowing me to work with them on the compelling research topic of axions. Both have had great ideas to improve my work and I have learned a lot from them. They also gave me a chance to present my work at different scientific conferences, which helped me improve a bit a as a speaker.

- Dr. Andreas Ringwald and Dr. Axel Lindner for providing me the references to understand the theory behind axions. Dr. Manuel Meyer helped me a lot in this matter too, as well as easing some programming with his own axion scripts. Dr. Alberto Dominguez and Dr. Marcos Lopez helped me a lot with the spectral fits, a very important contribution for the analysis. Dr. Elisa Pueschel helped me a lot with extragalactic background light insight too.

- all the *Fermi*-LAT collaboration members, particularly the Dark Matter and New Physics group. They gave me a lot of useful feedback during the calls.

- my fellow PhD students (some of them are postdocs now!): Chiara, Giulio, Henrike, Konstantin, Maria, Matteo, Moritz, Nathan and Simone. We had great discussions, scientific or not. In particular, Matteo helped me a lot with Python and gave me the boost I needed to start my whole work. Konstantin and Maria gave me their german knowledge to translate the abstract.

- the postdocs that had the rough task to read my thesis when it was still raw, Mireia, Raul and Maria. They helped me improve its contents and make it readable. Thanks to Orel too, for helping me understand the hardest concepts of experimental physics and statistics. Finally, Tarek, for his absolute knowledge in programming that got me out of sticky situations.

- Siannah Penaranda and Jose Luis Alonso, two of the teachers that encouraged and motivated me the most during my degree.

- My mother Lyda and my aunt Diana, for their amazing family support during all the stages of my life. Without them, I would not be able to have a chance of studying a PhD at all.

- Stack Overflow posts, for reasons.

Bibliography

[1] Karl G. Jansky, "Radio Waves from Outside the Solar System", *Nature*, 132, 1933, p. 66, URL https://doi.org/10.1038/132066a0.

[2] A. A. Penzias and R. W. Wilson, "A Measurement of Excess Antenna Temperature at 4080 Mc/s.", *The Astrophysical Journal*, 142, 1965, pp. 419–421, URL http://adsabs.harvard.edu/abs/1965ApJ...142..419P.

[3] W. Forman, et al., "The fourth Uhuru catalog of X-ray sources.", *The Astrophysical Journal*, 38, 1978, pp. 357–412, URL http://adsabs.harvard.edu/cgi-bin/bib_query?1978ApJS...38..357F.

[4] W. Kraushaar, et al., "Explorer XI Experiment on Cosmic Gamma Rays.", *The Astrophysical Journal*, 141, 1965, p. 845, URL http://adsabs.harvard.edu/abs/1965ApJ...141..845K.

[5] C. Fichtel, "EGRET overview: Achievements in the light of expectations.", *Astronomy and Astrophysics, Supplement*, 120, 1996, pp. 23–29, URL http://adsabs.harvard.edu/abs/1996A%26AS..120C..23F.

[6] E. Lorenz and R. Wagner, "Very-high energy gamma-ray astronomy. A 23-year success story in high- energy astroparticle physics", *European Physical Journal H*, 37, 2012, pp. 459–513, URL https://ui.adsabs.harvard.edu/#abs/2012EPJH...37..459L.

[7] W. B. Atwood, et al., "The Large Area Telescope on the Fermi Gamma-Ray Space Telescope Mission", *The Astrophysical Journal*, 697, 2009, pp. 1071–1102, URL https://ui.adsabs.harvard.edu/#abs/2009ApJ...697.1071A.

[8] J. A. Hinton, "The Status of the H.E.S.S. project", *New Astronomy Review*, 48, 2004, pp. 331–337, URL https://arxiv.org/abs/astro-ph/0403052.

[9] R Firpo, "Status and results of the MAGIC telescope", *Journal of Physics: Conference Series*, 110(6), 2008, p. 062009, URL http://stacks.iop.org/1742-6596/110/i=6/a=062009.

[10] Jamie Holder, "VERITAS: Status and Highlights", *International Cosmic Ray Conference*, 11, 2011, p. 137, URL https://ui.adsabs.harvard.edu/#abs/2011ICRC...12..137H.

[11] J. Pretz, "Highlights from the High Altitude Water Cherenkov Observatory", in *34th International Cosmic Ray Conference (ICRC2015)*, 2015, vol. 34, p. 25, URL https://ui.adsabs.harvard.edu/#abs/2015ICRC...34...25P.

[12] Jan Conrad and Olaf Reimer, "Indirect dark matter searches in gamma and cosmic rays", *Nature Physics*, 13, 2017, pp. 224–231, URL https://ui.adsabs.harvard.edu/#abs/2017NatPh..13..224C.

[13] A. Ringwald, "Axions and Axion-Like Particles", *ArXiv e-prints*, 2014, p. arXiv:1407.0546, URL https://ui.adsabs.harvard.edu/#abs/2014arXiv1407.0546R.

[14] Russell M. Kulsrud and Ellen G. Zweibel, "On the origin of cosmic magnetic fields", *Reports on Progress in Physics*, 71, 2008, p. 046901, URL https://ui.adsabs.harvard.edu/#abs/2008RPPh...71d6901K.

[15] Miguel A. Sanchez-Conde, et al., "The search of axion-like-particles with Fermi and Cherenkov telescopes", *ArXiv e-prints*, 2010, p. arXiv:1001.1892, URL https://ui.adsabs.harvard.edu/#abs/2010arXiv1001.1892S.

[16] Alberto Franceschini and Giulia Rodighiero, "The extragalactic background light revisited and the cosmic photon- photon opacity", *Astronomy and Astrophysicsl*, 603, 2017, p. A34, URL https://ui.adsabs.harvard.edu/#abs/2017A&A...603A..34F.

[17] M. Ackermann, et al., "2FHL: The Second Catalog of Hard Fermi-LAT Sources", *The Astrophysical Journal Supplement Series*, 222, 2016, p. 5, URL https://ui.adsabs.harvard.edu/#abs/2016ApJS..222....5A.

[18] L. Cazon and for The Pierre Auger Collaboration, "The Pierre Auger Observatory: new results and prospects", *ArXiv e-prints*, 2018, p. arXiv:1808.00745, URL https://ui.adsabs.harvard.edu/#abs/2018arXiv180800745C.

[19] R. L. Diehl, "Particle acceleration in cosmic sites. Astrophysics issues in our understanding of cosmic rays", *European Physical Journal D*, 55, 2009, pp. 509–518, URL `https://ui.adsabs.harvard.edu/#abs/2009EPJD...55..509D`.

[20] M. Ostrowski, "Mechanisms and sites of ultra high energy cosmic ray origin", *Astroparticle Physics*, 18, 2002, pp. 229–236, URL `https://ui.adsabs.harvard.edu/#abs/2002APh....18..229O`.

[21] Francis F. Chen, *Introduction to plasma physics and controlled fusion. Volume 1, Plasma physics*, Springer, 2nd edn., 1984, URL `http://gen.lib.rus.ec/book/index.php?md5=C163A7016424E61AD353A4C532D59174`.

[22] A. M. Hillas, "The Origin of Ultra-High-Energy Cosmic Rays", *Annual Review of Astronomy and Astrophys*, 22, 1984, pp. 425–444, URL `http://adsabs.harvard.edu/abs/1984ARA%26A..22..425H`.

[23] D J. Miller, "High Energy Astrophysics, 3rd edn., by Malcolm S. Longair", *Contemporary Physics*, 53, 2012, pp. 174–175.

[24] "IX. A dynamical theory of the electric and luminiferous medium.— Part III. relations with material media", *Philosophical Transactions of the Royal Society of London A: Mathematical, Physical and Engineering Sciences*, 190, 1897, pp. 205–300, URL `http://rsta.royalsocietypublishing.org/content/190/205`.

[25] G. R. Blumenthal and J. Gould, Robert, "Bremsstrahlung, Synchrotron Radiation, and Compton Scattering of High-Energy Electrons Traversing Dilute Gases", *Reviews of Modern Physics*, 42, 1970, pp. 237–270, URL `https://link.aps.org/doi/10.1103/RevModPhys.42.237`.

[26] H. Bethe and W. Heitler, "On the Stopping of Fast Particles and on the Creation of Positive Electrons", *Proceedings of the Royal Society of London Series A*, 146, 1934, pp. 83–112, URL `http://adsabs.harvard.edu/abs/1934RSPSA.146...83B`.

[27] H. W. Koch and J. W. Motz, "Bremsstrahlung Cross-Section Formulas and Related Data", *Reviews of Modern Physics*, 31, 1959, pp. 920–955, URL `http://adsabs.harvard.edu/abs/1959RvMP...31..920K`.

[28] Arthur H. Compton, "A Quantum Theory of the Scattering of X-rays by Light Elements", *Physical Review*, 21, 1923, pp. 483–502, URL https://link.aps.org/doi/10.1103/PhysRev.21.483.

[29] John D. Jackson, *Classical Electrodynamics*, Wiley, 1999, URL http://www.worldcat.org/isbn/9780471309321.

[30] O. Klein and Y. Nishina, "Über die Streuung von Strahlung durch freie Elektronen nach der neuen relativistischen Quantendynamik von Dirac", *Zeitschrift für Physik*, 52(11), 1929, pp. 853–868, URL https://doi.org/10.1007/BF01366453.

[31] Gabriele Ghisellini, *Radiative Processes in High Energy Astrophysics*, 2013.

[32] E. Kundu and N. Gupta, "Possible proton synchrotron origin of X-ray and gamma-ray emission in large-scale jet of 3C 273.", *Monthly Notices of the Royal Astronomical Society*, 444, 2014, pp. L16–L19, URL https://ui.adsabs.harvard.edu/#abs/2014MNRAS.444L..16K.

[33] K. Mannheim, "The Proton blazar", *Astronomy and Astrophysics*, 269, 1993, p. 67, URL https://arxiv.org/abs/astro-ph/9302006.

[34] K. Mannheim and P. L. Biermann, "Gamma-ray flaring of 3C 279 - A proton-initiated cascade in the jet?", *Astronomy and Astrophysics*, 253, 1992, pp. L21–L24, URL http://adsabs.harvard.edu/abs/1992A&A...253L..21M.

[35] J. Beringer et al., "Review of Particle Physics (RPP)", *Physical Review*, D86, 2012, p. 010001, URL https://journals.aps.org/prd/abstract/10.1103/PhysRevD.86.010001.

[36] J. A. Hinton and W. Hofmann, "Teraelectronvolt Astronomy", *Annual Review of Astronomy and Astrophysics*, 47, 2009, pp. 523–565, URL https://ui.adsabs.harvard.edu/#abs/2009ARA&A..47..523H.

[37] Arnon Dar and Ari Laor, "Hadronic Production of TeV Gamma-Ray Flares from Blazars", *The Astrophysical Journal Letters*, 478(1), 1997, p. L5, URL http://stacks.iop.org/1538-4357/478/i=1/a=L5.

[38] M. Ackermann, et al., "Detection of the Characteristic Pion-Decay Signature in Supernova Remnants", *Science*, 339, 2013, pp. 807–811, URL https://ui.adsabs.harvard.edu/#abs/2013Sci...339..807A.

[39] ENRICO Fermi, "On the Origin of the Cosmic Radiation", *Physical Review*, 75, 1949, pp. 1169–1174, URL https://link.aps.org/doi/10.1103/PhysRev.75.1169.

[40] Malcolm S. Longair, "High Energy Astrophysics, 3rd edn.", *Contemporary Physics*, 53, 2012, pp. 174–175, URL https://www.researchgate.net/publication/254224630_High_Energy_Astrophysics_3rd_edn_by_Malcolm_S_Longair.

[41] W. I. Axford, et al., "The acceleration of cosmic rays by shock waves", *International Cosmic Ray Conference*, 11, 1977, pp. 132–137, URL http://adsabs.harvard.edu/abs/1977ICRC...11..132A.

[42] A. R. Bell, "The acceleration of cosmic rays in shock fronts. II", *Monthly Notices of the Royal Astronomical Society*, 182, 1978, pp. 443–455, URL http://adsabs.harvard.edu/abs/1978MNRAS.182..443B.

[43] R. D. Blandford and J. P. Ostriker, "Particle acceleration by astrophysical shocks", *The Astrophysical Journal Letters*, 221, 1978, pp. L29–L32, URL http://adsabs.harvard.edu/abs/1978ApJ...221L..29B.

[44] G Krymsky, "A regular mechanism for the acceleration of charged particles on the front of a shock wave", *Akademiia Nauk SSSR Doklady*, 234, 1977, pp. 1306–1308.

[45] L. D. Landau and E. M. Lifshitz, *Fluid Mechanics, Second Edition: Volume 6 (Course of Theoretical Physics)*, Course of theoretical physics / by L. D. Landau and E. M. Lifshitz, Vol. 6, Butterworth-Heinemann, 2nd edn., 1987, URL http://www.worldcat.org/isbn/0750627670.

[46] Mireia Nievas Rosillo, "Observations of VHE emission from Blazars at Cosmological Distances", , 2018, URL https://eprints.ucm.es/50912/.

[47] Markus Boettcher, "Models for the Spectral Energy Distributions and Variability of Blazars", *ArXiv e-prints*, 2010, p. arXiv:1006.5048, URL https://ui.adsabs.harvard.edu/#abs/2010arXiv1006.5048B.

[48] M A Malkov and L O'C Drury, "Nonlinear theory of diffusive acceleration of particles by shock waves", *Reports on Progress in Physics*, 64(4), 2001, p. 429, URL http://stacks.iop.org/0034-4885/64/i=4/a=201.

[49] Hyesung Kang and T. W. Jones, "Efficiency of Nonlinear Particle Acceleration at Cosmic Structure Shocks", *The Astrophysical Journal*, 620(1), 2005, p. 44, URL http://stacks.iop.org/0004-637X/620/i=1/a=44.

[50] A. Balogh and R.A. Treumann, *Physics of Collisionless Shocks: Space Plasma Shock Waves*, ISSI Scientific Report Series, Springer New York, 2013, URL https://books.google.de/books?id=mR4_AAAAQBAJ.

[51] Ellen G Zweibel and Masaaki Yamada, "Magnetic Reconnection in Astrophysical and Laboratory Plasmas", , 2009.

[52] R. G. Giovanelli, "A Theory of Chromospheric Flares", *Nature*, 158, 1946, pp. 81–82, URL http://adsabs.harvard.edu/abs/1946Natur.158...81G.

[53] E. N. Parker, "Sweet's Mechanism for Merging Magnetic Fields in Conducting Fluids", *Journal of Geophysics Research*, 62, 1957, pp. 509–520, URL http://adsabs.harvard.edu/abs/1957JGR....62..509P.

[54] P. A. Sweet, "The Neutral Point Theory of Solar Flares", in *Electromagnetic Phenomena in Cosmical Physics*, edited by B. Lehnert, 1958, vol. 6 of *IAU Symposium*, p. 123, URL http://adsabs.harvard.edu/abs/1958IAUS....6..123S.

[55] Hannes Alfvén, "Existence of Electromagnetic-Hydrodynamic Waves", *Nature*, 150(3805), 1942, pp. 405–406, URL http://www.nature.com/doifinder/10.1038/150405a0.

[56] D. Kagan, et al., "Relativistic Magnetic Reconnection in Pair Plasmas and Its Astrophysical Applications", *Space Science Reviews*, 191(1), 2015, pp. 545–573, URL https://doi.org/10.1007/s11214-014-0132-9.

[57] Lorenzo Sironi and Anatoly Spitkovsky, "Relativistic Reconnection: An Efficient Source of Non-thermal Particles", *The Astrophysical Journal Letters*, 783(1), 2014, p. L21, URL http://stacks.iop.org/2041-8205/783/i=1/a=L21.

[58] M. Oka, et al., "Island surfing mechanism of electron acceleration during magnetic reconnection", *Journal of Geophysical Research (Space Physics)*, 115, 2010, p. A08223, URL http://adsabs.harvard.edu/abs/2010JGRA..115.8223O.

[59] M. Ackermann, et al., "Fermi-LAT Observations of the Diffuse Gamma-Ray Emission: Implications for Cosmic Rays and the Interstellar Medium", *The Astrophysical Journal*, 750, 2012, p. 3, URL http://adsabs.harvard.edu/abs/2012ApJ...750....3A.

[60] Andrew M. Taylor and Gwenael Giacinti, "Cosmic rays in a galactic breeze", *Physical Review D*, 95, 2017, p. 023001, URL https://link.aps.org/doi/10.1103/PhysRevD.95.023001.

[61] T. Gold, "Rotating Neutron Stars and the Nature of Pulsars", *Nature*, 221, 1969, pp. 25–27, URL http://adsabs.harvard.edu/abs/1969Natur.221...25G.

[62] F PACINI, "Energy Emission from a Neutron Star", *Nature*, 216, 1967, pp. 567–568.

[63] Bryan M. Gaensler and Patrick O. Slane, "The Evolution and Structure of Pulsar Wind Nebulae", *Annual Review of Astronomy and Astrophysics*, 44, 2006, pp. 17–47, URL https://ui.adsabs.harvard.edu/#abs/2006ARA&A..44...17G.

[64] J Jeff Hester, "The Crab Nebula: An Astrophysical Chimera", *Annual Review of Astronomy and Astrophysics*, 46, 2008, pp. 127–155.

[65] Adam Burrows, "Supernova explosions in the Universe", *Nature*, 403, 2000, pp. 727–33.

[66] A. Heger, et al., "How Massive Single Stars End Their Life", *The Astrophysical Journal*, 591, 2003, pp. 288–300, URL https://ui.adsabs.harvard.edu/#abs/2003ApJ...591..288H.

[67] F. Acero, et al., "Fermi Large Area Telescope Third Source Catalog", *Astrophysical Journal, Supplement*, 218, 2015, p. 23, URL http://adsabs.harvard.edu/abs/2015ApJS..218...23A.

[68] Guillaume Dubus, "Gamma-ray emission from binaries in context", *Comptes Rendus Physique*, 16, 2015, pp. 661–673, URL https://ui.adsabs.harvard.edu/#abs/2015CRPhy..16..661D.

[69] R. H. D. Corbet, et al., "A Luminous Gamma-ray Binary in the Large Magellanic Cloud", *The Astrophysical Journal*, 829, 2016, p. 105, URL http://adsabs.harvard.edu/abs/2016ApJ...829..105C.

[70] G. A. Caliandro, et al., "The missing GeV γ-ray binary: searching for HESS J0632+057 with Fermi-LAT", *Monthly Notices of the Royal Astronomical Society*, 436, 2013, pp. 740–749, URL http://adsabs.harvard.edu/abs/2013MNRAS.436..740C.

[71] Arash Bodaghee, et al., "Gamma-Ray Observations of the Microquasars Cygnus X-1, Cygnus X-3, GRS 1915+105, and GX 339-4 with the Fermi Large Area Telescope", *The Astrophysical Journal*, 775, 2013, p. 98, URL https://ui.adsabs.harvard.edu/#abs/2013ApJ...775...98B.

[72] M. Ackermann, et al., "Fermi establishes classical novae as a distinct class of gamma-ray sources", *Science*, 345, 2014, pp. 554–558, URL https://ui.adsabs.harvard.edu/#abs/2014Sci...345..554A.

[73] A. A. Abdo, et al., "Gamma-Ray Emission Concurrent with the Nova in the Symbiotic Binary V407 Cygni", *Science*, 329, 2010, pp. 817–821, URL https://ui.adsabs.harvard.edu/#abs/2010Sci...329..817A.

[74] A. M. Ghez, et al., "Measuring Distance and Properties of the Milky Way's Central Supermassive Black Hole with Stellar Orbits", *The Astrophysical Journal*, 689, 2008, pp. 1044–1062, URL https://ui.adsabs.harvard.edu/#abs/2008ApJ...689.1044G.

[75] Christopher van Eldik, "Gamma rays from the Galactic Centre region: A review", *Astroparticle Physics*, 71, 2015, pp. 45–70, URL https://ui.adsabs.harvard.edu/#abs/2015APh....71...45V.

[76] M. Ackermann, et al., "The Fermi Galactic Center GeV Excess and Implications for Dark Matter", *The Astrophysical Journal*, 840, 2017, p. 43, URL https://ui.adsabs.harvard.edu/#abs/2017ApJ...840...43A.

[77] M. Ackermann, et al., "The Third Catalog of Active Galactic Nuclei Detected by the Fermi Large Area Telescope", *The Astrophysical Journal*, 810, 2015, p. 14, URL https://ui.adsabs.harvard.edu/#abs/2015ApJ...810...14A.

[78] Stefan Ohm, "Starburst galaxies as seen by gamma-ray telescopes", *Comptes Rendus Physique*, 17, 2016, pp. 585–593, URL https://ui.adsabs.harvard.edu/#abs/2016CRPhy..17..585O.

[79] A. A. Abdo, et al., "Detection of Gamma-Ray Emission from the Starburst Galaxies M82 and NGC 253 with the Large Area Telescope on Fermi", *The Astrophysical Journal Letters*, 709(2), 2010, p. L152, URL http://stacks.iop.org/2041-8205/709/i=2/a=L152.

[80] F. Acero, et al., "Detection of Gamma Rays from a Starburst Galaxy", *Science*, 326, 2009, p. 1080, URL https://ui.adsabs.harvard.edu/#abs/2009Sci...326.1080A.

[81] VERITAS Collaboration, et al., "A connection between star formation activity and cosmic rays in the starburst galaxy M82", *Nature*, 462, 2009, pp. 770–772, URL https://ui.adsabs.harvard.edu/#abs/2009Natur.462..770V.

[82] P. Mészáros, "Gamma ray bursts", *Astroparticle Physics*, 43, 2013, pp. 134–141, URL http://adsabs.harvard.edu/abs/2013APh....43..134M.

[83] Frédéric Piron, "Gamma-ray bursts at high and very high energies", *Comptes Rendus Physique*, 17, 2016, pp. 617–631, URL https://ui.adsabs.harvard.edu/#abs/2016CRPhy..17..617P.

[84] C. Tadhunter, "An introduction to active galactic nuclei: Classification and unification", *New Astronomy Review*, 52, 2008, pp. 227–239, URL http://adsabs.harvard.edu/abs/2008NewAR..52..227T.

[85] E. A. Fath, "The Spectra of Some Spiral Nebulæ and Globular Star Clusters", *Publications of the ASP*, 21, 1909, pp. 138–143, URL http://adsabs.harvard.edu/abs/1909PASP...21..138F.

[86] D. E. Osterbrock, "Seyfert Galaxies", *The Astrophysical Journal*, 525, 1999, p. 337, URL http://adsabs.harvard.edu/abs/1999ApJ...525C.337O.

[87] M. Schmidt, "3C 273 : A Star-Like Object with Large Red-Shift", *Nature*, 197, 1963, p. 1040, URL http://adsabs.harvard.edu/abs/1963Natur.197.1040S.

[88] P. Martini, et al., "The Cluster and Field Galaxy Active Galactic Nucleus Fraction at z = 1-1.5: Evidence for a Reversal of the Local Anticorrelation between

Environment and AGN Fraction", *The Astrophysical Journal*, 768, 2013, p. 1, URL http://adsabs.harvard.edu/abs/2013ApJ...768....1M.

[89] Henric Krawczynski and Ezequiel Treister, "Active galactic nuclei — the physics of individual sources and the cosmic history of formation and evolution", *Frontiers of Physics*, 8, 2013, pp. 609–629, URL https://ui.adsabs.harvard.edu/#abs/2013FrPhy...8..609K.

[90] J. E. Barnes and L. E. Hernquist, "Fueling starburst galaxies with gas-rich mergers", *The Astrophysical Journal Letters*, 370, 1991, pp. L65–L68, URL http://adsabs.harvard.edu/abs/1991ApJ...370L..65B.

[91] John Kormendy and Luis C. Ho, "Coevolution (Or Not) of Supermassive Black Holes and Host Galaxies", *Annual Review of Astronomy and Astrophys*, 51(1), 2013, pp. 511–653.

[92] P. Ghosh, "Accretion Disks in Quasars and Active Galactic Nuclei", *Journal of Astrophysics and Astronomy Supplement*, 16, 1995, p. 171, URL http://adsabs.harvard.edu/abs/1995JApAS..16..171G.

[93] F. Haardt and L. Maraschi, "X-ray spectra from two-phase accretion disks", *The Astrophysical Journal*, 413, 1993, pp. 507–517, URL http://adsabs.harvard.edu/abs/1993ApJ...413..507H.

[94] Moshe Elitzur and Isaac Shlosman, "The AGN Obscuring Torus: End of the Doughnut Paradigm?", *The Astrophysical Journal*, 648, 2006, pp. L101–L104.

[95] P. Padovani, "Gamma-Ray Emitting AGN and Unified Schemes", in *Very High Energy Phenomena in the Universe; Moriond Workshop*, edited by Y. Giraud-Heraud and J. Tran Thanh van, 1997, p. 7, URL https://ui.adsabs.harvard.edu/#abs/1997vhep.conf....7P.

[96] B. L. Fanaroff and J. M. Riley, "The morphology of extragalactic radio sources of high and low luminosity", *Monthly Notices of the Royal Astronomical Society*, 167, 1974, pp. 31P–36P, URL http://adsabs.harvard.edu/abs/1974MNRAS.167P..31F.

[97] C. M. Urry and P. Padovani, "Unified Schemes for Radio-Loud Active Galactic Nuclei", *Publications of the ASP*, 107, 1995, p. 803, URL http://adsabs.harvard.edu/abs/1995PASP..107..803U.

[98] G. Ghisellini, et al., "The transition between BL Lac objects and flat spectrum radio quasars", *Monthly Notices of the Royal Astronomical Society*, 414(3), 2011, pp. 2674–2689, URL http://dx.doi.org/10.1111/j.1365-2966.2011.18578.x.

[99] G. Ghisellini, et al., "The Fermi blazar sequence", *Monthly Notices of the Royal Astronomical Society*, 469, 2017, pp. 255–266, URL https://ui.adsabs.harvard.edu/#abs/2017MNRAS.469..255G.

[100] Matthias Weidinger and Felix Spanier, "Particle acceleration in Blazars", , 2011, vol. 274, pp. 263–266.

[101] Tiffany R. Lewis, et al., "Electron Acceleration in Blazars: Application to the 3C 279 Flare on 2013 December 20", *The Astrophysical Journal*, 884(2), 2019, p. 116.

[102] T. Savolainen, et al., "Relativistic beaming and gamma-ray brightness of blazars", *Astronomy and Astrophysicsl*, 512, 2010, p. A24, URL https://ui.adsabs.harvard.edu/#abs/2010A&A...512A..24S.

[103] M. J. Rees, "Appearance of Relativistically Expanding Radio Sources", *Nature*, 211, 1966, pp. 468–470, URL http://adsabs.harvard.edu/abs/1966Natur.211..468R.

[104] G. Ghisellini, et al., "Relativistic bulk motion in active galactic nuclei", *The Astrophysical Journal*, 407, 1993, pp. 65–82, URL http://adsabs.harvard.edu/abs/1993ApJ...407...65G.

[105] D. A. Kniffen, et al., "Time variability in the gamma-ray emission of 3C 279", *The Astrophysical Journal*, 411, 1993, pp. 133–136, URL http://adsabs.harvard.edu/abs/1993ApJ...411..133K.

[106] R. C. Hartman, "Gamma-ray Variability in Blazars", in *Blazar Continuum Variability*, edited by H. R. Miller, et al., 1996, vol. 110 of *Astronomical Society of the Pacific Conference Series*, p. 333, URL http://adsabs.harvard.edu/abs/1996ASPC..110..333H.

[107] MARTIN J. REES, "Relativistic jets and beams in radio galaxies", *Nature*, 275, 1978, pp. 516–517, URL https://www.nature.com/articles/275516a0.

[108] L. Maraschi, et al., "A jet model for the gamma-ray emitting blazar 3C 279", *The Astrophysical Journal Letters*, 397, 1992, pp. L5–L9, URL http://adsabs.harvard.edu/abs/1992ApJ...397L...5M.

[109] C. D. Dermer and G. Menon, *High Energy Radiation from Black Holes: Gamma Rays, Cosmic Rays, and Neutrinos*, 2009, URL http://adsabs.harvard.edu/abs/2009herb.book.....D.

[110] L. Dondi and G. Ghisellini, "Gamma-ray-loud blazars and beaming", *Monthly Notices of the Royal Astronomical Society*, 273, 1995, pp. 583–595, URL http://adsabs.harvard.edu/abs/1995MNRAS.273..583D.

[111] Jörg P. Rachen, "Hadronic blazar models and correlated X-ray/TeV flares", in *American Institute of Physics Conference Series*, edited by Brenda L. Dingus, et al., 2000, vol. 515 of *American Institute of Physics Conference Series*, pp. 41–52, URL https://ui.adsabs.harvard.edu/#abs/2000AIPC..515...41R.

[112] A Reimer, "On the Physics of Hadronic Blazar Emission Models", *Journal of Physics: Conference Series*, 355(1), 2012, p. 012011, URL http://stacks.iop.org/1742-6596/355/i=1/a=012011.

[113] Steven Bloom and Alan P. Marscher, "An Analysis of the Synchrotron Self-Compton Model for the Multi–Wave Band Spectra of Blazars", *The Astrophysical Journal*, 461, 1996, p. 657.

[114] C. D. Dermer, et al., "High-energy gamma radiation from extragalactic radio sources", *Astronomy and Astrophysicsl*, 256, 1992, pp. L27–L30, URL http://adsabs.harvard.edu/abs/1992A%26A...256L..27D.

[115] M. Sikora, et al., "Comptonization of diffuse ambient radiation by a relativistic jet: The source of gamma rays from blazars?", *The Astrophysical Journal*, 421, 1994, pp. 153–162, URL http://adsabs.harvard.edu/abs/1994ApJ...421..153S.

[116] G. Ghisellini and P. Madau, "On the origin of the gamma-ray emission in blazars", *Monthly Notices of the Royal Astronomical Society*, 280, 1996, pp. 67–76, URL http://adsabs.harvard.edu/abs/1996MNRAS.280...67G.

[117] M. Błażejowski, et al., "Comptonization of Infrared Radiation from Hot Dust by Relativistic Jets in Quasars", *The Astrophysical Journal*, 545, 2000, pp. 107–116, URL https://ui.adsabs.harvard.edu/#abs/2000ApJ...545..107B.

[118] V. Zabalza, "Naima: a Python package for inference of particle distribution properties from nonthermal spectra", in *34th International Cosmic Ray Conference (ICRC2015)*, 2015, vol. 34, p. 922, URL https://ui.adsabs.harvard.edu/#abs/2015ICRC...34..922Z.

[119] G. Fossati, et al., "A unifying view of the spectral energy distributions of blazars", *Monthly Notices of the Royal Astronomical Society*, 299, 1998, pp. 433–448, URL http://adsabs.harvard.edu/abs/1998MNRAS.299..433F.

[120] D. Donato, et al., "Hard X-ray properties of blazars", *Astronomy and Astrophysicsl*, 375, 2001, pp. 739–751, URL http://adsabs.harvard.edu/abs/2001A%26A...375..739D.

[121] Gabriele Ghisellini, "Extragalactic relativistic jets", in *American Institute of Physics Conference Series*, edited by Felix A. Aharonian, et al., 2011, vol. 1381 of *American Institute of Physics Conference Series*, pp. 180–198, URL https://ui.adsabs.harvard.edu/#abs/2011AIPC.1381..180G.

[122] G. Ghisellini, et al., "High-redshift Fermi blazars", *Monthly Notices of the Royal Astronomical Society*, 411, 2011, pp. 901–914, URL https://ui.adsabs.harvard.edu/#abs/2011MNRAS.411..901G.

[123] R. A. Sunyaev and J. Chluba, "Signals from the epoch of cosmological recombination (Karl Schwarzschild Award Lecture 2008)", *Astronomische Nachrichten*, 330, 2009, p. 657, URL https://ui.adsabs.harvard.edu/#abs/2009AN....330..657S.

[124] J. Biteau and D. A. Williams, "The Extragalactic Background Light, the Hubble Constant, and Anomalies: Conclusions from 20 Years of TeV Gamma-ray Observations", *The Astrophysical Journal*, 812, 2015, p. 60, URL https://ui.adsabs.harvard.edu/#abs/2015ApJ...812...60B.

[125] Eli Dwek and Frank Krennrich, "The extragalactic background light and the gamma-ray opacity of the universe", *Astroparticle Physics*, 43, 2013, pp. 112–133, URL https://ui.adsabs.harvard.edu/#abs/2013APh....43..112D.

[126] T.K. Gaisser, *Cosmic Rays and Particle Physics*, Cambridge University Press, 1990, URL https://books.google.de/books?id=qJ7Z6oIMqeUC.

[127] P. A. Čerenkov, "Visible Radiation Produced by Electrons Moving in a Medium with Velocities Exceeding that of Light", *Physical Review*, 52, 1937, pp. 378–379, URL https://link.aps.org/doi/10.1103/PhysRev.52.378.

[128] P. Murdin, *Encyclopedia of Astronomy & Astrophysics*, Taylor & Francis, 2001, URL https://books.google.de/books?id=W8zLQgAACAAJ.

[129] T. C. Weekes, *Very high energy gamma-ray astronomy*, 2003, URL http://adsabs.harvard.edu/abs/2003vheg.book.....W.

[130] Robert J. Gould and Gérard P. Schréder, "Pair Production in Photon-Photon Collisions", *Physical Review*, 155, 1967, pp. 1404–1407, URL https://link.aps.org/doi/10.1103/PhysRev.155.1404.

[131] H. Mo, et al., *Galaxy Formation and Evolution*, 2010, URL http://adsabs.harvard.edu/abs/2010gfe..book.....M.

[132] M. Tanabashi, et al., "Review of Particle Physics", *Physical Review D*, 98, 2018, p. 030001, URL https://link.aps.org/doi/10.1103/PhysRevD.98.030001.

[133] H. Dole, et al., "The cosmic infrared background resolved by Spitzer. Contributions of mid-infrared galaxies to the far-infrared background", *Astronomy and Astrophysicsl*, 451, 2006, pp. 417–429, URL https://ui.adsabs.harvard.edu/#abs/2006A&A...451..417D.

[134] G. Rodighiero, et al., "Mid- and far-infrared luminosity functions and galaxy evolution from multiwavelength Spitzer observations up to z ˜ 2.5", *Astronomy and Astrophysicsl*, 515, 2010, p. A8, URL http://adsabs.harvard.edu/abs/2010A%26A...515A...8R.

[135] Michael G. Hauser and Eli Dwek, "The Cosmic Infrared Background: Measurements and Implications", *Annual Review of Astronomy and Astrophysics*, 39, 2001, pp. 249–307, URL https://ui.adsabs.harvard.edu/#abs/2001ARA&A..39..249H.

[136] W. L. Freedman, et al., "BVRI photometry of extragalactic cepheids and new insights for the distance scale", *Astrophysical Journal, Supplement*, 59, 1985, pp. 311–321, URL http://adsabs.harvard.edu/abs/1985ApJS...59..311F.

[137] L. R. Levenson and E. L. Wright, "Probing the 3.6 μm CIRB with Spitzer in Three DIRBE Dark Spots", *The Astrophysical Journal*, 683, 2008, pp. 585–596, URL `https://ui.adsabs.harvard.edu/#abs/2008ApJ...683..585L`.

[138] H. E. S. S. Collaboration, et al., "Measurement of the EBL spectral energy distribution using the VHE γ-ray spectra of H.E.S.S. blazars", *Astronomy and Astrophysicsl*, 606, 2017, p. A59, URL `https://ui.adsabs.harvard.edu/#abs/2017A&A...606A..59H`.

[139] F. W. Stecker, et al., "Intergalactic Photon Spectra from the Far-IR to the UV Lyman Limit for $0 < z < 6$ and the Optical Depth of the Universe to High-Energy Gamma Rays", *The Astrophysical Journal*, 648, 2006, pp. 774–783, URL `http://adsabs.harvard.edu/abs/2006ApJ...648..774S`.

[140] A. Franceschini, et al., "Extragalactic optical-infrared background radiation, its time evolution and the cosmic photon-photon opacity", *Astronomy and Astrophysicsl*, 487, 2008, pp. 837–852, URL `http://adsabs.harvard.edu/abs/2008A%26A...487..837F`.

[141] Kari Helgason and Alexander Kashlinsky, "Reconstructing the γ-Ray Photon Optical Depth of the Universe to z ~4 from Multiwavelength Galaxy Survey Data", *The Astrophysical Journal*, 758, 2012, p. L13, URL `https://ui.adsabs.harvard.edu/#abs/2012ApJ...758L..13H`.

[142] P. Madau, et al., "High-redshift galaxies in the Hubble Deep Field: colour selection and star formation history to z˜4", *Monthly Notices of the Royal Astronomical Society*, 283, 1996, pp. 1388–1404, URL `http://adsabs.harvard.edu/abs/1996MNRAS.283.1388M`.

[143] J. D. Finke, et al., "Modeling the Extragalactic Background Light from Stars and Dust", *The Astrophysical Journal*, 712, 2010, pp. 238–249, URL `http://adsabs.harvard.edu/abs/2010ApJ...712..238F`.

[144] Joel R. Primack, et al., "Extragalactic Background Light and Gamma-Ray Attenuation", in *American Institute of Physics Conference Series*, edited by Felix A. Aharonian, et al., 2011, vol. 1381 of *American Institute of Physics Conference Series*, pp. 72–83, URL `https://ui.adsabs.harvard.edu/#abs/2011AIPC.1381...72P`.

[145] The Fermi-LAT Collaboration. Contact Authors, et al., "A gamma-ray determination of the Universe's star- formation history", *ArXiv e-prints*, 2018, p. arXiv:1812.01031, URL https://ui.adsabs.harvard.edu/#abs/2018arXiv181201031A.

[146] Y. C. Pei and S. M. Fall, "Cosmic Chemical Evolution", *The Astrophysical Journal*, 454, 1995, p. 69, URL http://adsabs.harvard.edu/abs/1995ApJ...454...69P.

[147] G. Hinshaw, et al., "Five-Year Wilkinson Microwave Anisotropy Probe Observations: Data Processing, Sky Maps, and Basic Results", *Astrophysical Journal, Supplement*, 180, 2009, pp. 225–245, URL http://adsabs.harvard.edu/abs/2009ApJS..180..225H.

[148] Rudy C. Gilmore, et al., "Semi-analytic modelling of the extragalactic background light and consequences for extragalactic gamma-ray spectra", *Monthly Notices of the Royal Astronomical Society*, 422(4), 2012, pp. 3189–3207, URL http://dx.doi.org/10.1111/j.1365-2966.2012.20841.x.

[149] Yoshiyuki Inoue, et al., "Extragalactic Background Light from Hierarchical Galaxy Formation: Gamma-Ray Attenuation up to the Epoch of Cosmic Reionization and the First Stars", *The Astrophysical Journal*, 768, 2013, p. 197, URL https://ui.adsabs.harvard.edu/#abs/2013ApJ...768..197I.

[150] A. Domínguez, et al., "Extragalactic background light inferred from AEGIS galaxy-SED-type fractions", *Monthly Notices of the Royal Astronomical Society*, 410, 2011, pp. 2556–2578, URL https://ui.adsabs.harvard.edu/#abs/2011MNRAS.410.2556D.

[151] V. Schoenfelder, et al., "Instrument description and performance of the Imaging Gamma-Ray Telescope COMPTEL aboard the Compton Gamma-Ray Observatory", *Astrophysical Journal, Supplement*, 86, 1993, pp. 657–692, URL http://adsabs.harvard.edu/abs/1993ApJS...86..657S.

[152] A. A. Moiseev, et al., "Compton-Pair Production Space Telescope (ComPair) for MeV Gamma-ray Astronomy", *arXiv e-prints*, 2015, p. arXiv:1508.07349, URL https://ui.adsabs.harvard.edu/#abs/2015arXiv150807349M.

[153] A. De Angelis, et al., "The e-ASTROGAM mission. Exploring the extreme Universe with gamma rays in the MeV - GeV range", *Experimental Astronomy*, 44, 2017, pp. 25–82, URL https://ui.adsabs.harvard.edu/#abs/2017ExA...44...25D.

[154] Carlotta Pittori and Marco Tavani, "Scientific Goals and Instrument Performance of the Gamma-Ray Imaging Detector AGILE", *Nuclear Physics B - Proceedings Supplements*, 134, 2004, pp. 72 – 74, URL http://www.sciencedirect.com/science/article/pii/S0920563204003007, proceedings of the Second International Conference on Particle and Fundamental Physics in Space (SpacePart '03).

[155] W. B. Atwood, et al., "The Large Area Telescope on the Fermi Gamma-Ray Space Telescope Mission", *The Astrophysical Journal*, 697, 2009, pp. 1071–1102, URL http://adsabs.harvard.edu/abs/2009ApJ...697.1071A.

[156] J. Beringer, et al., "Review of Particle Physics", *Physical Review D*, 86, 2012, p. 010001, URL https://link.aps.org/doi/10.1103/PhysRevD.86.010001.

[157] Ralph Engel, et al., "Extensive Air Showers and Hadronic Interactions at High Energy", *Annual Review of Nuclear and Particle Science*, 61(1), 2011, pp. 467–489, URL https://doi.org/10.1146/annurev.nucl.012809.104544.

[158] E. Rutherford F.R.S., "The scattering of alpha and beta particles by matter and the structure of the atom", *Philosophical Magazine*, 92(4), 2012, pp. 379–398, URL https://doi.org/10.1080/14786435.2011.617037.

[159] Charles Meegan, et al., "The Fermi Gamma-ray Burst Monitor", *The Astrophysical Journal*, 702, 2009, pp. 791–804, URL https://ui.adsabs.harvard.edu/#abs/2009ApJ...702..791M.

[160] Carlotta Pittori and Marco Tavani, "Scientific Goals and Instrument Performance of the Gamma-Ray Imaging Detector AGILE", *Nuclear Physics B - Proceedings Supplements*, 134, 2004, pp. 72 – 74, URL http://www.sciencedirect.com/science/article/pii/S0920563204003007, proceedings of the Second International Conference on Particle and Fundamental Physics in Space (SpacePart '03).

[161] J Bregeon, "Design and performance of the silicon strip tracker of the Fermi Large Area Telescope", *Journal of Instrumentation*, 6(12), 2011, p. C12043, URL http://stacks.iop.org/1748-0221/6/i=12/a=C12043.

[162] Christian W. Fabjan and Fabiola Gianotti, "Calorimetry for particle physics", *Reviews of Modern Physics*, 75, 2003, pp. 1243–1286, URL https://link.aps.org/doi/10.1103/RevModPhys.75.1243.

[163] A. A. Abdo, et al., "Fermi large area telescope observations of the cosmic-ray induced gamma-ray emission of the Earth's atmosphere", *Physical Review D*, 80, 2009, p. 122004, URL https://link.aps.org/doi/10.1103/PhysRevD.80.122004.

[164] A.A. Moiseev, et al., "Observation and simulations of the backsplash effects in high-energy gamma-ray telescopes containing a massive calorimeter", *Astroparticle Physics*, 22(3), 2004, pp. 275 – 283, URL http://www.sciencedirect.com/science/article/pii/S0927650504001318.

[165] M. Ackermann, et al., "The Fermi Large Area Telescope on Orbit: Event Classification, Instrument Response Functions, and Calibration", *The Astrophysical Journal Supplement Series*, 203, 2012, p. 4, URL https://ui.adsabs.harvard.edu/#abs/2012ApJS..203....4A.

[166] W. Atwood, et al., "Pass 8: Toward the Full Realization of the Fermi-LAT Scientific Potential", *arXiv e-prints*, 2013, p. arXiv:1303.3514, URL https://ui.adsabs.harvard.edu/#abs/2013arXiv1303.3514A.

[167] J. Asercion and Fermi Science Support Center Team, "Understanding and Using the Fermi Science Tools", in *American Astronomical Society Meeting Abstracts 227*, 2016, vol. 227 of *American Astronomical Society Meeting Abstracts*, p. 348.07, URL http://adsabs.harvard.edu/abs/2016AAS...22734807A.

[168] Bruno Rossi and Kenneth Greisen, "Cosmic-Ray Theory", *Reviews of Modern Physics*, 13, 1941, pp. 240–309, URL https://link.aps.org/doi/10.1103/RevModPhys.13.240.

[169] D. Heck, et al., *CORSIKA: a Monte Carlo code to simulate extensive air showers.*, 1998, URL http://adsabs.harvard.edu/abs/1998cmcc.book.....H.

[170] W. Hofmann, et al., "Comparison of techniques to reconstruct VHE gamma-ray showers from multiple stereoscopic Cherenkov images", *Astroparticle Physics*, 12, 1999, pp. 135–143, URL https://ui.adsabs.harvard.edu/#abs/1999APh....12..135H.

[171] Jamie Holder, "Atmospheric Cherenkov Gamma-ray Telescopes", *arXiv e-prints*, 2015, p. arXiv:1510.05675, URL https://ui.adsabs.harvard.edu/#abs/2015arXiv151005675H.

[172] Gennadi Sardanashvily, *Noether's theorems: applications in mechanics and field theory*, Atlantis studies in variational geometry, Springer, Paris, 2016, URL https://cds.cern.ch/record/2143630.

[173] Jean Iliopoulos, "Introduction to the STANDARD MODEL of the Electro-Weak Interactions", *arXiv e-prints*, 2013, p. arXiv:1305.6779, URL https://ui.adsabs.harvard.edu/#abs/2013arXiv1305.6779I.

[174] C. S. Wu, et al., "Experimental Test of Parity Conservation in Beta Decay", *Physical Review*, 105, 1957, pp. 1413–1415, URL https://link.aps.org/doi/10.1103/PhysRev.105.1413.

[175] J. H. Christenson, et al., "Evidence for the 2π Decay of the K_2^0 Meson", *Physical Review Letters*, 13, 1964, pp. 138–140, URL https://link.aps.org/doi/10.1103/PhysRevLett.13.138.

[176] Alan Kostelecky, "The Status of CPT", *arXiv e-prints*, 1998, pp. hep–ph/9810365, URL https://ui.adsabs.harvard.edu/#abs/1998hep.ph...10365K.

[177] Steven Weinberg, "The U(1) problem", *Physical Review D*, 11, 1975, pp. 3583–3593, URL https://link.aps.org/doi/10.1103/PhysRevD.11.3583.

[178] G. 't Hooft, "How instantons solve the U(1) problem", *Physics Reports*, 142(6), 1986, pp. 357 – 387, URL http://www.sciencedirect.com/science/article/pii/0370157386901171.

[179] R. D. Peccei, "QCD, strong CP and axions.", *Journal of Korean Physical Society*, 29, 1996, pp. S199–S208, URL https://ui.adsabs.harvard.edu/#abs/1996JKPS...29S.199P.

[180] Varouzhan Baluni, "CP-nonconserving effects in quantum chromodynamics", *Physical Review D*, 19, 1979, pp. 2227–2230, URL https://link.aps.org/doi/10.1103/PhysRevD.19.2227.

[181] R. D. Peccei and Helen R. Quinn, "CP Conservation in the Presence of Pseudoparticles", *Physical Review Letters*, 38, 1977, pp. 1440–1443, URL https://link.aps.org/doi/10.1103/PhysRevLett.38.1440.

[182] R.D. Peccei, et al., "A viable axion model", *Physics Letters B*, 172(3), 1986, pp. 435 – 440, URL http://www.sciencedirect.com/science/article/pii/0370269386902844.

[183] R. D. Peccei, "CP Violation: A Theoretical Review", *arXiv e-prints*, 1995, pp. hep–ph/9508389, URL https://ui.adsabs.harvard.edu/#abs/1995hep.ph....8389P.

[184] Jihn E. Kim, "Weak-Interaction Singlet and Strong CP Invariance", *Physical Review Letters*, 43, 1979, pp. 103–107, URL https://link.aps.org/doi/10.1103/PhysRevLett.43.103.

[185] Michael Dine, et al., "A simple solution to the strong CP problem with a harmless axion", *Physics Letters B*, 104(3), 1981, pp. 199 – 202, URL http://www.sciencedirect.com/science/article/pii/0370269381905906.

[186] A. R. Zhitnitsky, "On Possible Suppression of the Axion Hadron Interactions. (In Russian)", *Sov J Nucl Phys*, 31, 1980, p. 260, [Yad. Fiz.31,497(1980)].

[187] Joseph D. Lykken, "Beyond the Standard Model", *arXiv e-prints*, 2010, p. arXiv:1005.1676, URL https://ui.adsabs.harvard.edu/#abs/2010arXiv1005.1676L.

[188] Sanghyeon Chang, et al., "Axion model in extra dimensions with TeV scale gravity", *Physical Review*, D61, 2000, p. 084005.

[189] Neil Turok, "Almost Goldstone bosons from extra dimensional gauge theories", *Physical Review Letters*, 76, 1996, pp. 1015–1018.

[190] Peter Svrcek and Edward Witten, "Axions In String Theory", *Journal of High Energy Physics*, 06, 2006, p. 051.

[191] Claudio Coriano and Nikos Irges, "Windows over a New Low Energy Axion", *Physics Letters*, B651, 2007, pp. 298–305.

[192] Howard Baer, et al., "Cosmological consequences of Yukawa-unified SUSY with mixed axion/axino cold and warm dark matter", *Journal of Cosmology and Astroparticle Physics*, 0902, 2009, p. 002.

[193] Asimina Arvanitaki, et al., "String Axiverse", *Physical Review*, D81, 2010, p. 123530.

[194] Georg Raffelt and Leo Stodolsky, "Mixing of the Photon with Low Mass Particles", *Physical Review*, D37, 1988, p. 1237.

[195] Giorgio Galanti and Marco Roncadelli, "Behavior of axionlike particles in smoothed out domainlike magnetic fields", *Physical Review D*, 98, 2018, p. 043018, URL `https://ui.adsabs.harvard.edu/#abs/2018PhRvD..98d3018G`.

[196] Pierre Sikivie, "Axion Cosmology", *Lecture Notes in Physics*, 741, 2008, pp. 19–50, [,19(2006)].

[197] P. Sikivie, "Dark matter axions", *International Journal of Modern Physics*, A25, 2010, pp. 554–563.

[198] L.F. Abbott and P. Sikivie, "A cosmological bound on the invisible axion", *Physics Letters B*, 120(1), 1983, pp. 133 – 136, URL `http://www.sciencedirect.com/science/article/pii/037026938390638X`.

[199] Michael Dine and Willy Fischler, "The not-so-harmless axion", *Physics Letters B*, 120(1), 1983, pp. 137 – 141, URL `http://www.sciencedirect.com/science/article/pii/0370269383906391`.

[200] Sanghyeon Chang, et al., "Studies of the motion and decay of axion walls bounded by strings", *Physical Review*, D59, 1999, p. 023505.

[201] Nilanjan Banik and Pierre Sikivie, "Cosmic Axion Bose-Einstein Condensation", *arXiv e-prints*, 2015, p. arXiv:1501.05913, URL `https://ui.adsabs.harvard.edu/#abs/2015arXiv150105913B`.

[202] Gianpaolo Carosi and Karl van Bibber, "Microwave Cavity Searches", *Lecture Notes in Physics*, 741, 2008, pp. 135–156.

[203] Alessandro de Angelis, et al., "Relevance of axionlike particles for very-high-energy astrophysics", *Physical Review D*, 84, 2011, p. 105030, URL `https://ui.adsabs.harvard.edu/#abs/2011PhRvD..84j5030D`.

[204] Georg Raffelt and Leo Stodolsky, "Mixing of the Photon with Low Mass Particles", *Physical Review*, D37, 1988, p. 1237.

[205] G. G. Raffelt, *Stars as laboratories for fundamental physics*, 1996, URL `http://wwwth.mpp.mpg.de/members/raffelt/mypapers/199613.pdf`.

[206] W. Heisenberg and H. Euler, "Folgerungen aus der Diracschen Theorie des Positrons", *Z Phys*, 98, 1936, pp. 714–732.

[207] M. Ajello, et al., "Search for Spectral Irregularities due to Photon-Axionlike-Particle Oscillations with the Fermi Large Area Telescope", *Physical Review Letters*, 116, 2016, p. 161101, URL `https://ui.adsabs.harvard.edu/#abs/2016PhRvL.116p1101A`.

[208] F. Lei, et al., "Compton Polarimetry in Gamma-Ray Astronomy", *Space Science Reviews*, 82, 1997, pp. 309–388, URL `http://adsabs.harvard.edu/abs/1997SSRv...82..309L`.

[209] Matteo Giomi, et al., "Estimate of the Fermi large area telescope sensitivity to gamma-ray polarization", in *6th International Symposium on High Energy Gamma-Ray Astronomy*, 2017, vol. 1792 of *American Institute of Physics Conference Series*, p. 070022, URL `https://ui.adsabs.harvard.edu/#abs/2017AIPC.1792g0022G`.

[210] J. L. Hewett, et al., "Fundamental Physics at the Intensity Frontier", *arXiv e-prints*, 2012, p. arXiv:1205.2671, URL `https://ui.adsabs.harvard.edu/#abs/2012arXiv1205.2671H`.

[211] Peter W. Graham, et al., "Experimental Searches for the Axion and Axion-Like Particles", *Annual Review of Nuclear and Particle Science*, 65, 2015, pp. 485–514, URL `https://ui.adsabs.harvard.edu/#abs/2015ARNPS..65..485G`.

[212] Klaus Ehret, "The ALPS Light Shining Through a Wall Experiment - WISP Search in the Laboratory", *arXiv e-prints*, 2010, p. arXiv:1006.5741, URL `https://ui.adsabs.harvard.edu/#abs/2010arXiv1006.5741E`.

[213] Klaus Ehret, et al., "New ALPS results on hidden-sector lightweights", *Physics Letters B*, 689, 2010, pp. 149–155, URL `https://ui.adsabs.harvard.edu/#abs/2010PhLB..689..149E`.

[214] M. Bregant, et al., "Limits on low energy photon-photon scattering from an experiment on magnetic vacuum birefringence", *Physical Review D*, 78, 2008, p. 032006, URL https://link.aps.org/doi/10.1103/PhysRevD.78.032006.

[215] Koichi Hattori and Kazunori Itakura, "Vacuum birefringence in strong magnetic fields: (I) Photon polarization tensor with all the Landau levels", *Annals of Physics*, 330, 2013, pp. 23–54, URL https://ui.adsabs.harvard.edu/#abs/2013AnPhy.330...23H.

[216] RÃ©my Battesti, et al., "High magnetic fields for fundamental physics", *Physics Reports*, 2018.

[217] Babette Döbrich, "Axion-like Particles from Primakov production in beam-dumps", *arXiv e-prints*, 2017, p. arXiv:1708.05776, URL https://ui.adsabs.harvard.edu/#abs/2017arXiv170805776D.

[218] Sergey Alekhin, et al., "A facility to search for hidden particles at the CERN SPS: the SHiP physics case", *Reports on Progress in Physics*, 79, 2016, p. 124201, URL https://ui.adsabs.harvard.edu/#abs/2016RPPh...79l4201A.

[219] Davide Cadamuro and Javier Redondo, "Cosmological bounds on pseudo Nambu-Goldstone bosons", *Journal of Cosmology and Astro-Particle Physics*, 2012, 2012, p. 032, URL https://ui.adsabs.harvard.edu/#abs/2012JCAP...02..032C.

[220] Eduard Massó and Ramon Toldrà, "New constraints on a light spinless particle coupled to photons", *Physical Review D*, 55, 1997, pp. 7967–7969, URL https://ui.adsabs.harvard.edu/#abs/1997PhRvD..55.7967M.

[221] M. Ted Ressell, "Limits to the radiative decay of the axion", *Physical Review*, D44, 1991, pp. 3001–3020.

[222] Davide Cadamuro, *Cosmological limits on axions and axion-like particles*, Ph.D. thesis, Munich U., 2012.

[223] Georg G. Raffelt, *Astrophysical Axion Bounds*, 2008, p. 51, URL https://ui.adsabs.harvard.edu/#abs/2008LNP...741...51R.

[224] V. Anastassopoulos, et al., "New CAST limit on the axion-photon interaction", *Nature Physics*, 13, 2017, pp. 584–590, URL https://ui.adsabs.harvard.edu/#abs/2017NatPh..13..584A.

[225] J. K. Vogel, et al., "IAXO - The International Axion Observatory", *arXiv e-prints*, 2013, p. arXiv:1302.3273, URL https://ui.adsabs.harvard.edu/#abs/2013arXiv1302.3273V.

[226] P. Sikivie, "Experimental Tests of the "Invisible" Axion", *Physical Review Letters*, 51, 1983, pp. 1415–1417, URL https://link.aps.org/doi/10.1103/PhysRevLett.51.1415.

[227] J. Hoskins, et al., "Search for nonvirialized axionic dark matter", *Physical Review D*, 84, 2011, p. 121302, URL https://link.aps.org/doi/10.1103/PhysRevD.84.121302.

[228] S. J. Asztalos, et al., "SQUID-Based Microwave Cavity Search for Dark-Matter Axions", *Physical Review Letters*, 104, 2010, p. 041301, URL https://link.aps.org/doi/10.1103/PhysRevLett.104.041301.

[229] Gray Rybka, "Direct Detection Searches for Axion Dark Matter", *Physics of the Dark Universe*, 4, 2014, pp. 14–16.

[230] Georg G. Raffelt, *Astrophysical Axion Bounds*, 2008, p. 51, URL https://ui.adsabs.harvard.edu/#abs/2008LNP...741...51R.

[231] Georg G. Raffelt, "Astrophysical axion bounds diminished by screening effects", *Physical Review D*, 33, 1986, pp. 897–909, URL https://link.aps.org/doi/10.1103/PhysRevD.33.897.

[232] Paolo Gondolo and Georg G. Raffelt, "Solar neutrino limit on axions and keV-mass bosons", *Physical Review D*, 79, 2009, p. 107301, URL https://link.aps.org/doi/10.1103/PhysRevD.79.107301.

[233] M. Salaris and S. Cassisi, *Evolution of Stars and Stellar Populations*, 2005, URL http://adsabs.harvard.edu/abs/2005essp.book.....S.

[234] Adrian Ayala, et al., "Revisiting the Bound on Axion-Photon Coupling from Globular Clusters", *Physical Review Letters*, 113, 2014, p. 191302, URL https://ui.adsabs.harvard.edu/#abs/2014PhRvL.113s1302A.

[235] Georg Raffelt and Achim Weiss, "Red giant bound on the axion-electron coupling reexamined", *Physical Review D*, 51, 1995, pp. 1495–1498, URL https://ui.adsabs.harvard.edu/#abs/1995PhRvD..51.1495R.

[236] B. Melendez, et al., "Revisiting the Impact of Axions in the Cooling of White Dwarfs", in *18th European White Dwarf Workshop.*, edited by J. Krzesiński, et al., 2013, vol. 469 of *Astronomical Society of the Pacific Conference Series*, p. 189, URL `https://ui.adsabs.harvard.edu/#abs/2013ASPC..469..189M`.

[237] Georg G. Raffelt, "Axion Constraints From White Dwarf Cooling Times", *Physics Letters*, 166B, 1986, pp. 402–406.

[238] B. Berenji, et al., "Constraints on axions and axionlike particles from Fermi Large Area Telescope observations of neutron stars", *Physical Review D*, 93, 2016, p. 045019, URL `https://ui.adsabs.harvard.edu/#abs/2016PhRvD..93d5019B`.

[239] M. Koshiba, "Observational neutrino astrophysics", *Phys Rept*, 220, 1992, pp. 229–381.

[240] Alexandre Payez, et al., "Revisiting the SN1987A gamma-ray limit on ultralight axion-like particles", *Journal of Cosmology and Astro-Particle Physics*, 2015, 2015, p. 006, URL `https://ui.adsabs.harvard.edu/#abs/2015JCAP...02..006P`.

[241] M. Meyer, et al., "Fermi Large Area Telescope as a Galactic Supernovae Axionscope", *Physical Review Letters*, 118, 2017, p. 011103, URL `https://ui.adsabs.harvard.edu/#abs/2017PhRvL.118a1103M`.

[242] Ignazio Bombaci, et al., "No axion-like particles from core-collapse supernovae?", *arXiv e-prints*, 2017, p. arXiv:1712.06205, URL `https://ui.adsabs.harvard.edu/#abs/2017arXiv171206205B`.

[243] A. Domínguez, et al., "Axion-like particle imprint in cosmological very-high-energy sources", *Journal of Cosmology and Astro-Particle Physics*, 2011, 2011, p. 020, URL `https://ui.adsabs.harvard.edu/#abs/2011JCAP...11..020D`.

[244] Dieter Horns, et al., "Hardening of TeV gamma spectrum of active galactic nuclei in galaxy clusters by conversions of photons into axionlike particles", *Physical Review D*, 86, 2012, p. 075024, URL `https://ui.adsabs.harvard.edu/#abs/2012PhRvD..86g5024H`.

[245] Daniele Montanino, et al., "Enhancing the Spectral Hardening of Cosmic TeV Photons by Mixing with Axionlike Particles in the Magnetized Cosmic Web",

Physical Review Letters, 119, 2017, p. 101101, URL https://ui.adsabs.harvard.edu/#abs/2017PhRvL.119j1101M.

[246] M. A. Sánchez-Conde, et al., "Hints of the existence of axionlike particles from the gamma-ray spectra of cosmological sources", *Physical Review D*, 79(12), 2009, p. 123511, URL http://adsabs.harvard.edu/abs/2009PhRvD..79l3511S.

[247] Pierre Brun, et al., "Constraints on axion-like particles with H.E.S.S. from observations of PKS 2155-304", *arXiv e-prints*, 2013, p. arXiv:1307.6068, URL https://ui.adsabs.harvard.edu/#abs/2013arXiv1307.6068B.

[248] E. Aliu et al., "Very-High-Energy Gamma Rays from a Distant Quasar: How Transparent Is the Universe?", *Science*, 320(5884), 2008, p. 1752.

[249] F. Aharonian, et al., "A low level of extragalactic background light as revealed by γ-rays from blazars", *Nature*, 440, 2006, pp. 1018–1021, URL http://adsabs.harvard.edu/abs/2006Natur.440.1018A.

[250] Aharonian, F., et al., "New constraints on the mid-IR EBL from the HESS discovery of VHE s from 1ES9+200", *A&A*, 475(2), 2007, pp. L9–L13, URL https://doi.org/10.1051/0004-6361:20078462.

[251] Jacobus P. van den Berg, et al., "Systematic Physical Characterization of the Gamma-Ray Spectra of 2FHL Blazars", *arXiv e-prints*, 2019, p. arXiv:1901.03494, URL https://ui.adsabs.harvard.edu/#abs/2019arXiv190103494V.

[252] M. Ackermann, et al., "The Imprint of the Extragalactic Background Light in the Gamma-Ray Spectra of Blazars", *Science*, 338, 2012, p. 1190.

[253] M. Ackermann, et al., "The First Fermi-LAT Catalog of Sources above 10 GeV", *The Astrophysical Journal Supplement Series*, 209, 2013, p. 34, URL https://ui.adsabs.harvard.edu/#abs/2013ApJS..209...34A.

[254] M. Davis, et al., "The All-Wavelength Extended Groth Strip International Survey (AEGIS) Data Sets", *The Astrophysical Journal Letters*, 660, 2007, pp. L1–L6, URL http://adsabs.harvard.edu/abs/2007ApJ...660L...1D.

[255] M. Cirasuolo, et al., "A new measurement of the evolving near-infrared galaxy luminosity function out to z ˜= 4: a continuing challenge to theoretical models of

galaxy formation", *Monthly Notices of the Royal Astronomical Society*, 401, 2010, pp. 1166–1176, URL http://adsabs.harvard.edu/abs/2010MNRAS.401.1166C.

[256] E. N. Parker, *Cosmical magnetic fields: Their origin and their activity*, 1979, URL http://adsabs.harvard.edu/abs/1979cmft.book.....P.

[257] Lawrence M. Widrow, "Origin of galactic and extragalactic magnetic fields", *Reviews of Modern Physics*, 74, 2002, pp. 775–823, URL https://ui.adsabs.harvard.edu/#abs/2002RvMP...74..775W.

[258] P. P. Kronberg and J. J. Perry, "Absorption lines, Faraday rotation, and magnetic field estimates for QSO absorption-line clouds", *The Astrophysical Journal*, 263, 1982, pp. 518–532, URL http://adsabs.harvard.edu/abs/1982ApJ...263..518K.

[259] R D. DAVIES, et al., "Interstellar Magnetic Fields determined from Zeeman Effect Measurements", *Nature*, 220, 1968, pp. 1207–1210.

[260] A. Lazarian, et al., "On the Efficiency of Grain Alignment in Dark Clouds", *The Astrophysical Journal*, 490, 1997, pp. 273–280, URL https://ui.adsabs.harvard.edu/#abs/1997ApJ...490..273L.

[261] J.-F. Donati and J. D. Landstreet, "Magnetic Fields of Nondegenerate Stars", *Annual Review of Astronomy and Astrophys*, 47, 2009, pp. 333–370, URL http://adsabs.harvard.edu/abs/2009ARA%26A..47..333D.

[262] Rainer Beck, "Magnetic fields in spiral galaxies", *Astronomy and Astrophysics Review*, 24, 2015, p. 4, URL https://ui.adsabs.harvard.edu/#abs/2015A&ARv..24....4B.

[263] Ronnie Jansson and Glennys R. Farrar, "The Galactic Magnetic Field", *The Astrophysical Journal*, 761, 2012, p. L11, URL https://ui.adsabs.harvard.edu/#abs/2012ApJ...761L..11J.

[264] A. Neronov and D. V. Semikoz, "Sensitivity of γ-ray telescopes for detection of magnetic fields in the intergalactic medium", *Physical Review D*, 80, 2009, p. 123012, URL https://ui.adsabs.harvard.edu/#abs/2009PhRvD..80l3012N.

[265] L. Biermann, "Über den Ursprung der Magnetfelder auf Sternen und im interstellaren Raum (miteinem Anhang von A. Schlüter)", *Zeitschrift Naturforschung*

Teil A, 5, 1950, p. 65, URL http://adsabs.harvard.edu/abs/1950ZNatA...5...65B.

[266] D. Grasso and H. R. Rubinstein, "Magnetic fields in the early Universe", *Physics Reports*, 348, 2001, pp. 163–266, URL https://ui.adsabs.harvard.edu/#abs/2001PhR...348..163G.

[267] Ronnie Jansson and Glennys R. Farrar, "A New Model of the Galactic Magnetic Field", *The Astrophysical Journal*, 757, 2012, p. 14, URL https://ui.adsabs.harvard.edu/#abs/2012ApJ...757...14J.

[268] B. T. Draine, *Physics of the Interstellar and Intergalactic Medium*, 2011.

[269] P. P. Kronberg and M. Simard-Normandin, "New evidence on the origin of rotation measures in extragalactic radio sources", *Nature*, 263, 1976, pp. 653–656, URL http://adsabs.harvard.edu/abs/1976Natur.263..653K.

[270] Pasquale Blasi, et al., "Cosmological Magnetic Field Limits in an Inhomogeneous Universe", *The Astrophysical Journal*, 514, 1999, pp. L79–L82, URL https://ui.adsabs.harvard.edu/#abs/1999ApJ...514L..79B.

[271] Karsten Jedamzik, et al., "Limit on Primordial Small-Scale Magnetic Fields from Cosmic Microwave Background Distortions", *Physical Review Letters*, 85, 2000, pp. 700–703, URL https://ui.adsabs.harvard.edu/#abs/2000PhRvL..85..700J.

[272] John D. Barrow, et al., "Constraints on a Primordial Magnetic Field", *Physical Review Letters*, 78, 1997, pp. 3610–3613, URL https://ui.adsabs.harvard.edu/#abs/1997PhRvL..78.3610B.

[273] R. Durrer, et al., "Tensor microwave anisotropies from a stochastic magnetic field", *Physical Review D*, 61, 2000, p. 043001, URL https://ui.adsabs.harvard.edu/#abs/2000PhRvD..61d3001D.

[274] Tina Kahniashvili, et al., "Faraday rotation limits on a primordial magnetic field from Wilkinson Microwave Anisotropy Probe five-year data", *Physical Review D*, 80, 2009, p. 023009, URL https://ui.adsabs.harvard.edu/#abs/2009PhRvD..80b3009K.

[275] Sangjin Lee, et al., "Extragalactic Magnetic Field and the Highest Energy Cosmic Rays", *The Astrophysical Journal*, 455, 1995, p. L21, URL `https://ui.adsabs.harvard.edu/#abs/1995ApJ...455L..21L`.

[276] A. Neronov and I. Vovk, "Evidence for Strong Extragalactic Magnetic Fields from Fermi Observations of TeV Blazars", *Science*, 328(5974), 2010.

[277] Justin D. Finke, et al., "Constraints on the Intergalactic Magnetic Field with Gamma-Ray Observations of Blazars", *The Astrophysical Journal*, 814, 2015, p. 20, URL `https://ui.adsabs.harvard.edu/#abs/2015ApJ...814...20F`.

[278] M. Fernandez Alonso and VERITAS Collaboration, "Limits to the Intergalactic Magnetic Field from extended gamma-ray emission around blazars", *Boletin de la Asociacion Argentina de Astronomia La Plata Argentina*, 59, 2017, pp. 90–92, URL `http://adsabs.harvard.edu/abs/2017BAAA...59...90F`.

[279] J. E. Gunn and B. A. Peterson, "On the Density of Neutral Hydrogen in Intergalactic Space.", *The Astrophysical Journal*, 142, 1965, pp. 1633–1641, URL `http://adsabs.harvard.edu/abs/1965ApJ...142.1633G`.

[280] P. J. E. (Phillip James Edwin) Peebles, *Principles of physical cosmology*, Princeton, N.J. : Princeton University Press, 1993, includes bibliographical references (p. [685]-709) and index.

[281] D. N. Spergel, et al., "First-Year Wilkinson Microwave Anisotropy Probe (WMAP) Observations: Determination of Cosmological Parameters", *The Astrophysical Journal Supplement Series*, 148, 2003, pp. 175–194, URL `https://ui.adsabs.harvard.edu/#abs/2003ApJS..148..175S`.

[282] Ralph E. Pudritz, et al., "Magnetic Fields in Astrophysical Jets: From Launch to Termination", *Space Science Reviews*, 169, 2012, pp. 27–72, URL `https://ui.adsabs.harvard.edu/#abs/2012SSRv..169...27P`.

[283] F. Tavecchio, et al., "TeV BL Lac objects at the dawn of the Fermi era", *Monthly Notices of the Royal Astronomical Society*, 401, 2010, pp. 1570–1586, URL `https://ui.adsabs.harvard.edu/#abs/2010MNRAS.401.1570T`.

[284] Fabrizio Tavecchio, et al., "Photons to axion-like particles conversion in Active Galactic Nuclei", *Physics Letters B*, 744, 2015, pp. 375–379, URL `https://ui.adsabs.harvard.edu/#abs/2015PhLB..744..375T`.

[285] G. Ghisellini, et al., "General physical properties of bright Fermi blazars", *Monthly Notices of the Royal Astronomical Society*, 402, 2010, pp. 497–518, URL `https://ui.adsabs.harvard.edu/#abs/2010MNRAS.402..497G`.

[286] N. A. Miller, et al., "Redshifts for a Sample of Radio-selected Poor Clusters", *Astronomical Journal*, 123, 2002, pp. 3018–3040, URL `http://adsabs.harvard.edu/abs/2002AJ....123.3018M`.

[287] M. W. Auger, et al., "The Environments of Low- and High-Luminosity Radio Galaxies at Moderate Redshifts", *Astronomical Journal*, 135, 2008, pp. 1311–1317, URL `http://adsabs.harvard.edu/abs/2008AJ....135.1311A`.

[288] K. Dolag, et al., "Non-Thermal Processes in Cosmological Simulations", *Space Science Reviews*, 134, 2008, pp. 311–335, URL `https://ui.adsabs.harvard.edu/#abs/2008SSRv..134..311D`.

[289] Y. Dubois and R. Teyssier, "Cosmological MHD simulation of a cooling flow cluster", *Astronomy and Astrophysicsl*, 482, 2008, pp. L13–L16, URL `https://ui.adsabs.harvard.edu/#abs/2008A&A...482L..13D`.

[290] Luigina Feretti, et al., "Clusters of galaxies: observational properties of the diffuse radio emission", *Astronomy and Astrophysics Review*, 20, 2012, p. 54, URL `https://ui.adsabs.harvard.edu/#abs/2012A&ARv..20...54F`.

[291] Manuel Meyer, et al., "On detecting oscillations of gamma rays into axion-like particles in turbulent and coherent magnetic fields", *Journal of Cosmology and Astro-Particle Physics*, 2014, 2014, p. 003, URL `https://ui.adsabs.harvard.edu/#abs/2014JCAP...09..003M`.

[292] R. A. Laing, et al., "Structures of the magnetoionic media around the Fanaroff-Riley Class I radio galaxies 3C31 and Hydra A", *Monthly Notices of the Royal Astronomical Society*, 391, 2008, pp. 521–549, URL `http://adsabs.harvard.edu/abs/2008MNRAS.391..521L`.

[293] R. A. Laing, et al., "Structures of the magnetoionic media around the Fanaroff-Riley Class I radio galaxies 3C31 and Hydra A", *Monthly Notices of the Royal Astronomical Society*, 391, 2008, pp. 521–549, URL `http://adsabs.harvard.edu/abs/2008MNRAS.391..521L`.

[294] M. Murgia, et al., "Magnetic fields and Faraday rotation in clusters of galaxies", *Astronomy and Astrophysicsl*, 424, 2004, pp. 429–446, URL `http://adsabs.harvard.edu/abs/2004A%26A...424..429M`.

[295] M. Ajello et al., "Search for Spectral Irregularities due to Photon-Axionlike-Particle Oscillations with the Fermi Large Area Telescope", *Physical Review Letters*, 116(16), 2016, p. 161101, URL `https://arxiv.org/abs/1603.06978`.

[296] G. Cowan, *Statistical data analysis*, Oxford University Press, USA, 1998.

[297] J.L. Han, "Observing Interstellar and Intergalactic Magnetic Fields", *Annual Review of Astronomy and Astrophysics*, 55(1), 2017, pp. 111–157, URL `https://doi.org/10.1146/annurev-astro-091916-055221`.

Declaration of independent work

I declare that I have completed the thesis independently using only the aids and tools specified. I have not applied for a doctor's degree in the doctoral subject elsewhere and do not hold a corresponding doctor's degree. I have taken due note of the Faculty of Mathematics and Natural Sciences PhD Regulations, published in the Official Gazette of Humboldt-Universität zu Berlin no. 126/2014 on 18/11/2014.

Berlin, 22 February 2019 Galo Gallardo Romero